

國立交通大學

物理研究所

博士論文

利用掃瞄穿隧顯微鏡觀測雙原子分子在表面上的反應

Scanning Tunneling Microscopy Studies of Surface

Reactions of Diatomic Molecules



研究生：馮世鑫

指導教授：江進福 教授

林登松 教授

中華民國九十七年十月

利用掃描穿隧顯微鏡觀測雙原子分子在表面上的反應

**Scanning Tunneling Microscopy Studies of Surface
Reactions of Diatomic Molecules**

研究生：馮世鑫

Student : Shyh-Shin Ferng

指導教授：江進福

Advisor : Tsin-Fu Jiang

林登松

Deng-Sung Lin

國立交通大學

物理研究所



Submitted to Institute of Physics
College of Science
National Chiao Tung University
in partial Fulfillment of the Requirements
for the Degree of
Doctor
in
Physics

October 2008

Hsinchu, Taiwan, Republic of China

中華民國九十七年十月

利用掃描穿隧顯微鏡觀測雙原子分子在表面上的反應

學生：馮世鑫

指導教授：江進福

林登松

國立交通大學物理研究所博士班

摘要

本論文主要是利用掃描穿隧顯微鏡 (STM) 觀察分子在表面上的作用與反應，其中的課題包括分子結合脫附、表面結構相變化、分子吸附、熱原子動力學以及基底大小對量子點成長的影響。本論文各章節大概編排如下：第一章簡介分子在表面上的吸附以及脫附動力學。第二章描述實驗上的儀器架構、STM 操作原理、樣品製備方式以及探針脫附的技巧。而第三章到第五章是展現實驗結果以及討論。第六章為實驗結果的結論以及進一步的討論。

在探討表面結構相變化的部分，氫原子在 Si(100) 表面上可使表層矽原子鍵結一個氫原子 (monohydride) 或者鍵結兩個氫原子 (dihydride)，而這兩種結構的組合可讓 Si(100) 表面上形成三種穩定的相位： (1×1) 、 (3×1) 以及 (2×1) 相位，氫原子的覆蓋率分別為 2、1.33 以及 1 個表層矽原子密度。本實驗探討 (1×1) 和 (3×1) 相位是如何相變到 (2×1) 相位，以及氫原子由表面熱脫附的動力學機制，做法是加熱擁有 (1×1) 和 (3×1) 相位的樣品，使表面上的結構相變至 (2×1) 相位，再利用掃描穿隧顯微鏡觀察表面上的變化。結果顯示氫分子由 dihydride 區域脫附時 (由 1×1 區域脫附)，兩個氫原子來自於相鄰兩個 dihydride 內側的氫原子。這種脫附方式在 (3×1) 區域進行前，必須先有 dihydride 與 monohydride 位置交換的動作，才能產生相鄰的 dihydride。而氫分子由 monohydride 區域脫

附是在樣品溫度較高時，兩個氫原子來自於同一個 dimer 上的氫原子。

在研究分子吸附動力學部分，首先討論碘分子在乾淨 Si(100) 表面上的吸附動力學。碘分子覆蓋率較低時，結果顯示兩個碘原子吸附在相鄰同排 dimer row 同側上的活性鍵的機率最高。當碘的吸附量增加後，最高的覆蓋率只能達到 0.92 個表層矽原子密度。為了進一步探討碘分子以及氯分子的吸附動力學，我們在覆蓋了氫原子的 Si(100) 表面上製備出擁有孤立活性鍵的表面，這些活性鍵可以是單一的、成對的、成串的或是長鍊狀的。當碘分子和氯分子與這些活性鍵作用後，我們觀察到兩種分子是以不同的動力學做吸附。對於碘分子的吸附，兩個碘原子的吸附必須同時產生，分子鍵才會斷裂。所以表面上必須存在兩個且鄰近的活性鍵，碘分子才會裂解吸附。對於氯分子而言，兩個氯原子的吸附是可以單獨進行，所以表面上只需要存在單一個活性鍵，即可使吸附反應發生。反應過程往往是一個氯原子先與活性鍵鍵結，而另一個氯原子可以離開表面，也可以與周遭的原子產生新的反應。

本論文利用真實空間以及原子解析度的影像來探討表面化學反應，其中的利用孤立活性鍵來探討分子吸附動力學更是第一次提出，這樣的表面結構提供一個很好的介面來研究氣體與固體反應動力學。

Scanning Tunneling Microscopy Studies of Surface Reactions of Diatomic Molecules

Student : Shyh-Shin Ferng

Advisor : Tsin-Fu Jiang

Deng-Sung Lin

**Institute of Physics
National Chiao Tung University**

Abstract

The objective of this thesis focuses on the fundamental issues in surface reactions by using scanning tunneling microscopy (STM). The scientific issues include recombinative desorption, structure phase transition, dissociative adsorption, abstractive adsorption, hot atom motion, and size-dependent quantum-dot growth. The thesis is organized as following: Chapter 1 introduces the common mechanisms of molecules adsorption and desorption on the surface. Chapter 2 describes the experimental setup employed during this research. The STM operating principles, sample preparation procedures, and STM lithography techniques are also explained. The detailed results and discussions of each issue are presented in Chapter 3, 4, and 5. Finally, Chapter 6 summarizes the results and further discussions.

For the discussion of structure phase transition on the Si(100) surface, monohydrides dimers (SiH) and dihydride (SiH₂) species can form an ordered mixture with (3 × 1), (1 × 1), and (2 × 1) phases. Thermal annealing at 570 K causes both the (3 × 1) and (1 × 1) domains to transform to the (2 × 1) phases. During the hydrogen reduction from 1.33 ML to 1 ML, the recombinative desorption of H₂ from dihydride

and monohydride species are investigated. Desorption from dihydrides proceeds by recombination of two H atoms coming separately from two adjacent dihydrides. This process is geometrically forbidden for the (3×1) surface, but becomes possible with a switch of a dihydride with a neighboring monohydride dimer. Desorption from monohydrides occurs at a higher temperature, and proceeds by recombination of the two H atoms on a given monohydride dimer.

In the discussions of molecule adsorption mechanisms, I_2 on a prototypical semiconductor surface is observed. Adsorption of I_2 on the same side of neighboring dimer is favored than on one dimer with the ratio 1 at low coverage. After further I_2 exposure, the maximum iodine coverage is 0.92 ML. To distinguish the adsorption geometry for I_2 , single dangling bond pairs that are fabricated on H/Si(100) surface are used for I_2 adsorption. Different adsorption mechanisms of I_2 and Cl_2 are demonstrated with I_2 and Cl_2 reaction to dangling bonds in isolation or organized in pairs, clusters, or arrays. Iodine chemisorption is predominantly a pair process involving the bonding of the two I atoms in a I_2 molecule onto two neighboring dangling bonds. In sharp contrast, adsorption of Cl_2 is dominated by the bonding of just one Cl atom in a Cl_2 molecule, with the other Cl atom either leaving the surface or migrating to a nearby area to cause further reactions.

This thesis gives the real-space images and detailed atomic processes by *in situ* studies. The adsorption mechanisms of molecules on various initial active site configurations are first reported. This approach points to opportunities for systematic investigations of the atomistics of gas-surface reactions.

Acknowledgements

感謝指導老師林登松教授在我碩、博期間的指導與教誨，六年的相處讓我獲益良多。感謝實驗室夥伴鎧銘學長、明峰、昌廷、仁陽在這些年來的幫助與指教，以及謝謝宏道、靖勛、中廷以及展源的陪伴，讓我博士生涯的最後一年充滿歡樂，也要感謝曉穎、欣樺、靈櫻以及歷屆畢業學弟妹的照顧。

感謝我的父親馮國添先生、母親吳美彩女士以及家人在這些年來的支持，讓我無後顧之憂地專注於實驗研究上，最終完成博士學位。謝謝女友君黛一路上的陪伴與等待，以及君黛父母張航雲先生與溫幼霞女士的關心及照顧。也感謝所有踢球的朋友，讓我可以不時地活動筋骨以及抒解每星期的疲勞。

I would also like to thank Karina, Jörg, Michael, Heiko, Fatih, Xin, Christopher and Carsten for your help and guidance during I stayed in Germany.



Contents

摘要.....	i
Abstract.....	iii
Acknowledgements	v
List of Figures.....	viii
Chapter 1 Introduction.....	1
1.1 Motivation.....	1
1.2 Si(100) surface	8
1.3 Literature Review.....	10
Chapter 2 Experimental Apparatus	16
2.1 Vacuum System.....	16
2.2 Scanning Tunneling Microscopy (STM)	18
2.3 Preparing STM tips	21
2.4 Sample preparation	23
2.5 Nanostructuring.....	27
Chapter 3 Atomistic View of the Recombinative Desorption of H₂ from H/Si(100)	30
3.1 Introduction.....	30
3.2 Experiment.....	33
3.3 Results and Discussion	34
3.3.1 Recombinative desorption of H ₂ from H/Si(100)	34
3.3.2 Evolution of two-dimension structure phase transition (1 × 1) → (2 × 1) and (3 × 1) → (2 × 1).....	40
3.4 Conclusion	46
Chapter 4 Unsaturated Characteristic of the I/Si(100) Surface via Dissociative Adsorption Mechanism	47
4.1 Introduction.....	47
4.2 Experiment.....	49
4.3 Results and Discussion	50
4.3.1 I ₂ dissociative adsorption on Si(100) surface.....	50
4.3.2 Presence of isolated single danglings	57
4.3.3 Maximum distance of two reactive sites allowed for I ₂ dissociative adsorption.....	60
4.4 Conclusion	64
Chapter 5 Topographically Constrained Adsorption and Reaction Mechanisms of I₂ and Cl₂ on the Si(100) Surface.....	65

5.1	Introduction.....	65
5.2	Experiment.....	66
5.3	Results and Discussion	67
5.4	Conclusion	77
Chapter 6	Conclusion	78
Appendix A	Growth Behaviour of Ge Nano-islands on The Nanosized Si{111} Facets Bordering on Two {100} Planes	81
A.1	Introduction.....	81
A.2	Experiment.....	83
A.3	Results and Discussion.....	85
A.3	Results and Discussion.....	85
A.3.1	The formation of well-confined {111} surface.....	85
A.3.2	Ge nano-islands on the (100) planes.....	87
A.3.2	Ge nano-islands on the {111} planes.....	89
A.3.4	Conclusion	96
References.....		97



List of Figures

Fig. 1.1 Schematic diagram showing normal surface reaction.	2
Fig. 1.2 Potential energy curve for the diatomic molecule adsorption on the surface...3	3
Fig. 1.3 Potential energy curves of non-activated and activated adsorption.....4	4
Fig. 1.4 Three normal adsorption mechanisms.	5
Fig. 1.5 If the surface can be saturated via dissociative adsorption mechanism.	6
Fig. 1.6 H atoms recombinative desorption from the surface and monohydride species rearrangement during phase transition.....	7
Fig. 1.7 Schematic illustration showing the reconstructed Si(100) surface.....	9
Fig. 1.8 Proposed mechanism for the conversion of H/Si(001)-3×1 to H/Si(001)-2×1	10
Fig. 1.9 Possible initial configurations following loss of two H atoms.....	11
Fig. 1.10 TPD spectra of H ₂ desorption obtained from H-saturated Si(100).....	12
Fig. 1.11 Dissociative adsorption of a Cl ₂ molecule on the buckled dimer.	13
Fig. 1.12 The structures observed in STM experiments after dissociative adsorption of Cl ₂ on Si(100).	14
Fig. 1.13 Initial stages of Cl ₂ adsorption showing the different Cl adsorption sites....	15
Fig. 1.14 TOF showing abstractive adsorption).....	15
Fig. 2.1 Schematic illustration the top view of the UHV chamber.	17
Fig. 2.2 Schematic illustration of the STM system.....	20
Fig. 2.3 The sketch of the etching procedure for the tungsten (W) tip.....	22
Fig. 2.4 STM image of H/Si(100)-(2 × 1) surface with several dangling bonds.	25
Fig. 2.5 STM image of H/Si(100)-(3 × 1) surface.	26
Fig. 2.6 Schematic illustration showing nanostructuring on H/Si(100) surface.	27

Fig. 2.8 Array of DBs was fabricated on a H terminated Si(100).....	29
Fig. 3.1 Schematic diagrams showing (1 × 1) dihydride, (2 × 1) monohydride, and (3 × 1) mixed monohydride-dihydride phases, and χ , δ , and μ reactions.....	32
Fig. 3.2 STM images after a (3 × 1) sample has been annealed at 570 K for different times.....	35
Fig. 3.3 Closeup images showing desorption processes from dihydride domain and monohydride domain	37
Fig. 3.4 Time evolution of H/Si(100) surface after sample was heated at 570K for different time.....	41
Fig. 3.5 Coverage for vacancies, (1 × 1), (3 × 1)), and (2 × 1) domains as functions of annealing time at 570 K	44
Fig. 3.6 STM image near step edge after nominal H/Si(100)-(3 × 1) is annealed.....	45
Fig. 4.1 STM images showing I ₂ adsorption on the Si(100) surface at different coverage.....	52
Fig. 4.2 Zoom-in images showing some configurations at low and high coverage surface.....	55
Fig. 4.3 Coverage of iodine and isolated SDB as function of I ₂ exposure	56
Fig. 4.4 Showing the population of each new adsorption site.....	59
Fig. 4.5 Showing before and after 1.32 L I ₂ expose on single DBs	62
Fig. 4.6 Showing before and after 1.32 L I ₂ expose on series of SDB pairs.....	63
Fig. 5.1 Showing before and after I ₂ expose on single and paired DBs.	68
Fig. 5.2 Showing before and after I ₂ expose on cluster of dangling bonds.....	69
Fig. 5.3 Showing different configurations after Cl ₂ expose on single DBs.....	71
Fig. 5.4 Showing before and after Cl ₂ expose on cluster of dangling bonds.....	74
Fig. 5.5 Showing before and after Cl ₂ expose on a linear array of dimer dangling bond pairs.....	75

Fig. 5.6 Showing before and after Cl₂ expose on a stripe of dangling bonds 76

Fig. A.1 Process flow chart for the fabrication of 2D arrays of rectangular mesas and negative pyramids. 84

Fig. A.2 AFM z-height profiles over the mesa side walls following etching in KOH + IPA solution. 86

Fig. A.3 Derivative AFM images displaying Si mesas after Ge growth. 88

Fig. A.4 Zoom-in three-dimensional images over the {111} facet. 91

Fig. A.5 Zoom-in derivative images over the {111} facet. 92

Fig. A.6 Three-dimensional AFM images showing a negative pyramid following Ge growth. 95



Chapter 1 Introduction

Why and how do molecules break the molecular bond and adsorb on the surface? This is a simple question and indeed very important for chemical industry and device processing. To answer this question, extensive theoretical and experimental studies have been carried over the half-century. However, most experimental works focused on the examinations of diffraction spectra or the detection of the atoms/molecules scattered from the surface after reactions; these indirect measurements can't reflect the real dynamics of the adsorbates. For the theoretical studies, surface reactions are often too complex to be simulated since the molecule has various transitional states, vibration states, or rotation states, and surface phonons also must be taken in consideration. After STM was invented, it has widely been used to understand the fundamental surface reaction by providing real-space images. However much detailed reaction dynamics are still not clear.

In this thesis, I will elucidate the surface reaction of H_2 , Cl_2 , and I_2 on Si(100) surface by patterning various dangling bond geometry. These studies include recombinative desorption, surface phase transition, dissociative adsorption, abstractive adsorption, hot atom motion, and cascading reaction.

1.1 Motivation

A surface reaction is complicated; it involves the interaction between the molecule and the substrate, the molecule and adsorbates, and adsorbates and adsorbates. Figure 1.1 shows a few common surface reactions. An incident molecule first adsorbs on the surface if the total energy decreases after formation of surface chemical bonds. The molecule bond can break and two atoms dissociate. The atoms can diffuse to the nearby existed adsorbates to form cluster or re-bond with other

adsorbate and desorbs away from the surface. Sometimes, the adsorbed atom could extract the substrate atom and create a vacancy site.

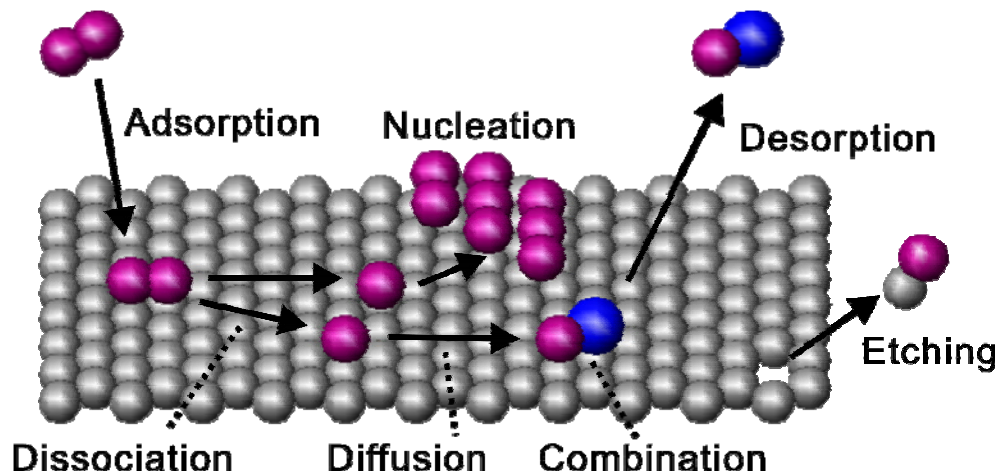


Fig. 1.1 Schematic diagram showing normal surface reaction.

Before the various surface reactions proceed, a molecule has to land on the surface. Figure 1.2 shows the Potential Energy Curve (PEC) for diatomic molecule adsorption on the surface. There are three different PECs, molecular physisorption PEC, molecular chemisorption PEC, and atomic chemisorption PEC. Typically an incoming molecule is trapped in a physisorption well when molecule comes from the gas source to the vicinity of a surface. If there is a charge transfer to the molecule, the molecule can then enter the molecular chemisorption well. The molecular bond will break as the total energy is further decreased after new chemical bonds are formed with the surface. Whether a molecule is adsorbed or not also depends on the activation barrier. Figure 1.3 shows that there are two kinds of adsorption, non-activated and activated adsorption. For non-activated cases, the direct chemisorption occurs. In the later case, an activation barrier prevents the molecule bond to break even though the molecule can

be trapped in a precursor well as precursor-mediated state. The precursor state may migrate on the surface and then either leave the surface or is adsorbed on somewhere else with a smaller barrier.

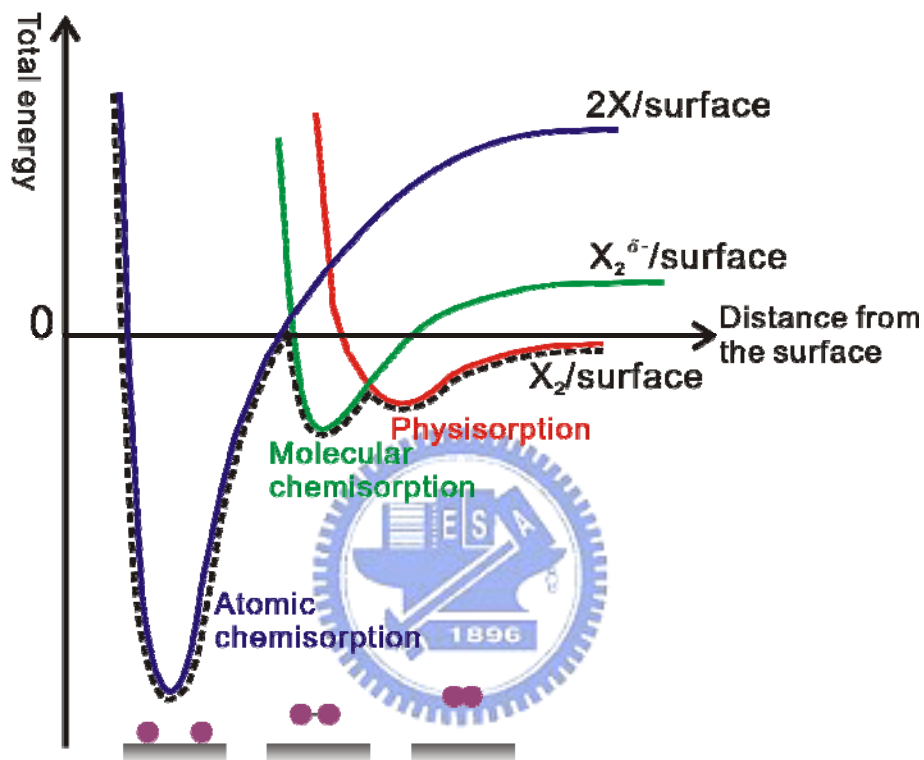


Fig. 1.2 Schematic illustration showing potential energy curve for the diatomic molecule adsorption on the surface.

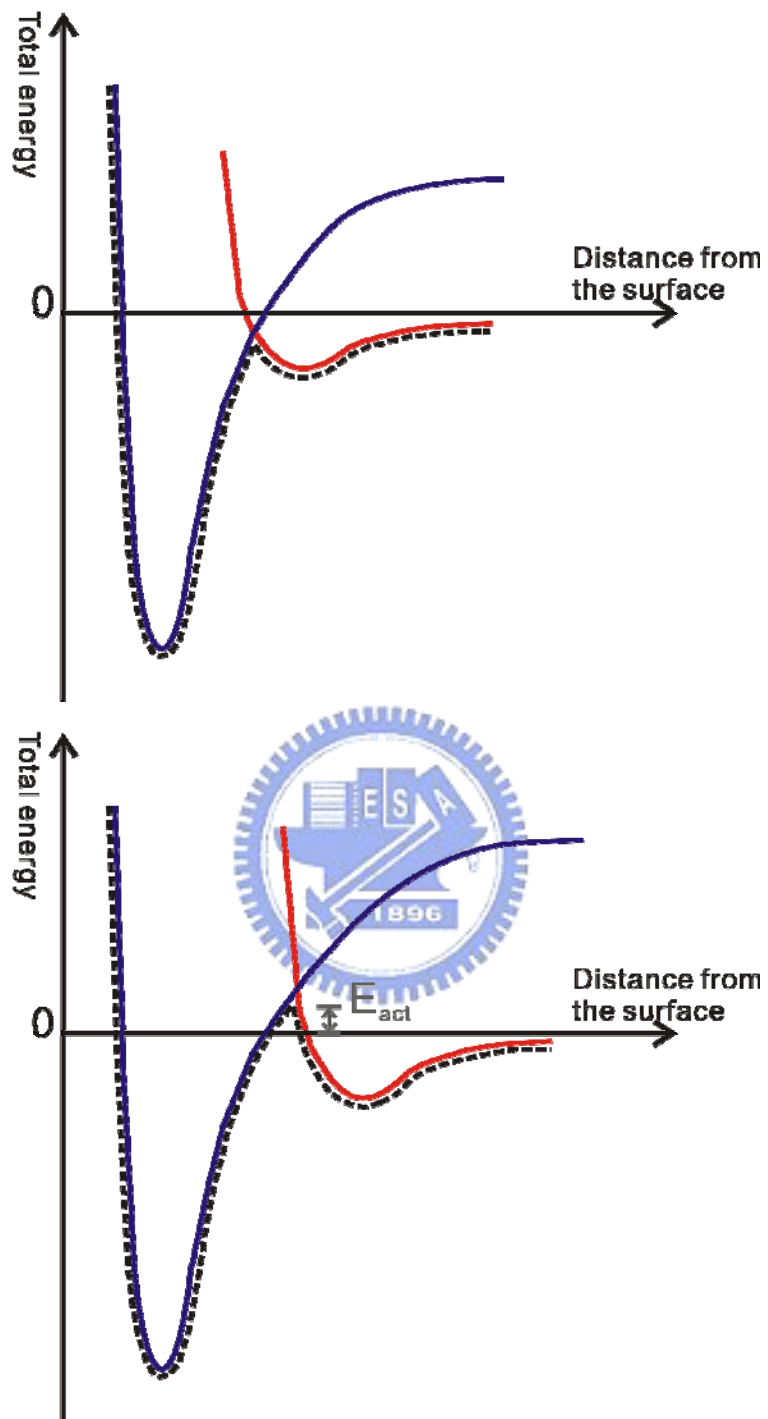


Fig. 1.3 Schematic illustration showing potential energy curves of non-activated and activated adsorption. E_{act} is the activation barrier for adsorption.

The adsorption mechanisms are commonly classified into three categories: dissociative adsorption, abstractive adsorption or hot atom process, as shown in Fig. 1.4. The dissociative adsorption means the molecular bond broken as two atom-substrate bonds are created. The hot atom process means the adsorbed atoms land at a distance in between. In other words, two atoms migrate a short distance before they settle down. In an abstractive adsorption, one atom of the molecule is adsorbed on the surface, while the other atom leaves the surface.

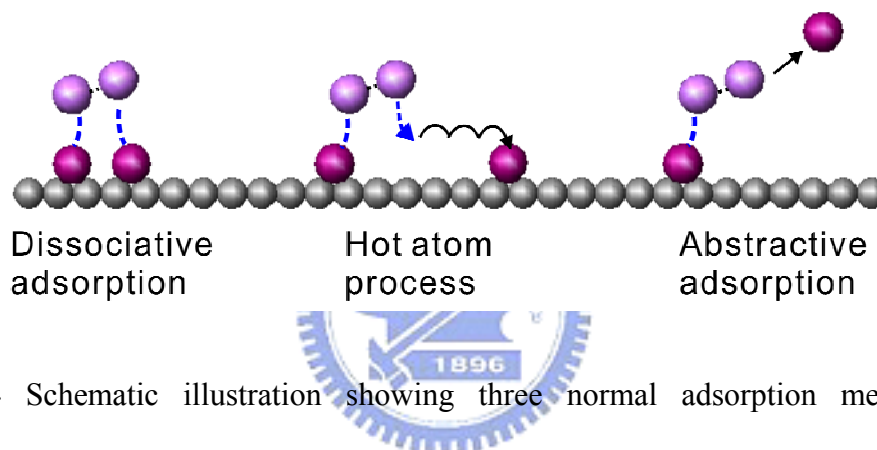


Fig. 1.4 Schematic illustration showing three normal adsorption mechanisms: dissociative adsorption, hot atom process, and abstractive adsorption.

As discussed above, the surface reaction or adsorption mechanisms are complicated, and some adsorbates are mobile. The final state that we obtained could be the result after adsorbate-adsorbate interaction, as shown in Fig. 1.5(a). In order to simplify the reaction and separated study each reaction, we fabricated several isolated reactive sites, i.e. isolated dangle bond, as shown in Fig. 1.5(b).

There are many interesting questions about diatomic molecule adsorption on this special configuration. For examples, if diatomic molecule adsorb on single DB sites? If molecules can be confined in the 1D dangling bond line? Our results will give answers to these issues.

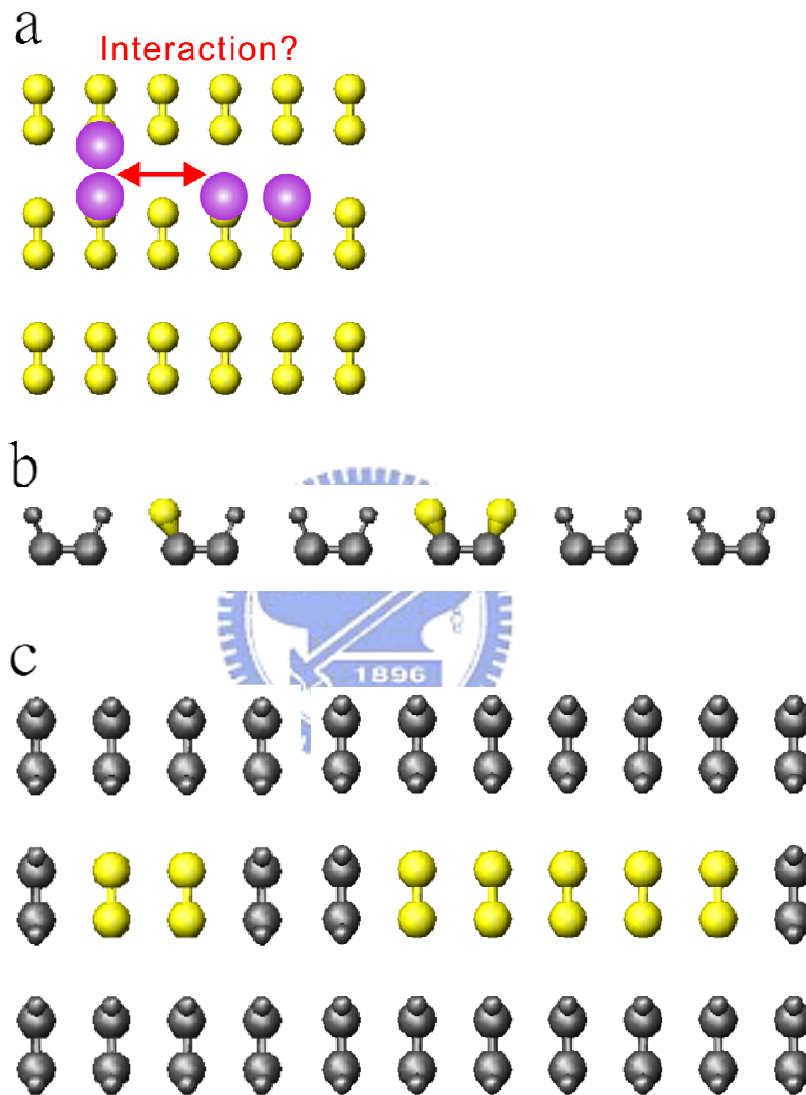


Fig. 1.5 Schematic illustration showing if the surface can be saturated via dissociative adsorption mechanism.

In addition, I also studied the recombinative desorption of diatomic molecule. Here we chose the hydrogen molecule as our main actor. There are three different H/Si(100) phase with different mixture of monohydride and dihydride. What we are interested in is how two H atom organize themselves to recombinatively desorb away from the surface, as illustrated in Fig. 1.6.

In thesis, the research is based on H/Si(100) surface, so I will discuss this surface first and including of hydrogen recombinative desorption. Then I will demonstrate that I₂ adsorption on clean Si(100) surface. Finally, I compare the different adsorption mechanisms of I₂ and Cl₂ using isolated or paired dangling bonds on H-terminated surface. The appendix includes a study of growth behaviour of Ge nano-islands on the nanosized Si{111} facets bordering on two {100} planes. The reason to organize this research in the appendix is that the reaction gas GeH₄ is a more complex gas, not a diatomic molecule.

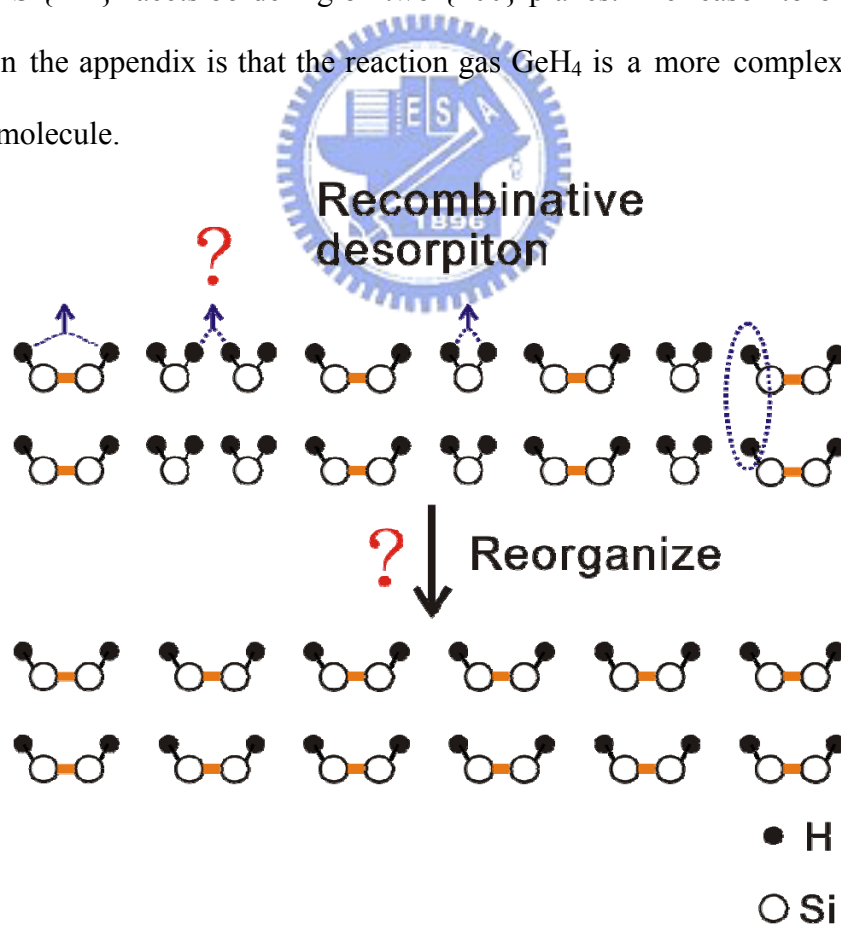


Fig. 1.6 Schematic illustration showing how is the H atoms recombinative desorption from the surface and monohydride species rearrangement during phase transition.

1.2 Si(100) surface

If one cleaves the silicon crystal along the (100) direction, two valence bonds of each exposure surface Si atom will be broken and become so-called dangling bonds on the surface. Therefore, every silicon atom in the unreconstructed surface has two dangling bonds and two valence bonds, as shown in Fig. 1.7. The unreconstructed surface has a 1×1 structure. In this 1×1 structure, the density of the dangling bonds is high (two dangling bonds per atoms), therefore the surface energy is high and the 1×1 structure is unstable. To reduce the numbers of the dangling bonds, the first layer atoms in the surface will reconstruct. By this way, the surface energy will be lower and the 1×1 structure will be more stable.

Upon reconstruction, two adjacent atoms form a strong sigma bond by combined one of the two dangling bonds. The numbers of dangling bonds is reduced by 50%. These remaining dangling bonds can further form a weak π bond. The 1×1 structure of the surface have transformed into 2×1 structure. These bonded pairs of Si atoms are called dimers. These dangling bonds are chemically reactive. An example is shown in 1.7: every dangling bond trap a hydrogen atom after hydrogen expose.

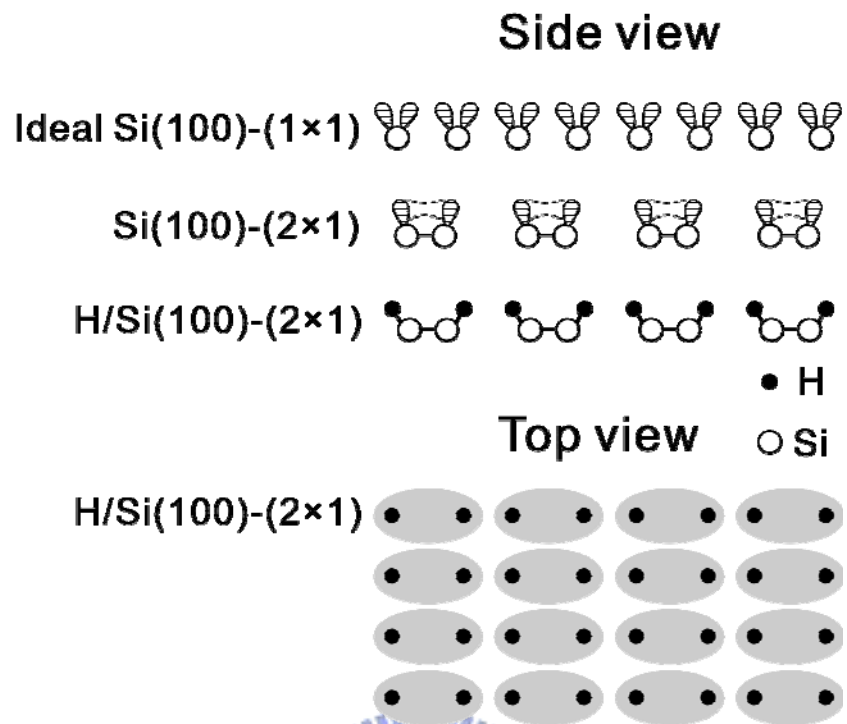


Fig. 1.7 Schematic illustration showing reconstructed Si(100) surface.



1.3 Literature Review

How are two H atoms from a dihydride recombination desorbed from the Si(100) surface? Scientists used several methods to answer this question [1,2,3,4]. Chen et al. proposed that the H₂ desorbs first as dihydride species, then the neighboring σ-bond switches, and finally a monohydride species is formed, as shown in Fig. 1.8. They also calculated the total energy of each configuration during conversion, as Fig. 1.9 depicts. Their results shows that the low energy reaction intermediate is either bare Si atom or bare dimer. Cheng et al. provided a temperature-programmed desorption (TPD) studied which have shown two desorption peaks: a β₂ peak at about 680 K corresponding to the conversion of dihydrides to monohydrides, and a β₁ peak at about 790 K corresponding to the conversion of monohydrides to the clean Si(100)-(2 × 1) surface, as shown in Fig. 1.10.

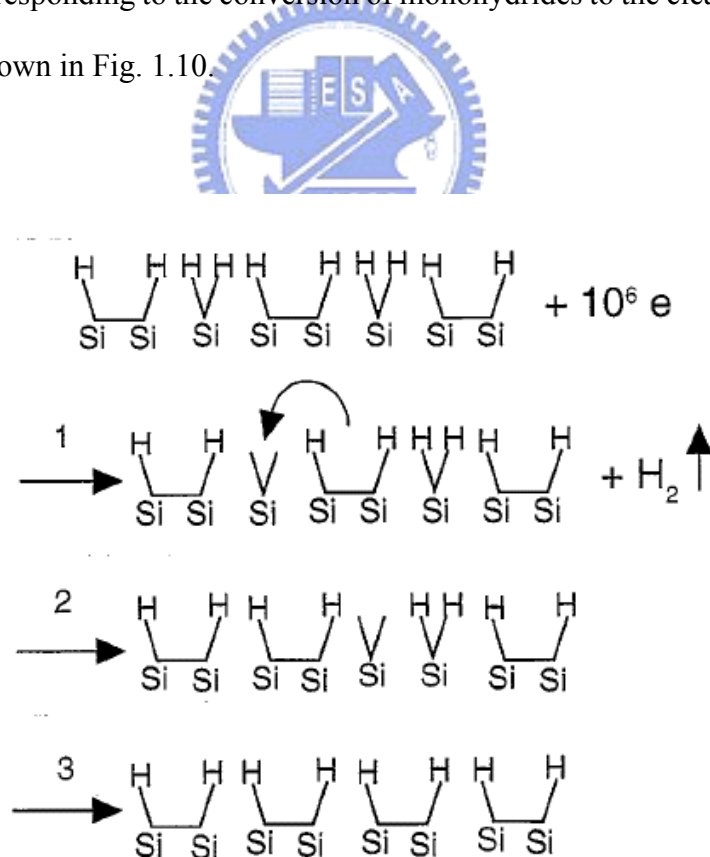


Fig. 1.8 Proposed mechanism for the conversion of H/Si(001)-3 × 1 to H/Si(001)-2 ×

1. Copied by T. C. Shen, Surf. Sci. 390, 35 (1997).

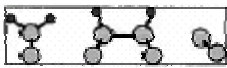
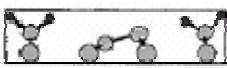
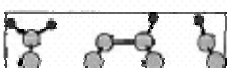
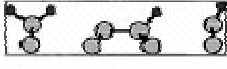

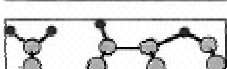


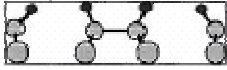
		Rel. Energy (eV)
a		1.73
b		1.72
c		2.59
d		2.44
e		1.96
f		2.45
g		2.72
h		2.74
i		2.75

Fig. 1.9 Possible initial configurations following loss of two H atoms from a DMD unit. The energies (relative to the 2×1 surface) are from the DFT calculations described in the text. Copied from T. C. Shen, Surf. Sci. 446, 211 (2000).

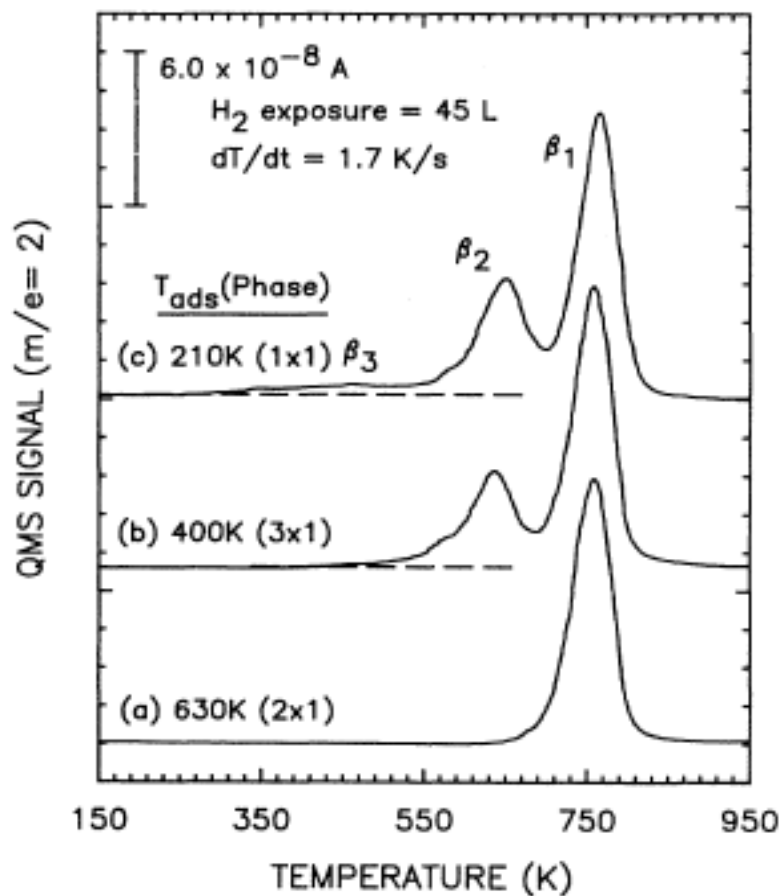


Fig. 1.10 TPD spectra of H₂ desorption obtained from H-saturated Si(100) at different adsorption temperature: (a) 630 K, (b) 400 K, 210 K. Spectra were taken with a heating rate of 1.7 K/s after the crystal was cooled down to 130K. Copied from C. C. Cheng, Phys. Rev. B 43, 4041 (1991).

The interaction of halogen molecules with Si surface is scientifically and technologically important. This system has been studied by various surface analysis techniques over the years [5,6,7]. Mori et al. use first-principle molecular-dynamics to simulate the adsorption with picosecond resolution, as shown in Fig. 1.11. They demonstrated that Cl₂ and F₂ molecules adsorb dissociatively at dangling bonds of a buckled dimer with no energy barrier, so that the buckled dimer becomes geometrically flat. Chan etc. calculated the total energy of different adsorption

configurations, as shown in Fig. 1.12. The energy ordering is Type I < Type IIa < Type IIIa < Type IIIb < Type IIb. Type I is the most stable because it only breaks one weak π bond between the dimer silicon atoms, while the other configurations break two. STM study was performed by Yates etc., as in Fig. 1.13. The adsorption of two Cl atoms on Si dimer sites in adjacent silicon dimer rows was found to be kinetically favored. In 1995, Li et al. identified a new adsorption mechanism: atom abstraction, Fig. 1.14. In this process, one atom of the molecule is adsorbed on the surface, while the other atom leaves the surface.

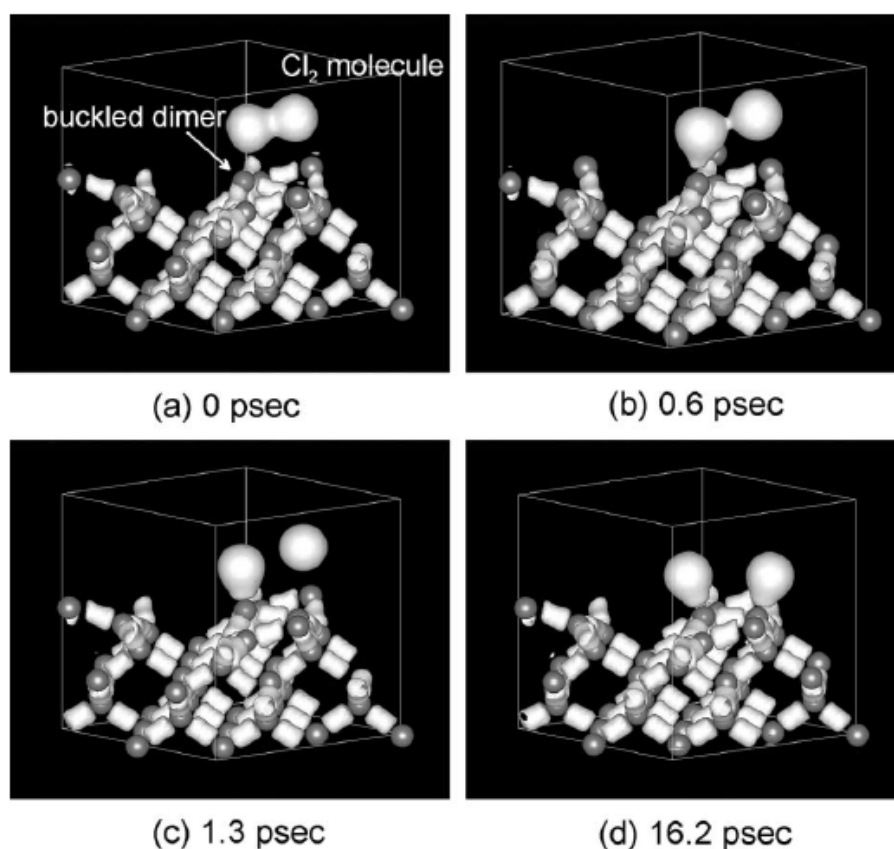


Fig. 1.11 Dissociative adsorption of a Cl_2 molecule on the buckled dimer of the $\text{Si}(001)\text{-p}(2\times 2)$ surface: (a) the initial configuration, (b) and (c) configurations in the middle of the reaction, and (d) the final configuration. Copied from Y. Mori etc., *Surf. Sci.* 515, 287 (2002).

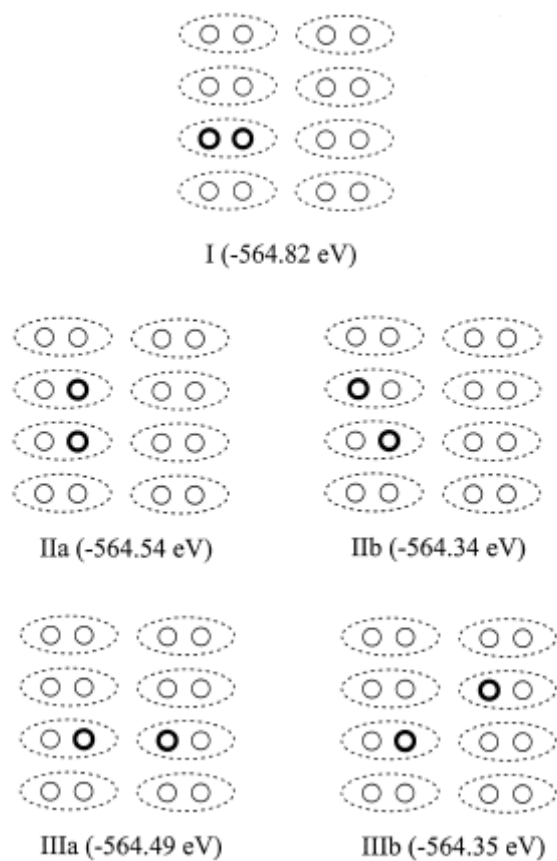


Fig. 1.12 The structures observed in STM experiments after dissociative adsorption of Cl_2 on Si(100). The broken line encircles a Si-Si dimer, while the dark circles indicate the adsorption sites of Cl atoms, which could be on the same dimer as in Type I, or across the same dimer row as in Type IIa and IIb, or across two dimer rows as in Type IIIa and IIIb. Each type of structure is put in a 4×4 surface lattice, which is the lattice used in our calculation. The number in parentheses is the calculated total energy for each structure. Copied from S.P. Chan etc., Chem. Phys. Lett. 318, 15 (2000).

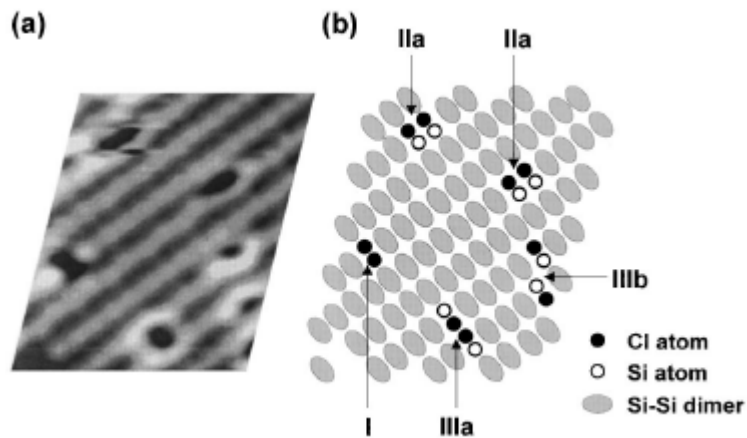


Fig. 1.13 Image of $46 \times 55 \text{ \AA}^2$ region of the Si(100) surface at initial stages of Cl_2 adsorption showing the different Cl adsorption sites. (a) Filled-state STM image at a sample bias of -1.5 V and a tunneling current of 0.05 nA . (b) Schematic identification of the observed features. Copied from J. T. Yates, Jr. etc., Phys. Rev. B 58, 7950 (1998).

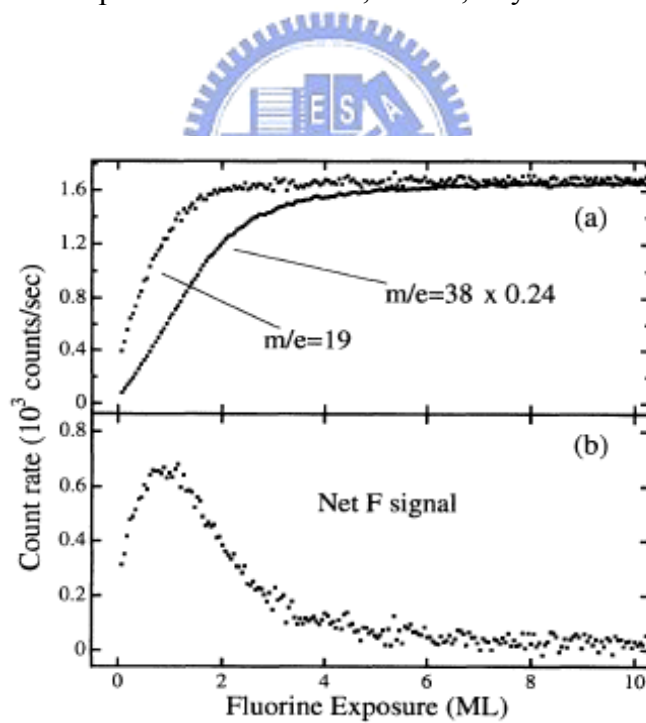


Fig. 1.14 (a) Signal at $m/e = 19$ and 38 (scaled by 0.25) recorded at $\theta_i = 0^\circ$ and $\theta_d = 35^\circ$ versus F_2 exposure in ML. A ML is equivalent to one F atom per Si atom. (b) Net F signal calculated by point-by-point subtraction of plots in (a) Copied from Y. L. Li etc., Phys. Rev. Lett. 74, 2603 (1995).

Chapter 2 Experimental Apparatus

2.1 Vacuum System

The experiments were carried out in the ultra-high vacuum (UHV) system with a base pressure of 1.0×10^{-10} torr. The whole system consists of commercial STM, pumping system, and gas source. The STM system with an indirect heating stage and thermal couple can give option for measurement with the temperature range from room temperature to 650 K. The pumping system includes dry pump, an oil pump, a turbo pump, a titanium sublimation pump (TSP), and an ion pump. The gas sources contain H_2 , I_2 , Cl_2 , and HCl.

The chamber is divided into three parts: Loading chamber, Main chamber, and Gas line as shown in Fig. 2.1. Loading chamber is used to transfer tips and samples. Main chamber is for preparing sample and STM measuring. Gas line is for quick exchanging gas source without venting main chamber. Gas source was introduced into the chamber through a precision leak valve.

In order to obtain ultra-high vacuum, the dry pump and turbo pump were first used to evacuate the chamber from the atmosphere to high vacuum around 10^{-6} torr. A baking procedure was followed to the temperature $\sim 120^\circ C$ for 24 hours. After the pressure started to drop off, most moisture was pumped out, closing the valve between the Loading chamber and Main chamber. Then ion pump with the help of TSP during cool down was supported to achieve ultra-high vacuum.

For the tips and samples transferring, the tips and samples were placed into the Loading chamber, and then we bake Loading chamber to $\sim 130^\circ C$ for 12 hrs to out gas the moisture from the tip holder. After the Loading chamber cool down to room temperature, we transport the tips and samples into Main chamber. Various treatments will be treated depending upon the type of sample used in the experiment.

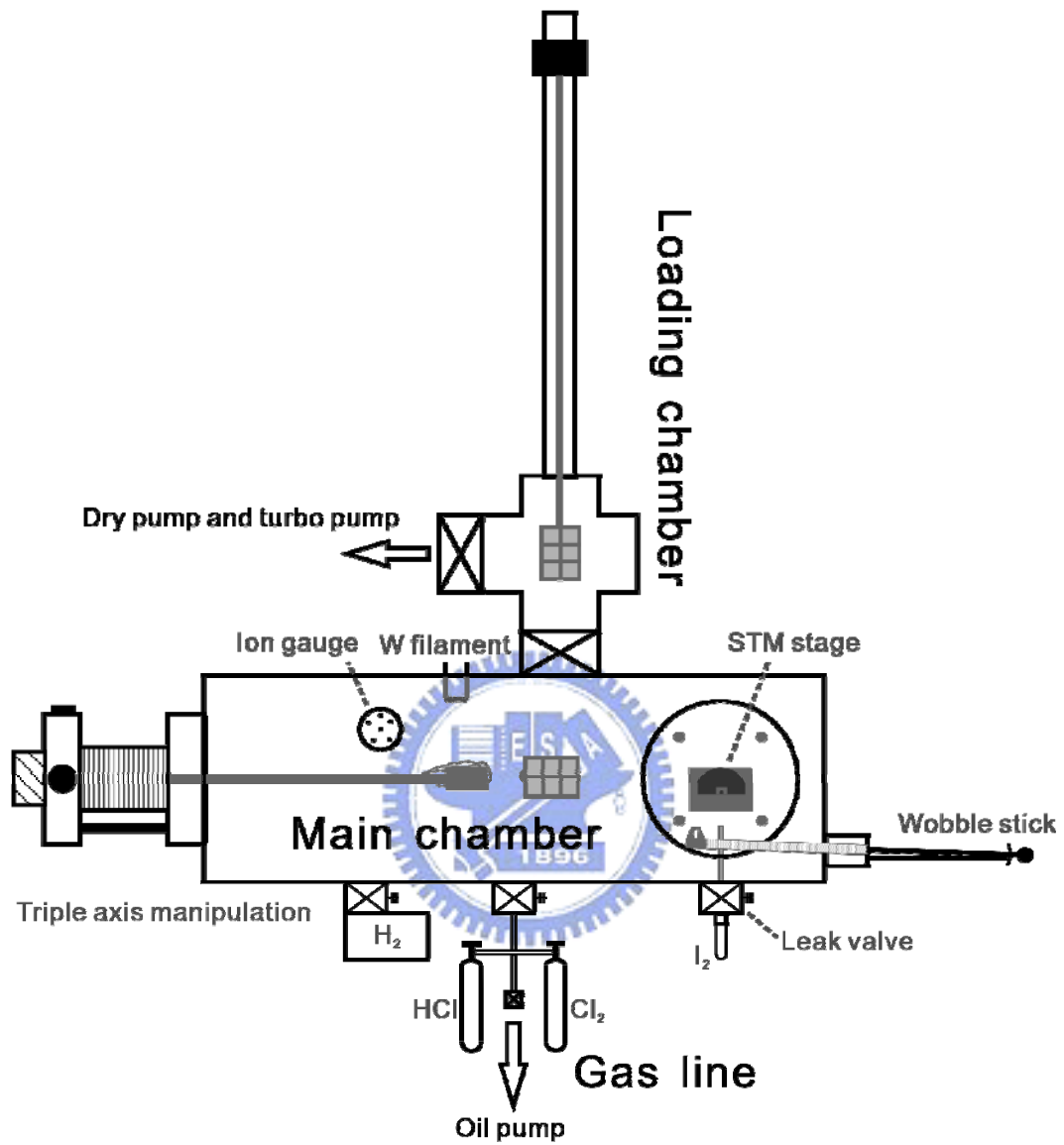


Fig. 2.1 Schematic illustration the top view of the UHV chamber.

2.2 Scanning Tunneling Microscopy (STM)

Scanning Tunneling Microscope (STM) was invented by G. Binnig and H. Rohrer in 1981, they shared the 1986 Nobel Prize in Physics for their invention. With the abilities of real-space surface image and atomic resolution, STM has been widely used in many fields, such as condensed-matter physics, chemical and biology.

Base on quantum mechanical tunneling, a particle can penetrate a potential barrier with nonzero probability. Thus, a sharp conducting tip is brought so close to the probed surface with a gap of a few angstroms, and a bias voltage is applied between tip and sample. This allowing the wave function of tip electron state can overlap with those of the sample. The tunneling current is proportion to density state of the sample and tip, gap voltage, and distance between tip and sample, as followed [8]:

$$I(r_0, V) \propto \int_{E_F}^{E_F+eV} dE \rho_T(E+eV) \rho_s(r_0, E) T(r_0, E, eV)$$

$$T(r_0, E, eV) = e^{-2\kappa s}$$

$$\kappa = [(2m\phi / \hbar^2) + k^2]^{1/2}$$

$$\phi = [\frac{1}{2}(\phi_t + \phi_s) - E + \frac{1}{2}(eV)]$$



$\rho_s(r_0, E)$: density of states of the sample

$\rho_T(E, eV)$: density of states of the tip

$T(r_0, E, eV)$: transmission probability of the electron

eV : applied bias voltage between tip and sample

$s(r_0)$: tip-sample gap width

In the operating of STM, piezoelectric elements are used to control the tip to move in three orthogonal directions as schemed in Fig. 2.2. For the z direction, a feedback

circuit is used to modify tip height in order to maintain a constant current during the operating in constant current mode. The tunneling current with stable feedback current is sensitive to control the distance between tip and sample, and the tunneling current is followed exponential decay. Typically, a change of the gap by 1 Å results in the tunneling current by an order of magnitude. Which gives STM its remarkably high precision in positioning the tip (sub-angstrom vertically and atomic resolution laterally).

As the formula showing above, STM tunneling current is an integration of electronic density of states, i.e., the number of filled or unfilled electron states near the Fermi level, within an energy range determined by the bias voltage. Therefore, STM is a mapping of surface local density of electronic state and can identify and distinguish the atoms or molecules on the surface.



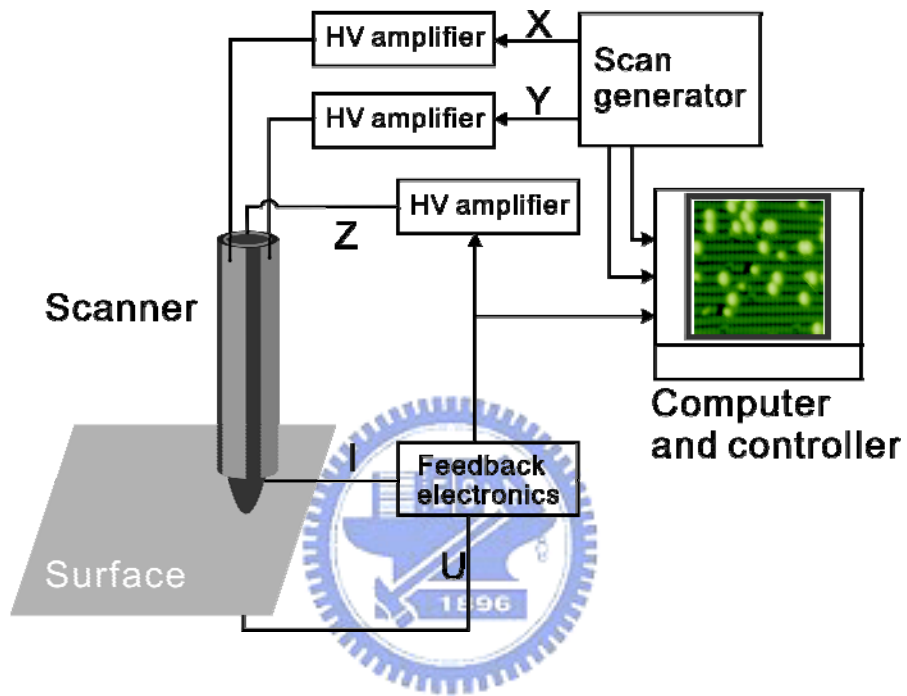
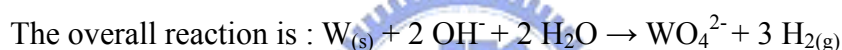
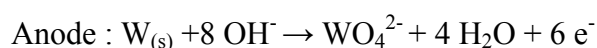
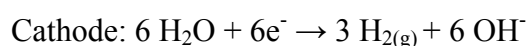


Fig. 2.2 Schematic illustration of the STM system.

2.3 Preparing STM tips

Tungsten wire was chosen to fabricate a sharp tunneling tip for its high conductivity and hardness. A standard method for fabricating a STM tip is electro-chemical etching. For our experiment, W wire with a diameter of 0.5 mm and ~10% NaOH solution were used. Before etching a tip, the W wire was first etched in NaOH solution to clean surface oxide for a few seconds, One end of the W wire was inserted 1.5~2 mm below the solution level. A positive voltage, 7 V, is applied to the W wire as the anode and the cylindrical stainless steel is as the cathode as shown in Fig. 2.3. At the anode and cathode the following reactions take place:



The tungsten which is etched near the interface gets thinner and thinner, and then it is formed a neck shape. Therefore, the end of the wires falls off immediately below the solution surface. Eventually, we can obtain a sharp tip. The tip was soaked into DI water for 20 min and then washed with DI water and methanol.

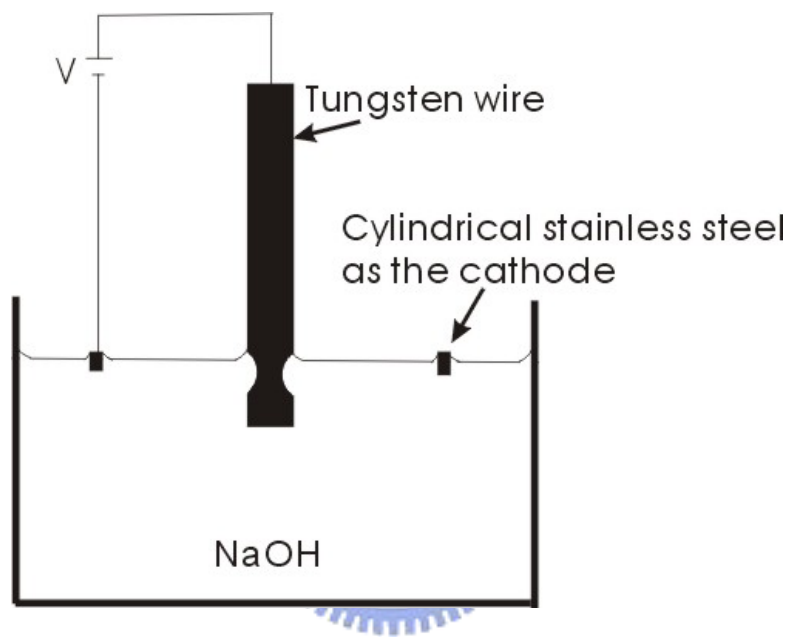
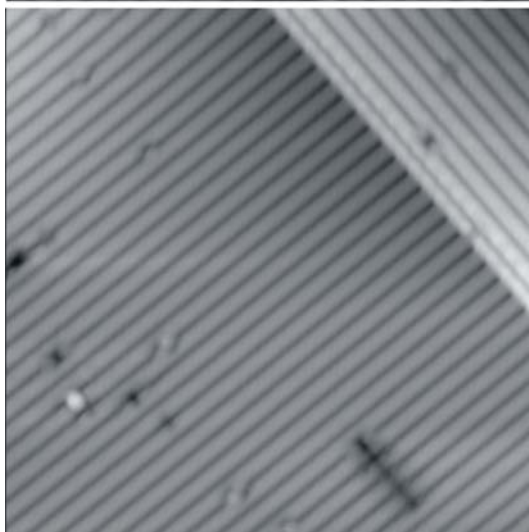
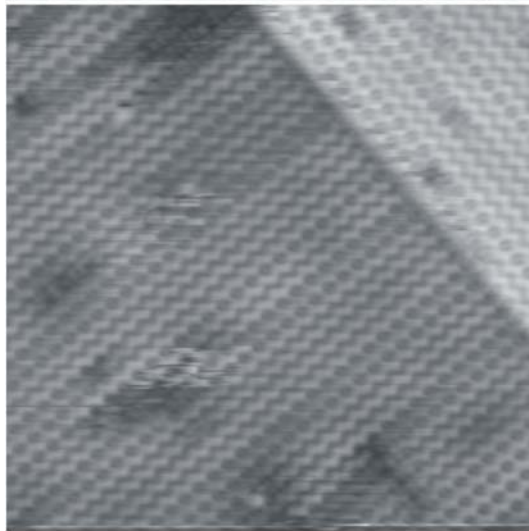
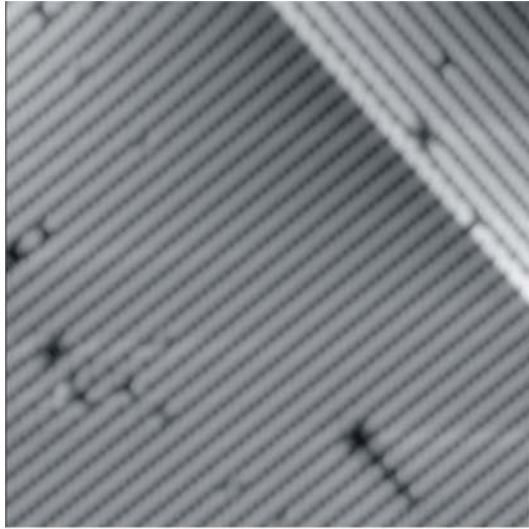


Fig. 2.3 The sketch of the etching procedure for the tungsten (W) tip. The atomic scale tip can be made by the electro-chemical etching.

2.4 Sample preparation

The Si(100) samples was a Boron-doped wafer and had an resistivity of about 10 ohm-cm and doping concentration of $5 \times 10^{15} \text{ cm}^{-3}$. The miscut angle of the samples is 0.1° . The samples were mounted on holders which were made of Ta and Mo. Pure N_2 gas gun was used to remove dusts on the samples' surfaces. After loading into the vacuum chamber, the sample holder was degassed by indirect heating for 12 hours. Then, sample was direct heating up to $\sim 600^\circ\text{C}$ using a small AC current (0.3 A) for 24 hours. In this procedure, the pressure never exceeded over 1.0×10^{-9} torr during sample degassing. To obtain typical Si(100)-(2 \times 1) reconstructed surface, the samples was direct Joule heating at ~ 1400 K with subsequent radiation quenching, as Fig. 2.4.

For preparing H/Si(100) surface, atomic hydrogen was produced by backfilling the chamber to a background pressure of 2×10^{-7} Torr in the presence of a 1800 K tungsten filament, installed ~ 5 cm away from the sample. The flux of atomic hydrogen was not measured, and the exposure was recorded in terms of the background dosage of H_2 inside the chamber. A H/Si(100)-(2 \times 1) surface was generated by dosing 90 L hydrogen on a clean Si(100)-(2 \times 1) surface at 600 K, as shown in Fig. 2.4. While a mixed dihydride and monohydride structure is generated by further dosing 120 L hydrogen at ~ 400 K on H/Si(100)-(2 \times 1) surface, as shown in Fig. 2.5. The sample temperature was measured via an infrared pyrometer.



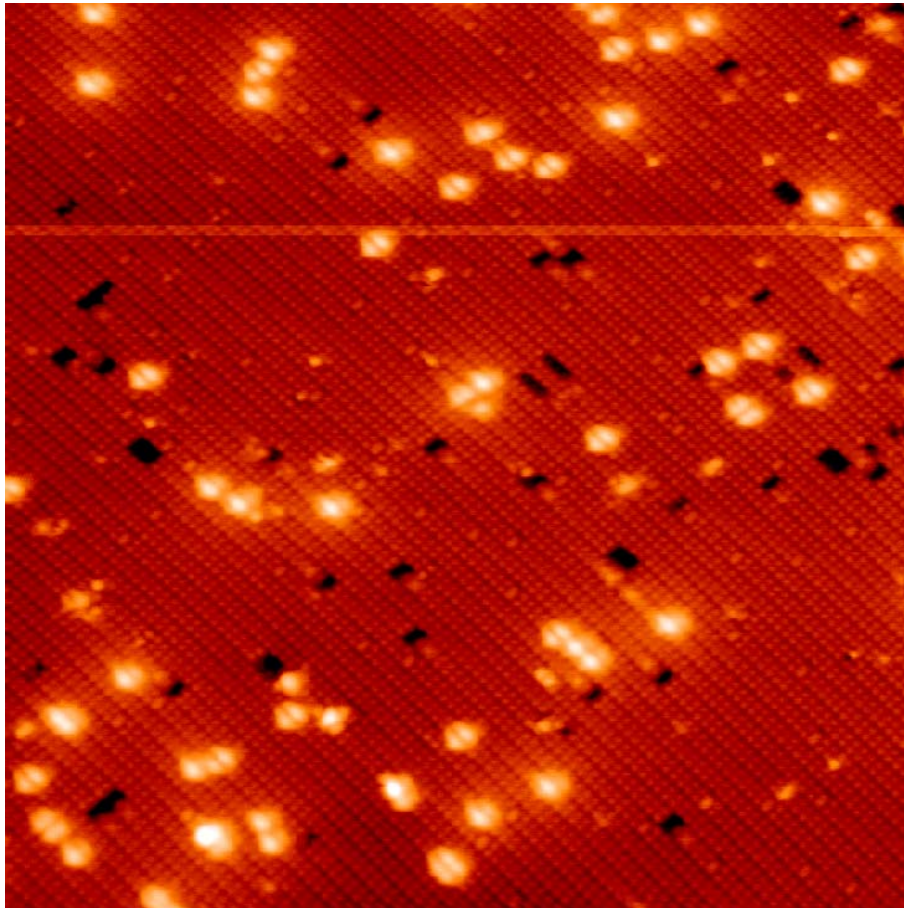


Fig. 2.4 STM image of (a)-(c) clean Si(100) surface at 7 K with sample bias of -2, 1, 2 Volt. (d) H/Si(100)-(2 × 1) surface with several dangling bonds.

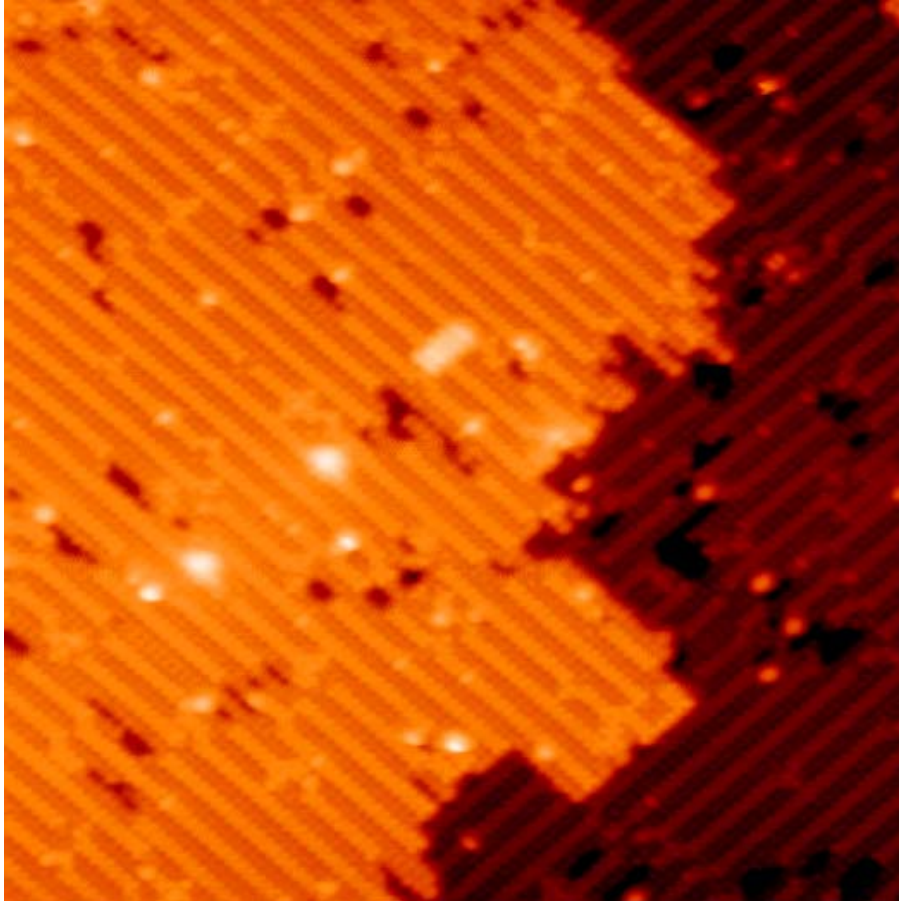


Fig. 2.5 STM image of H/Si(100)-(3 × 1) surface.

2.5 Nanostructuring

The nanostructuring which were performed by STM on H/Si(100) surface through inelastic electron scattering mechanisms has been studied for several years [9, 10]. This technique can create localized reactive sites for exposing interesting molecules and the surrounding H-terminated area remaining unreacted. The desorption mechanism involves multi-quantum vibrational excitations of the H-Si bond under conditions of relatively high current and low energy tunneling electrons. In this thesis, the nanofabrications were created by an Omicron Nanostructuring program. The typical bias and current used for hydrogen desorption were 4.0 eV and 4.0 nA. The moving speed of the tip was 30-200 nm/ s. To fabricate a well-confined dangling bond lines, STM tip must be cleaned by making several times tip-forming until an empty state image with atomic resolution could be acquired. To overcome thermal drift, the tip must move along the scanning direction during nanostructuring, horizontal in our case as schemed in Fig. 2.6. Fig. 2.7 shows two dangling lines perpendicular to the dimer row direction, and Fig. 2.8 shows array of dangling bonds spread along the dimer row direction.

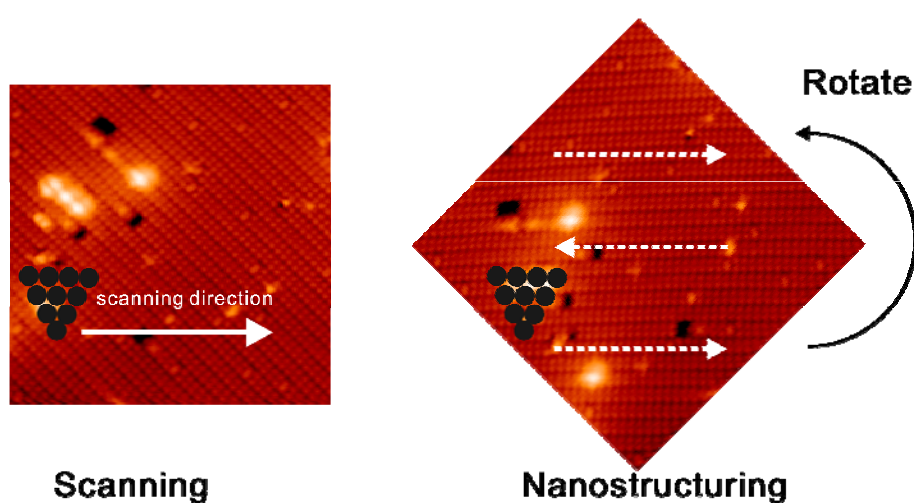


Fig. 2.6 Schematic illustration showing nanostructuring on H/Si(100) surface.

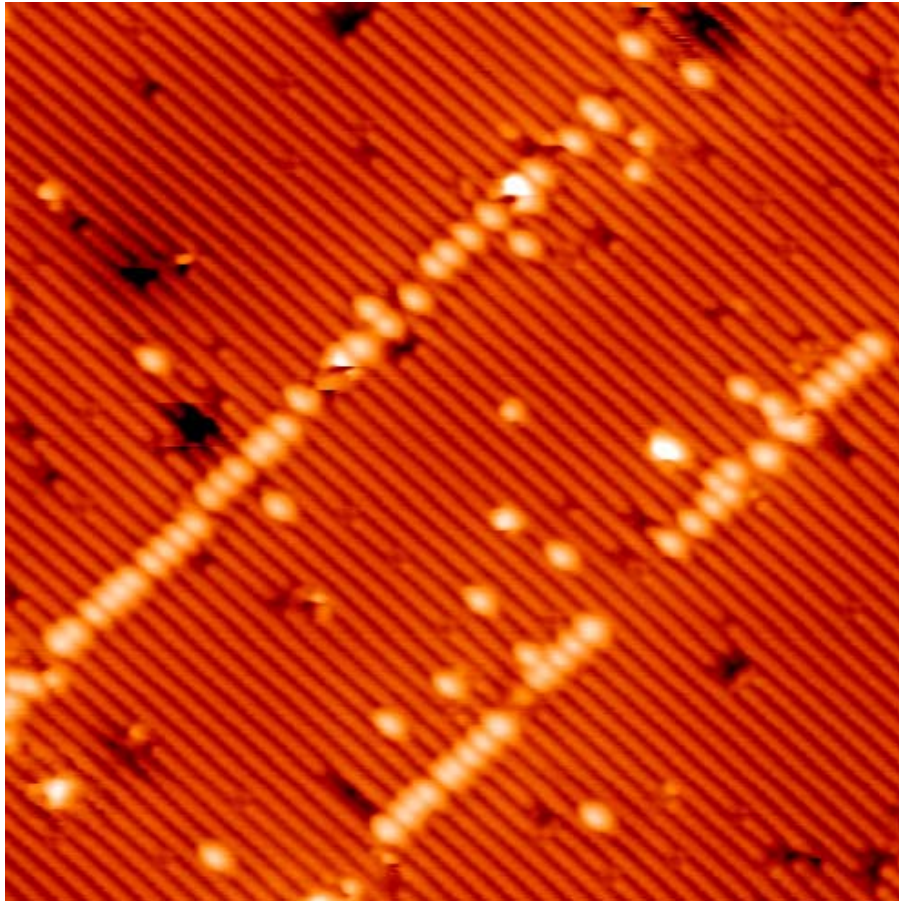


Fig. 2.7 Two DBs chains was fabricated on a H terminated Si(100) with a current–voltage pulse of +4.0 V/3.3 nA.

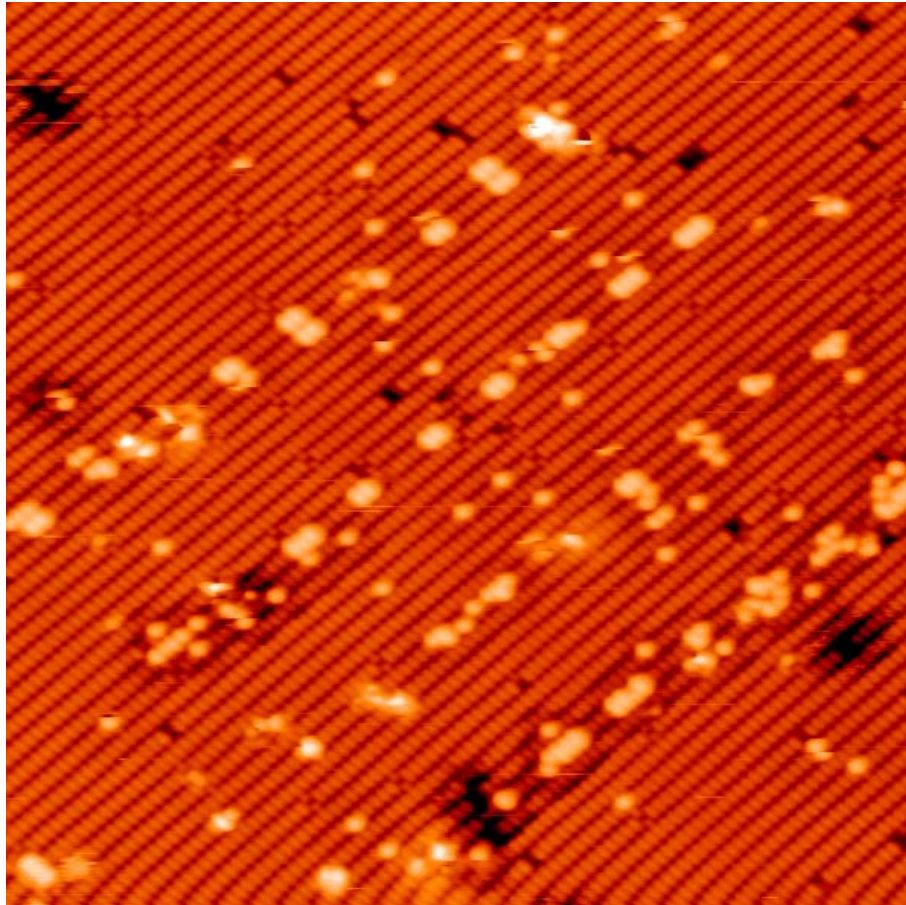


Fig. 2.8 Array of DBs was fabricated on a H terminated Si(100) with a current–voltage pulse of +3.8V/4.5 nA.

Chapter 3 Atomistic View of the Recombinative Desorption of H₂ from H/Si(100)

3.1 Introduction

Recombinative molecular desorption from a surface generally requires the assembly and organization of constituent atoms or molecular fragments on the surface into favorable precursor or predesorption configurations that are compatible with the free molecular shape [11,12]. Geometric constraints can play an important role in the pathway leading to a predesorption configuration, and this subject matter is of fundamental interest to surface physics and chemistry. In this Chapter, we discuss a study with scanning tunneling microscopy (STM) of the relevant atomistic issues associated with the desorption of H₂ from hydrogenated Si(100) surfaces. Being a simple model system, H/Si(100) has attracted intense interest, both experimentally and theoretically [13,14,15,16,17,18]. A detailed understanding of this system is also important from the technological point of view, as hydrogen termination and desorption are often employed in Si device processing. The key question is how two H atoms on H/Si(100) can organize themselves into a state conducive to recombination and desorption. The underlying principles are straightforward, as we shall demonstrate: the two H atoms must move sufficiently close to each other, and subsequent desorption must not leave behind a highly unstable surface configuration.

The relevant geometries are indicated schematically in Fig. 3.1(a)-Fig. 3.1(c). The clean Si(100) surface forms a (2 × 1) reconstruction consisting of parallel rows of dimers. Each surface Si atom has one dangling bond, and saturation of these dangling bonds with H leads to a (2 × 1) monohydride surface (or M—M, where M stands for H—Si). Further H adsorption breaks the dimer bond. With each Si surface atom accommodating two H atoms, a fully

H-saturated surface is a (1×1) dihydride (D) surface [19,4 ,20]. There also exists an intermediate (3×1) phase in which rows of monohydride dimers are interlaced with rows of dihydrides (D(M–M)) [19,20,21,22,3]. Theory has shown that the (3×1) phase is more stable than separate (1×1) dihydride and (2×1) monohydride regions or other periodic patterns, but the free energy difference is relatively modest [23]. Experimentally, antiphase domain boundaries are commonly found on the (3×1) surface, which can be in the form of two adjacent monohydride dimer rows or two adjacent dihydride rows.

The coverage of H on the ideal (2×1) , (3×1) and (1×1) phases on Si(100) is 1, 4/3 and 2 ML, respectively ($1\text{ML} = 6.8 \times 10^{14}$ atoms/cm²). Hence, the pathways of desorbing surface hydrogen involve the structure phase transitions between the $(1 \times 1) \rightarrow (2 \times 1)$ and $(3 \times 1) \rightarrow (2 \times 1)$. While atomic H flux is commonly used to surface chemisorption, hydrogen desorbs molecularly. Therefore, the two transitions are mainly governed by the H₂ recombinative desorption from the monohydride and/or dihydride species. In this chapter we show experimentally that desorption from the (1×1) dihydride phase involves a pair of neighboring dihydrides linked along the tetrahedral bond direction: $\text{DD} \rightarrow \text{M} - \text{M} + \text{H}_2$. The $(3 \times 1) \rightarrow (2 \times 1)$ transition was first observed at 575 K by low-energy electron diffraction [24]. Local electron-beam excitation using STM tips was found to induce the creation of local (2×1) subunits on the (3×1) phase at room temperature. Energy barriers of various rearrangement pathways of the $(3 \times 1) \rightarrow (2 \times 1)$ transition following the loss of two H atoms were also calculated on the basis of density function theory [3]. Because dihydrides in (3×1) domains are separated in the tetrahedral bond direction by monohydride dimers, the thermally activated (3×1) to (2×1) transition is geometrically impossible to occur in a single desorption step from a pair of dihydrides. In this study we find that a position switching of dihydrides with neighboring monohydrides takes place before H₂ desorption, and we provide further insight for both phase transitions of H/Si(100)- (3×1) and H/Si(100)- $(1 \times 1) \rightarrow$ H/Si(100)- (2×1) .

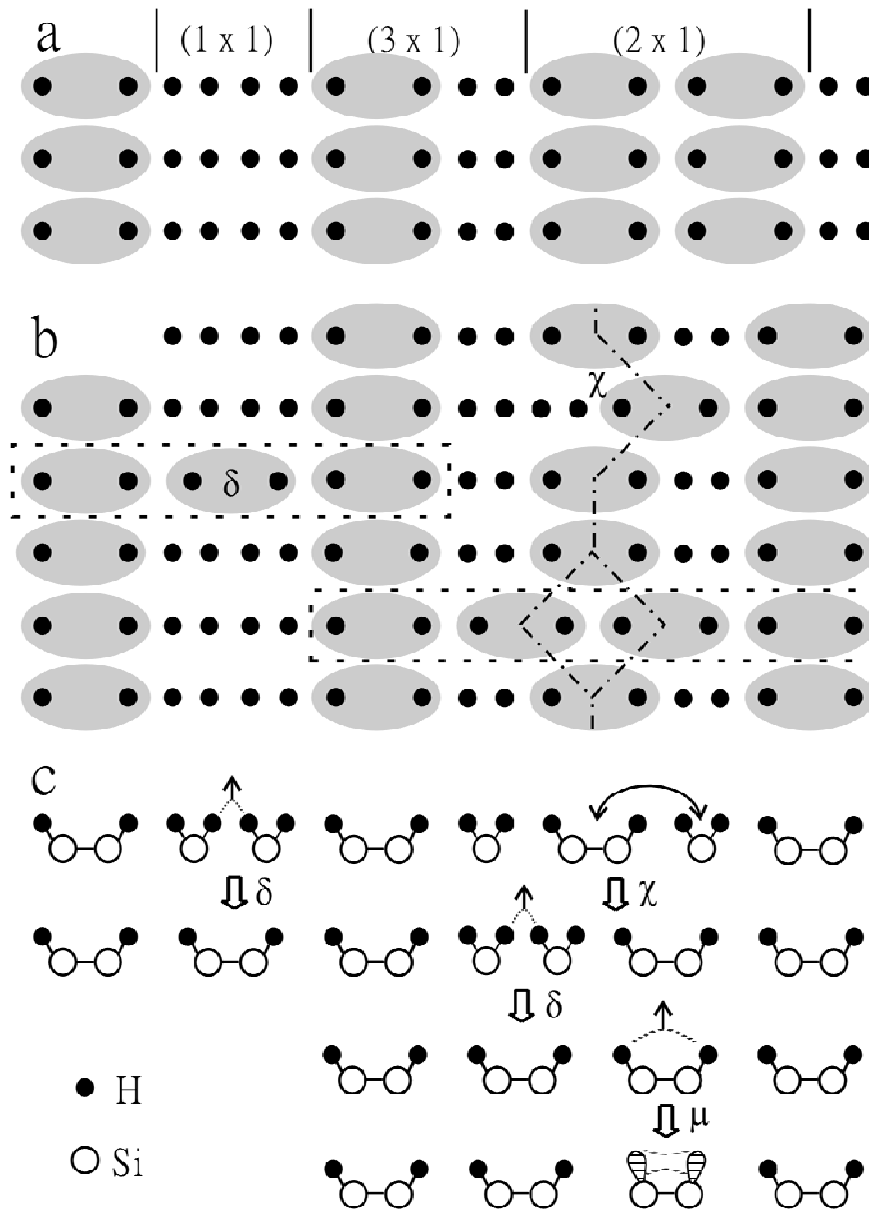


Fig. 3.1 Schematic diagrams showing (a) side and top views of (1 × 1) dihydride, (2 × 1) monohydride, and (3 × 1) mixed monohydride-dihydride phases, and (b) top and (c) side views of atomic configurations involved in χ , δ , and μ reactions as discussed in the text. Dashed rectangles indicate (6 × 1) and (8 × 1) units. Dash-dotted lines outline the V- and diamondshaped structures.

3.2 Experiment

Our experiments were performed using a scanning tunneling microscope in an ultra-high-vacuum chamber with a base pressure of 1×10^{-10} Torr. Si(100) samples were mounted on holders made of Ta and Mo. Both the sample holders and the samples were out-gassed for 12 h at 900 K. The starting clean Si(100)-(2 × 1) surfaces were prepared by brief direct Joule heating at ~1400 K with subsequent radiation quenching. Atomic hydrogen was produced by backfilling the chamber to a background pressure of 2×10^{-7} Torr in the presence of a 1800 K tungsten filament, installed ~5 cm away from the sample. The flux of atomic hydrogen was not measured, and the exposure was recorded in terms of the background dosage of H₂ inside the chamber. A mixed dihydride and monohydride structure is generated by dosing 120 L hydrogen at ~400 K on the H/Si(100)-(2 × 1) surface that was beforehand prepared by dosing 90 L hydrogen on a clean Si(100)-(2 × 1) surface at 600 K [24]. An indirect heating stage with a thermal couple is used for the phase transition at 570 K. All STM images were taken at room temperature with a constant current mode. Various bias voltages were employed as an aid for positive identification of the different surface species. All images presented below were taken at a sample bias of +2.3 V unless otherwise stated. The size of a 1 × 1 unit cell in the image is $3.84 \times 3.84 \text{ \AA}^2$.

3.3 Results and Discussion

3.3.1 Recoinitative desorption of H₂ from H/Si(100)

Figure 3.2 shows representative STM images for a (3 × 1) surface after annealing for 0, 0.5, 4.5, and 33 h, respectively, at 570 K, which is barely above the threshold for desorption. The initial (3 × 1) surface is fairly well ordered, with some randomly located antiphase domain boundaries. Figure 3.2(d) shows that after 33 h anneal the surface is essentially completely converted to a monohydride (2 × 1) surface. In the process, H in the amount equivalent to nominal 1/3 of a Si monolayer is desorbed. Since the dimer rows for the initial (3 × 1) reconstruction and the final (2 × 1) reconstruction are organized with different periodicity, the conversion must involve dimer row reorganization. A detailed examination of the STM images at intermediate stages of desorption reveals that two kinds of reactions are happening as described below.

First, let us focus on a domain boundary involving a local (1 × 1) patch consisting of two adjacent dihydride rows, as shown in Fig. 3.3(a), which is an unoccupied-state image obtained after annealing for 0.5 h. Here, one can see two cases of recombinative desorption. In each case, two adjacent dihydrides donate one H each to form a desorbing H₂ molecule, leaving behind a monohydride dimer. This process, referred to as the δ process, is schematically illustrated on the left side of Fig. 3.1(b) and Fig. 3.1(c). The resulting surface structure consists of three adjacent monohydride dimers stringed along the dimer bond direction. For simplicity, we shall refer to this as a (6 × 1) unit. Desorption from a single dihydride is never observed; the reason is that the end product would be a Si surface atom with two dangling bonds, which is energetically unfavorable. Likewise, desorption does not occur for two adjacent dihydrides lined up perpendicular to the dimer bond direction. This dihydride-pair desorption (δ) process accounts for the conversion of (1 × 1) patches into monohydrides, but is incompatible with the (3 × 1) geometry because the dihydrides are separated along the tetrahedral bond direction by

monohydride dimer rows.

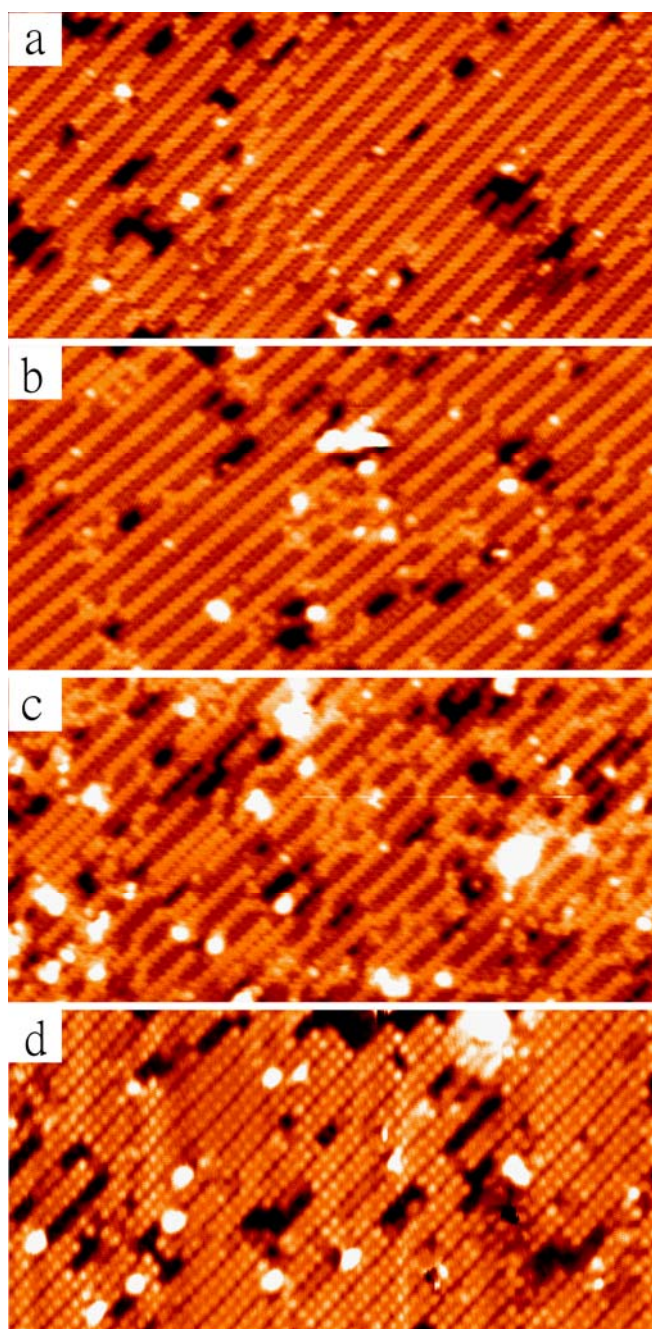


Fig. 3.2 STM images taken at room temperature after a (3×1) sample has been annealed at 570 K for (a) 0, (b) 0.5, (c) 4.5, and (d) 33 h. The dark pits are single or double vacancies. In (a)–(c), the brighter rows are monohydrides and the darker rows are dihydrides.

The other kind of reaction, referred to as the χ process and schematically indicated in Fig. 3.1(b) and Fig. 3.1(c), occurs in ordered (3×1) areas. An example is shown in Fig. 3.3(b), taken after 0.5 h of annealing. Here, a monohydride dimer is seen to switch its position with its neighboring dihydride, resulting in a V-shaped kink in an otherwise straight row. As theory indicates, the barrier involved in this switch is actually quite low [25]. The resulting configuration can be considered as a combination of two adjacent antiphase defects. This antiphase defect pair (ADP) contains two adjacent dihydrides, and can therefore desorb via the same δ process as discussed above and illustrated in Fig. 3.1(b) and Fig. 3.1(c). Indeed, STM images taken at inter-mediate annealing times show a number of such reaction products. An example is shown in Fig. 3.3(c). This two-step desorption process ($\chi + \delta$) leads to a local surface geometry consisting of four monohydride dimers stringed along the dimer bond direction, resulting in an overall diamondlike shape in the image. This is referred to as an (8×1) unit in the following.

A counting of the STM images after 1.5 h of annealing shows that there are more ADPs than (8×1) units with a ratio of about two. This is consistent with the low energy barrier for the formation of ADPs (the χ process), and the rate of desorption appears to be dominated by the dihydride-pair recombination (δ) process. Further evidence is provided by earlier temperature-programmed desorption (TPD) studies which have shown two desorption peaks: a β_2 peak at about 680 K (with an onset near 570 K) corresponding to the conversion of dihydrides to monohydrides, and a β_1 peak at about 790 K corresponding to the conversion of monohydrides to the clean Si(100)- (2×1) surface [4,26]. The β_2 peak appears identical for both the (1×1) and the (3×1) surfaces, suggesting that the geometrical barrier

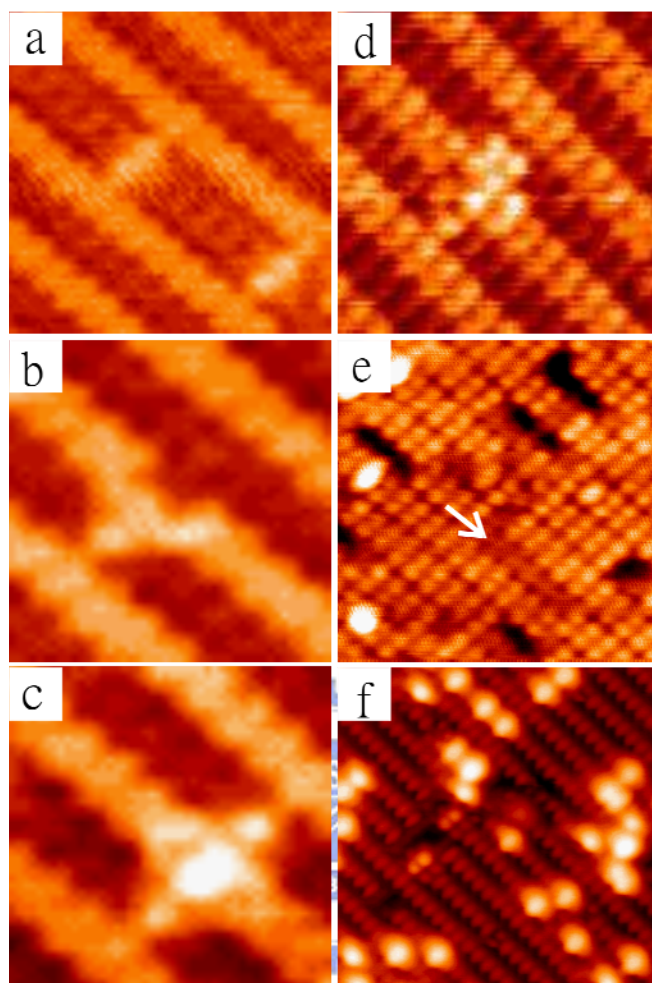


Fig. 3.3 Closeup images showing (a) two (6×1) units formed as a result of the δ desorption process in a two-row-wide (1×1) dihydride domain, (b) a V-shaped kink (ADP) resulting from a position-switching χ process and (c) a diamond-shaped (8×1) unit resulting from combined χ and δ processes, (d) an ADP neighboring an (8×1) unit, (e) a dihydride row trapped in a 2×1 domain, and (f) desorption (μ) events from a monohydride (2×1) phase. Image (f) was taken at a sample bias of -2.1 V, while all of the others were taken with +2.3 V. Images (a)–(d) were taken after annealing a (3×1) sample at 570 K for 0.5 h, while image (e) was taken after a 33 h anneal. Image (f) was taken after annealing a (2×1) monohydride surface for 1 min at 725 K.

for desorption from the (3×1) surface does not play a significant role in the desorption energetics.

As the annealing progresses, further desorption appears to favor sites next to where desorption has already occurred. An example is shown in Fig. 3.3(d), where an (8×1) unit is neighbored by an ADP, and the resulting pattern is closely matched by a combination of the two features shown in Fig. 3.3(b) and Fig. 3.3(c). With continued desorption, (8×1) and (6×1) units tend to expand into $(8 \times n)$ and $(6 \times n)$ patches. Since the initial (3×1) surface also contains (4×1) units in antiphase domain boundaries, the overall surface structure can become fairly complicated as domains form, grow, and merge, as seen in Fig. 3.2(c). The complicated domain patterns eventually give way to a simple monohydride surface with an overall (2×1) reconstruction as seen in Fig. 3.2(d). However, cases are found where a single row of dihydrides gets trapped in large patches of (2×1) monohydrides, and an example is shown in the image in Fig. 3.3(e). These features are relatively rare, but are robust as desorption can no longer proceed via the same two-step mechanism.

Some prior studies have suggested recombination involving two H atoms from a single dihydride unit as an important or dominant contribution to desorption [26,27,28]. Such a process would lead to a bare Si atom on the surface with two dangling bonds, which is highly unstable, and our study shows that this does not occur. A single row of dihydrides trapped within a (2×1) monohydride domain can be considered as a kind of (2×1) antiphase (or twin) domain boundary. It is interesting to note that this type of antiphase domain boundary has never been observed on clean (2×1) surfaces apparently to avoid bare Si atoms with double dangling bonds. For the present system, such boundaries form due to reaction kinetics and stabilization by hydrogen termination. In Fig. 3.2(a)-3.2(d), significant numbers of single vacancies and double vacancies form short chains and/or clusters. The initial vacancies of $\sim 4\%$ of the surface area result from etching during the atomic H exposure [29]. Up to $\sim 4\%$ more vacancies could be found after annealing at 570 K. These vacancies presumably result from the formation and

desorption of Si_2H_2 and SiH_4 [30,31]. These etching processes could account for some reduction of surface hydrogen during the (3×1) to (2×1) phase transformation.

Significant desorption from the monohydride phase requires a higher temperature. An example is shown in Fig. 3.3(f) where a monohydride surface has undergone annealing at 725 K for a minute. This temperature falls within the width of the β_1 peak. The bright spots indicate where desorption has occurred. A careful inspection of the surface at different bias conditions reveals that the desorption involves a pair of H atoms from a single monohydride dimer. The process, referred to as the μ process and schematically indicated in Fig. 3.1(c), is consistent with the notion that desorption must involve two nearby H atoms which can easily move close to each other (through bond flexing in the present case). Our results for monohydride desorption are consistent with prior observations [32,33].



3.3.2 Evolution of two-dimension structure phase transition $(1 \times 1) \rightarrow (2 \times 1)$ and $(3 \times 1) \rightarrow (2 \times 1)$.

Following procedures developed previously, as Fig. 3.4(a) displays, a typical surface so prepared consists of (3×1) domains (purple) and small areas with (2×1) (green) and (1×1) structures. The dark pits, having a depth of about one monolayer, were single or double vacancies depending on their width. The (3×1) domains are separated by vacancies and three kinds of characteristic antiphase boundaries, which possess local (1×1) , (2×1) and (3×1) order, respectively. In consistence with a previous study, the local (1×1) domains consist of no more than two dihydride rows because of the repulsive interaction between dihydride units. Also, vacancy clusters persist on the surface as a result of etching [21].

Fig. 3.4(b)–Fig. 3.4(d) show STM images of a hydrogen terminated Si(100) surface after annealing at 570 K for 0.5, 4.5, and 33 h, respectively. The annealing temperature is barely above the threshold for desorption [4,26]. The coverage of various phases as a function of annealing time is displayed in Fig. 3.5. Although desorption of SiH_4 and SiH_2 molecules as etching products and refilling of desorption sites by mobile surface Si species could have occurred [30,31]. Fig. 3.4 and Fig. 3.5 show that these effects do not lead to obvious variations in the distribution and density of vacancies within a few percents of statistical uncertainty. Thus, annealing does not significantly induce surface etching; instead, it slowly converts both the (1×1) and (3×1) phases to (2×1) by desorbing hydrogen.

The atomic details of the structure transformation from mixed dihydride and monohydride to the monohydride (2×1) phases have been discussed above. Briefly, desorption from dihydrides involves a pair of neighboring dihydrides linked along the tetrahedral bond direction, i.e., $\text{DD} \rightarrow (\text{M}-\text{M}) + \text{H}_2$. The same desorption mechanism applies to the (3×1) domains via first a position switch of dihydrides with neighboring

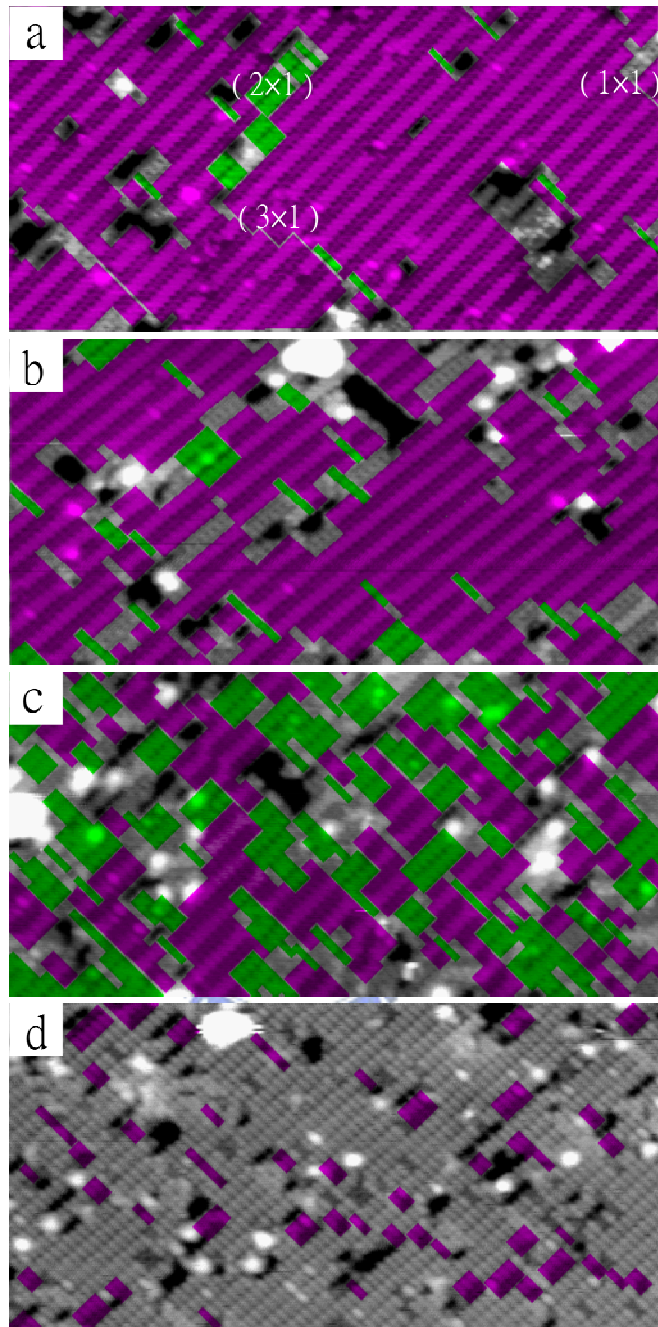


Fig. 3.4 Time evolution of H/Si(100) observed through STM images taken at room temperature after sample was heated at 570K for (a) 0, (b) 0.5, (c) 4.5, and (d) 33 h. The initial H coverage was about 1.4 ML. The (3×1) and (2×1) areas are colored purple and green, respectively, except in (d) for the sake of clarity. The dark pits are single or double vacancies.

monohydrides, i.e., $D(M-M)D(M-M) \rightarrow DD(M-M)(M-M) \rightarrow (M-M)(M-M)(M-M) + H_2$. The switch of adjacent monohydride and dihydride species in a (3×1) domain results in two dihydride species lying side by side along the Si-H bond directions. Although several bonds (Si-H and Si-Si) are involved, the energy barrier of this switching reaction is calculated to be only ~ 1.6 eV which is in reasonable agreement with that estimated from the reaction temperature of 570 K [25].

The initial switch (χ) reaction occurs randomly, leading to the random emergence of local (2×1) ordering in the (3×1) domains, as Fig. 3.4(b) demonstrates. Fig. 3.6 shows that the transition sites exhibit no notable preference near antiphase boundaries, steps or defects. The switch and the subsequent H_2 desorption in (3×1) domains creates local (2×1) domains of sizes $(n \times 8)$. The (2×1) domains of monohydride dimers due to H_2 desorption from the (1×1) , i.e., $(M-M)DD(M-M) \rightarrow (M-M)(M-M)(M-M) + H_2$, have sizes of $(n \times 6)$. The antiphase boundaries of two (3×1) domains along the dimer rows' direction, $D(M-M) + (M-M)D$, consist of two monohydride dimer rows lying side by side and are exhibited as islands of sizes $(n \times 4)$. These three kinds of local (2×1) domains (green) are dispersed in the (3×1) domains (purple), as Figs. 4(b) and 4(c) display.

Apparently, the two-step H_2 desorption reactions prefer slightly the ends of (2×1) dimer rows, causing the (2×1) domains to extend in the dimer row direction and the (3×1) domains to shrink, as Fig. 3.4(c) and Fig. 3.4(d) show. As annealing continues, the (2×1) areas grow and coalesce into larger domains while new clusters of (2×1) dimers continue to emerge at the expense of the (3×1) and (1×1) domains, as shown in Fig. 3.4(c) and Fig. 3.4(d). The exponential form of the growth of (2×1) domains and the decay of (3×1) and (1×1) domains suggest an approximately linear growth/decay behavior. A standard curve fitting gives decay constants of 0.070 and 0.071 or equivalently half-lives of 9.9 and 9.8 h for the (1×1) and (3×1) domains, respectively, at 570 K. Since the decay constant is very sensitive to the change in activation energy, the similar decay constants for the two phase transformations strongly

suggest that they share a common fundamental and dominant mechanism. As discussed, the $(1 \times 1) \rightarrow (2 \times 1)$ transition takes place via direct H_2 recombinative desorption from two neighboring dihydrides, while the $(3 \times 1) \rightarrow (2 \times 1)$ transition requires a switching reaction before the common H_2 desorption from dihydrides. The dominant mechanism is, therefore, the common H_2 desorption, not the switching reaction between a dihydride radical and a monohydride dimer. This conjecture suggests a faster switching mechanism, a slower desorption mechanism, and the existence of the intermediate state. Indeed, the intermediate local (1×1) phase consisting a DD dihydride pair after the switching reaction (i.e., near label χ) is commonly observed in the STM images.



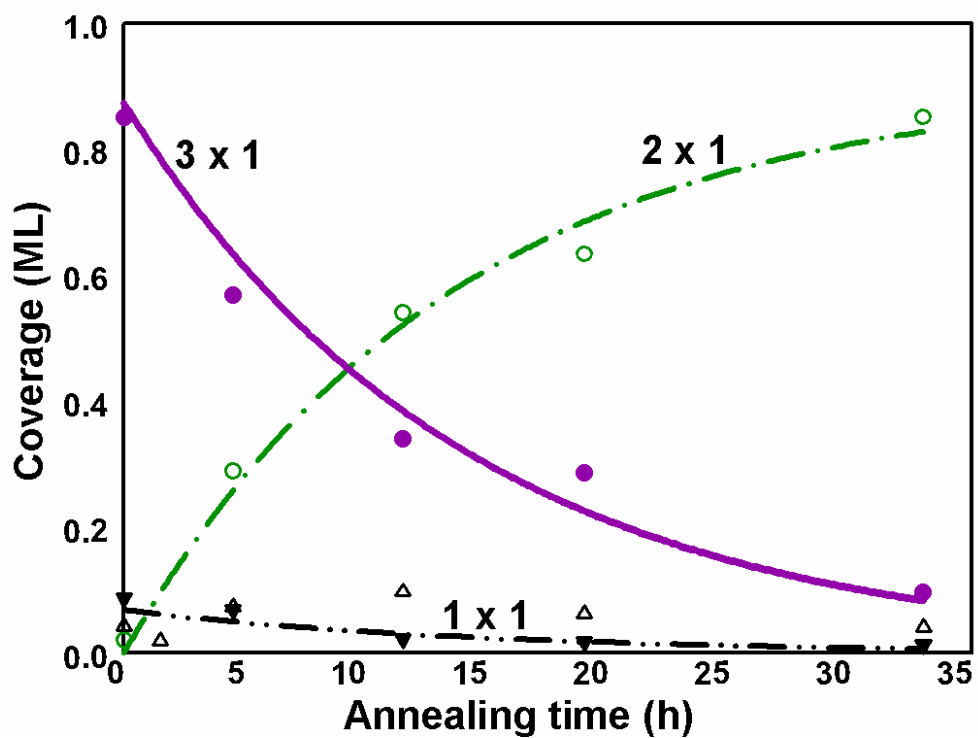


Fig. 3.5 Coverage for vacancies (triangles), (1×1) (filled triangles), (3×1) (filled circles), and (2×1) (open circles) domains as functions of annealing time at 570 K. The fitting curves for the (3×1) , (1×1) and (2×1) domains are $87.4e^{-0.071t}$, $6.8e^{-0.070t}$, and $90.5(1-e^{-0.075t})$, respectively.

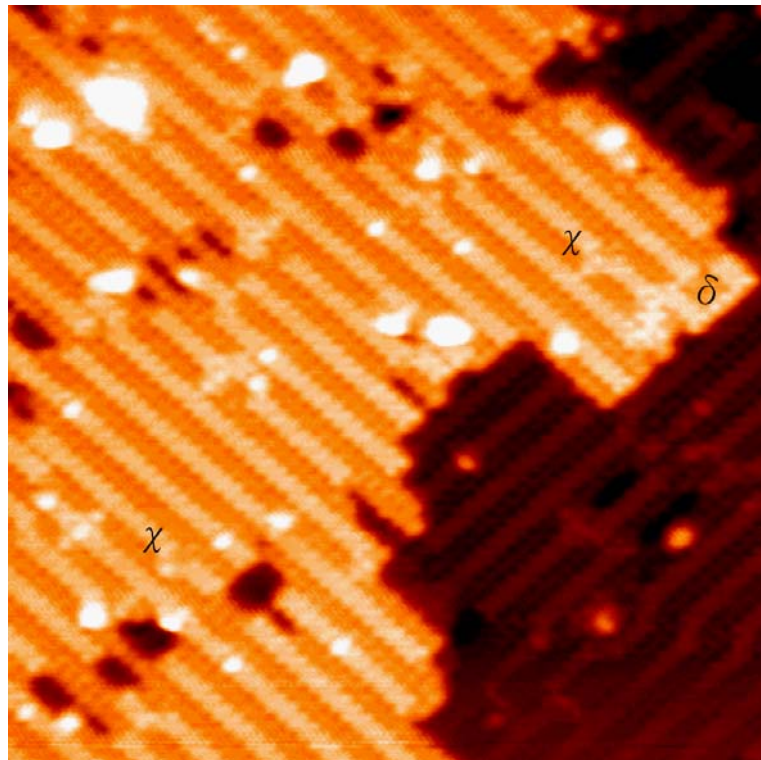


Fig. 3.6 STM image near step edge after nominal H/Si(100)-(3 \times 1) surface is annealed at 570K for 0.5 h. The product of a desorption process from dihydridepair recombination is labeled as δ ; of a position switch process, χ .

3.4 Conclusion

To summarize, we have presented a detailed atomistic view of the desorption of H_2 from $H/Si(100)$ in terms of three processes: δ , χ , and μ . The results illustrate two basic principles relevant to recombinative desorption: the constituent atoms must be organized first on the surface into predesorption states that are compatible with the free molecular geometry, and the resulting surface structure must be energetically favorable. Specifically, desorption from dihydrides proceeds by recombination of two H atoms coming separately from two adjacent dihydrides, leaving behind after the reaction a monohydride dimer on the surface. This process is geometrically forbidden for the (3×1) surface, but becomes possible with a switch of a dihydride with a neighboring monohydride dimer to form an ADP structure. Desorption from monohydrides occurs at a higher temperature, and proceeds by recombination of the two H atoms on a given monohydride dimer. Bare Si atoms with two dangling bonds are never observed, and the allowed surface states include just dihydrides, monohydrides, and clean Si dimers. For the performed real-space measurements on the structure evolution during hydrogen reduction from 1.4 to 1.0ML in phase transition from mixed (3×1) and (1×1) phases to (2×1) phase at 570 K. Both the initial (3×1) and (1×1) domains linearly decay with a common half-life time of ~ 9.8 h. These findings together suggest that the (3×1) structure first transforms to the local (1×1) structure before the dominant dihydride-pair recombination mechanism occurs.

Chapter 4 Unsaturated Characteristic of the I/Si(100) Surface via Dissociative Adsorption Mechanism

4.1 Introduction

The adsorption of diatomic molecules onto the surface is scientifically and technologically important. This subject has been studied using various surface analysis techniques over the years [34,35,36,37,6,5]. Two basic chemisorption categories are reported: dissociative adsorption and abstractive adsorption. For the dissociative adsorption, the molecule sticks to the impinging surface as a precursor-state. An activation barrier may or may not present for the molecular bond broken and chemical bonded. In an abstractive adsorption, one atom of the molecule is adsorbed upon hitting surface, with the other atom either leaving the surface or migrating to a nearby area to cause further reactions. Abstractive adsorption frequently occurs when the energy released by the adsorbate-surface bond exceeds the binding energy of the molecule. For halogen gas, the high exothermicity of F₂, Cl₂, and Br₂ abstractive adsorption on Si surface had been studied by Li et al. and Kummel et al.. A saturated surface with 1 ML coverage were also reported [36,38,7]. In contrast to others halogen gas, abstractive adsorption of I₂ on Si(100) surface has not been observed due to low energy released. In this paper, we will show that the adsorption of I₂ on Si(100) surface is dominant by dissociative mechanism.

With dissociative mechanism as a only process for adsorption, one can expected some un-bonded sites are present after randomly adsorption of diatomic molecules on uniformly distribute surface surface dangling bonds. Nord and Evans showed a maximum coverage of 0.9 ML for dimers irreversible filling on a square lattice [39]. In our study, an unsaturated surface with maximum coverage of 0.92 ML was observed for the I₂ adsorption on Si(100)-(2

$\times 1$) surface. We also discuss the origin of nonreactive 0.08 ML single dangling bonds (SDB). Some of these SDBs are very separated by a short distance and remain on the surface after large I_2 exposure. The maximum distance between two isolated SDBs allowed for I_2 dissociative adsorption is derived from series SDBs pairs on H/Si(100) surface.



4.2 Experiment

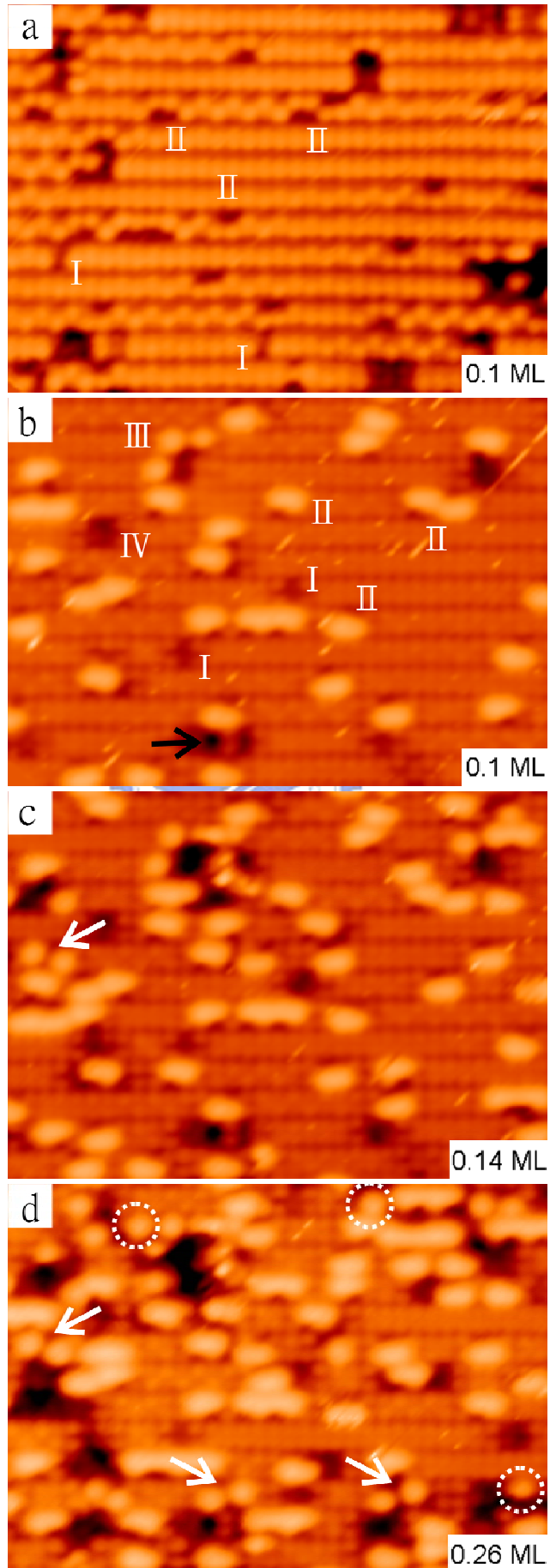
Our experiments were performed using a scanning tunneling microscope in an ultra-high-vacuum chamber with a base pressure of 1×10^{-10} Torr. Si(100) samples were mounted on holders made of Ta and Mo. Both the sample holders and the samples were out-gassed for 12 h at 900 K. The starting clean Si(100)-(2 × 1) surfaces were prepared by brief direct Joule heating at ~1400K with subsequent radiation quenching. Atomic hydrogen was produced by backfilling the chamber to a background pressure of 2×10^{-7} Torr in the presence of a 1800 K tungsten filament, installed ~5 cm away from the sample. The solid I₂ was purified by freeze-pump-thaw cycles before use and I₂ vapor was introduced into the chamber through a precision leak valve. In the chamber, a quartz tubing is set up to guide I₂ vapor directly to the sample, the distance from the sample to the end of quartz tubing is 1 inch. So, the pressure indicated by ion gauge is the partial pressure of I₂ in the chamber that is much smaller than the dosing on the sample. The H/Si(100) substrate with single and paired DBs were prepared by unsaturated H₂ dosing surface or annealed surface, these DBs were exposed to I₂ for discussing I₂ dissociative mechanism. Halogen gas dosing and STM images acquiring were done at room temperature.

4.3 Results and Discussion

4.3.1 I₂ dissociative adsorption on Si(100) surface

Fig. 4.1(a) and Fig. 4.1(b) shows filled and empty state image taken after I₂ exposure to iodine coverage ($\theta(I) \sim 0.1$ ML) at room temperature, some brighter and dimmer features comparing to clean surface are observed. Adsorption of diatomic molecular on Si(100) surface typically occurs in two configurations: on a single Si dimer or at the same side of adjacent dimers in the same dimer row [40,41]. These configurations are referred to as type I and II sites, zoom-in images and schematic illustration are shown in Fig. 4.2(a). For the type I feature, I₂ filled dimer is dim and flat, and can be distinguished from dimer vacancy with fitting color scale as a black arrow indicated. The Si dimer neighboring to type I site are untilted and with better resolved than surrounding dimers, this untilted characteristic is due to an elastic strain induced by neighboring I₂ filled dimer. The other feature, type II adsorption site is imaged as bright bean-shaped features in emptied state image. The dim side is attributed to I₂ bonding sites, the other sides are two unpaired Si dangling bonds (DB). The bonding sites of type I and II configurations are closed and in pair, this can be the result of dissociative adsorption. Several type I and II adsorption sites are labeled in Fig. 4.1(a) and Fig. 4.1(b).

In contrast to type I and II configurations that two atoms are bonding on adjacent DB, several isolated single DBs (SDB) are also present in Fig. 4.1(b). A zoom-in image is displayed in right side of Fig. 4.2(a) and referred to as type III configuration. This configuration can a result of abstractive adsorption. Only one I atom forms a chemical bond on the impinging position while the other atom bounces back to vacuum or migrates to a nearby area after molecular bond cleavage.



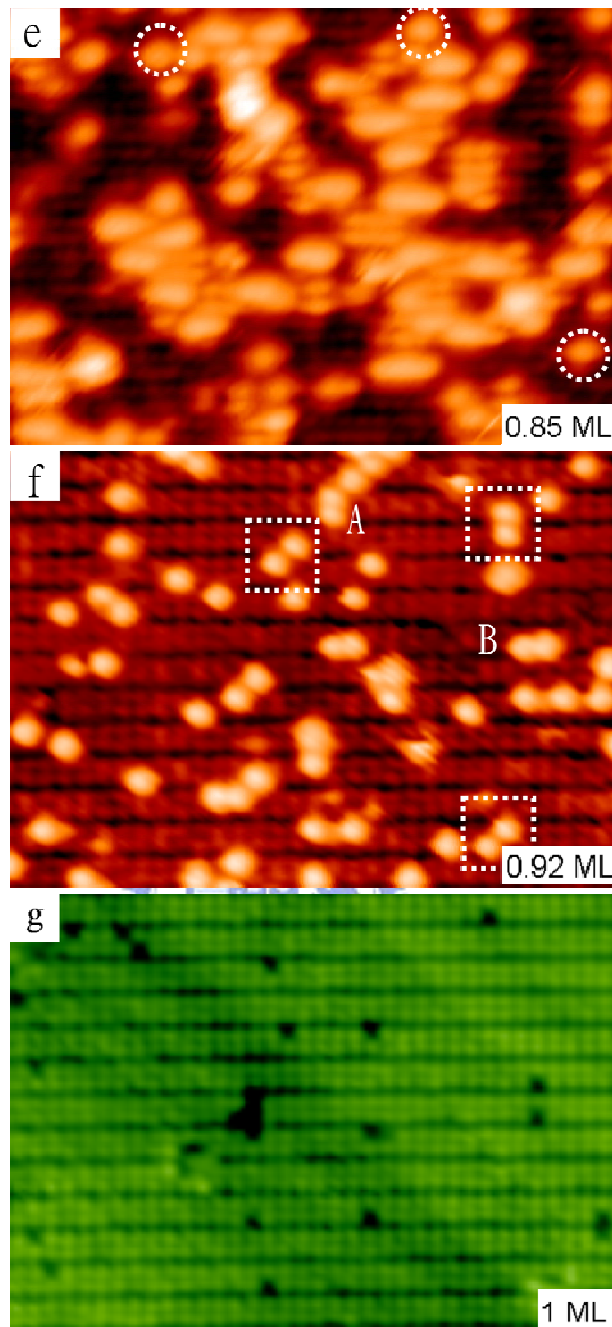


Fig. 4.1 STM images showing I_2 adsorption on the Si(100) surface at coverage $\theta(I) =$ (a) 0.1, (b) 0.1, (c) 0.14, (d) 0.26, (e) 0.85, and (f) 0.92 ML. (a) Filled and (b)-(e) empty state images. The numbers I to IV in (a) and point out four typical adsorption sites at low coverage, and black arrow shows a dimer vacancy. The white arrows in (c) and (d) show the crossed type II configuration, and circles mark several stable isolated SDBs. The squares in (f) show several DBs that are on neighboring dimers. (g) A saturated surface after exposing to Cl_2 . The STM sample bias are (a) -1.8, (b)-(e) 1.8, and (f) -2.3 V.

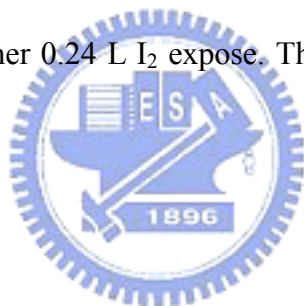
In order to determine which configuration is the dominant adsorption mechanism, in the corner of Fig. 4.2(a) shows the relative percentage for I₂ adsorption into different configurations at low coverage. At $\theta(I) \sim 0.1$ ML, the population of type I, II, and III configurations are 11%, 70%, and 5%. The rest 14% is the feature with four I atoms on two adjacent dimers that could regard as two type I or two type II adsorption events, and named type IV configuration. The statistical result shows that dissociative adsorption is the dominant adsorption mechanism with total population of 95%, type I, II, and IV configurations, much higher than abstractive mechanism, type III configuration.

Additionally, type II adsorption is more favorable at room temperature even though two π bonds are disrupted. Similar results were observed by Boland and Yates for others halogen gas (Cl₂, Br₂, and I₂) [40,7,42,43]. However, a larger population of type I sites was reported by Weaver; this difference in population also noticed by Yates [41,7,44]. We attribute this difference to different I₂ gas source or I₂ generator. In our setup, I₂ vapor was held in a room temperature glass tube and introduced into the chamber through a leak valve without any heating process. However, a solid state electrochemical doser was used to provide I₂ in Weaver's experiment. The requisite operating temperature of doser, around 100°C, can give I₂ more translational energy before impinging surface and the extra thermal energy may allow I₂ overcome energy barrier to form type I configuration. Type I sites were reported to dominate after the surface had been annealed [42,45].

Increasing I₂ dosage, sequential images of the same surface region with $\theta(I)=0.14$, 0.26, and 0.85 ML are presented in Fig. 4.1(c) to 1(e). Fig. 4.3 shows the coverage of I₂ as a function of I₂ exposure. The I₂ dosage is 0.25 L at coverage of 0.85 ML, while the coverage is slightly up to 0.92 ML after further two times I₂ exposure to 0.54 L. The coverage stay at 0.92 ML after further I₂ dosing to 1.14 and 1.56 L, this high dosed surface is shown in Fig. 4.1(f). Some bright features are dangle bonds. These DBs are isolated or somewhat in pairs. This unsaturated surface shows that I₂ adsorption on surface simply via dissociative mechanism

can not terminate surface atoms, and result in maximum coverage of 0.92 ML.

These DBs can be divided into three categories as in Fig. 4.2(b). Most of DBs are isolated with percentage of 93%. The rest are Si dimer or two DBs on neighboring dimers, referred to as type C, A, and B configurations, respectively. These configurations are similar to the features at low coverage surface, as shown in Fig. 4.2(a). However, relatively population and adsorbate-substrate position are reversed. From geometrical point, configuration A and B should not present at high I_2 dosed surface, because these sites can be filled by iodine atom via type I and II adsorption process since they are the dominant process during I_2 adsorption. This result can be attributed to the absence of precursor-mediated adsorption mechanism when most surface atoms are terminated by iodine atom. This decreases the sticking probability of I_2 interaction to A and B sites. For the isolated SDBs, C configuration, these DBs are stable after further 0.24 L I_2 expose. The origin of these SDBs and stability will be discussed followed.



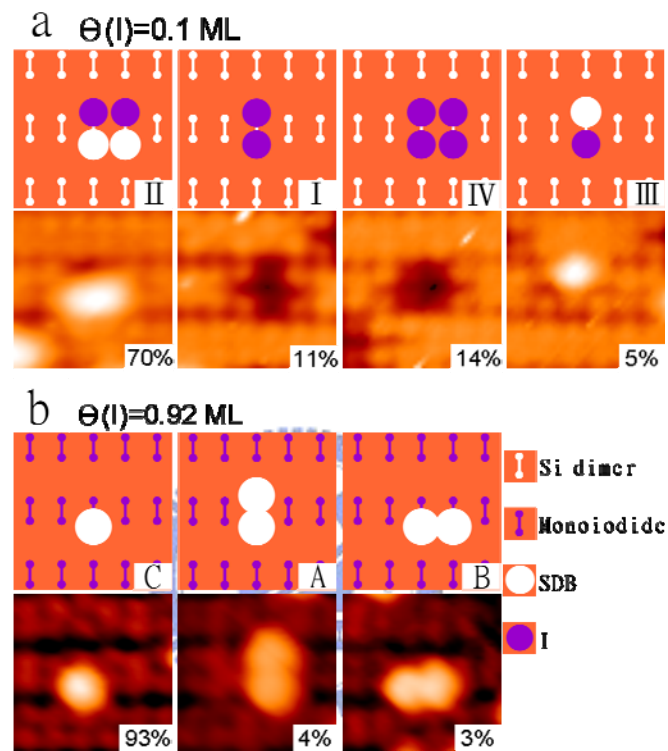


Fig. 4.2 (a) and (b) Zoom-in images showing some configurations that are observed at low and high coverage surface. In the corner shows relative percentage of each configuration.

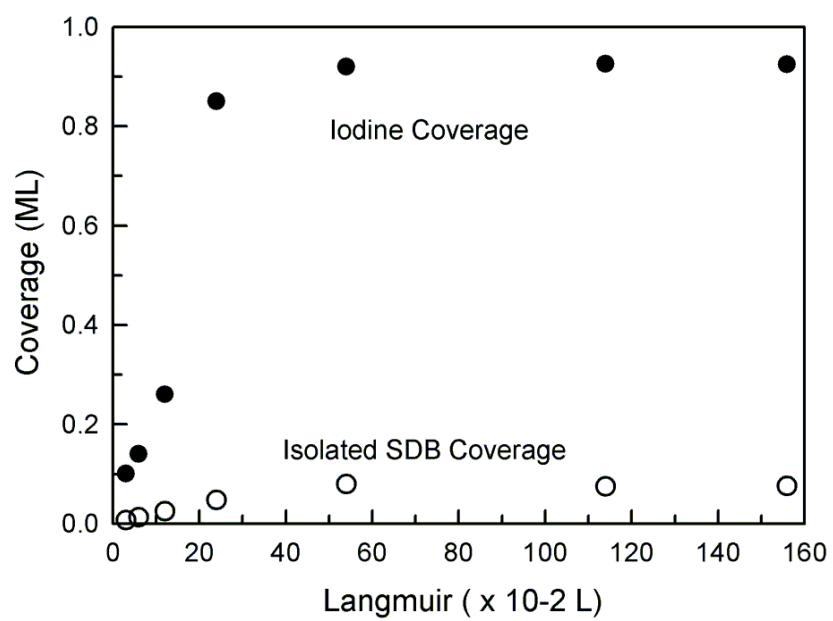


Fig. 4.3 Coverage of iodine and isolated SDB as function of I₂ exposure, the maximum coverage is 0.92 ML.

4.3.2 Presence of isolated single danglings

Back to low coverage surface and comparing the adsorption sites of Fig. 4.1(c) to Fig. 4.1(b), from $\theta(I)=0.14\text{ML}$ to $\theta(I)=0.1\text{ML}$. After analyzed ~ 200 new adsorption sites, around 50% of adsorption sites were isolated type I or II sites, 44% were bonded nearby the original type I or type II sites. The rest 6% are type III configuration. The total number of type I and type II adsorption sites are 12% and 82%, respectively. The detail populations of each configuration are shown in Fig. 4.4(a). Notably, there are two groups that can result in isolated SDBs. One is the 6% type III sites, these SDBs are more or less in pairs and asymmetrically positioned on the same dimer row or neighboring rows as an example at upper left of Fig. 4.1(a) [40]. Thermally activated motion at room temperature was supported by Weaver due to low diffusion barrier for I atom motion on the silicon surface [46]. This mechanism leads to I atoms hopping both along and across the dimer row before chemically bonded. We group these isolated SDBs as type III configuration all together, and attribute the appearance to abstractive adsorption.

The other one is a cross adsorption of two type II sites resulting in two unpaired SDBs on next nearest neighbor dimers, as illustrated in Fig. 4.4(b). The percentage is 4.6% within type II site, an example is pointed with white arrows in Fig. 1(b). This cross adsorption feature is present more as iodine coverage up to 0.26 ML, as white arrows indicated in Fig. 1(c).

Additionally, tip induced rearrangement of type II features into two separated SDBs are also observed since emptied state images were acquired [42,43]. However, not more than 2% of type II sites were excited after comparing original adsorption sites in $\theta(I)=0.1\text{ML}$ to $\theta(I)=0.14\text{ML}$. The probability is rarely because of the bias used here, 1.8 V, is much small than the threshold voltage 2.7 V for excitation that Boland reported. In order to reduce this extrinsic excitation, the tip was moved away from the interesting area during I_2 dosing, and back again after I_2 dosing stopped and pumped. To sum up these isolated SDBs (type III site, crossed

type II site, and tip-excited area), around 12% of isolated SDBs were present during the iodine coverage from $\theta(I)=0.14$ ML to $\theta(I)=0.1$ ML, these isolated SDBs coverage is 0.025 and 0.048 ML, respectively. Most isolated SDBs were produced by abstractive adsorption and crossed type II sites, and could regard as an intrinsic result during I_2 adsorption on Si surface at low coverage.

Tracing isolated single DBs in Fig. 4.1(d) to the same sites in Fig. 4.1(e) after further I_2 exposure, several isolated SDBs are remain on the surface but surrounded by I-terminated surface, as shown by circles. The density of isolated SDBs as a function of I_2 exposure is shown in Fig. 4.3. The coverage of isolated SDBs is 0.05 ML at $\theta(I)=0.85$ ML, and up to 0.08 ML at $\theta(I)=0.92$ ML with double I_2 exposure to 0.54 L, nearly the same SDBs and I_2 coverage after further three times expose to 1.56 L. Fig. 4.1(f) is an image acquiring after 1.14 L I_2 dosed, the image shows around 0.08 ML bright features or isolated SDBs on the surface. These remained isolated SDBs don't interact to I_2 and stop the iodine coverage to go further.

Discussing the adsorption dynamics more detailed, in contract to I_2 form an unsaturated surface, Fig. 4.1(g) shows a Cl-terminated surface acquired by the same experiment condition. This difference is due to different dominant adsorption mechanism. The adsorption of Cl_2 is dominant by abstractive adsorption and can passivate SDBs. A saturated Cl/Si(100) surface and similar discussion also be reported by Yates [7]. While due to low exothermicity to form only one bonding, the adsorption of I_2 is predominantly by the dissociative adsorption. In other words, a cleaving of I_2 molecular bond is allowed only when interaction to two nearby SDBs. Such SDBs must be close enough or comparable to I_2 bond length. The detail adsorption mechanism will discuss in Chapter 5.

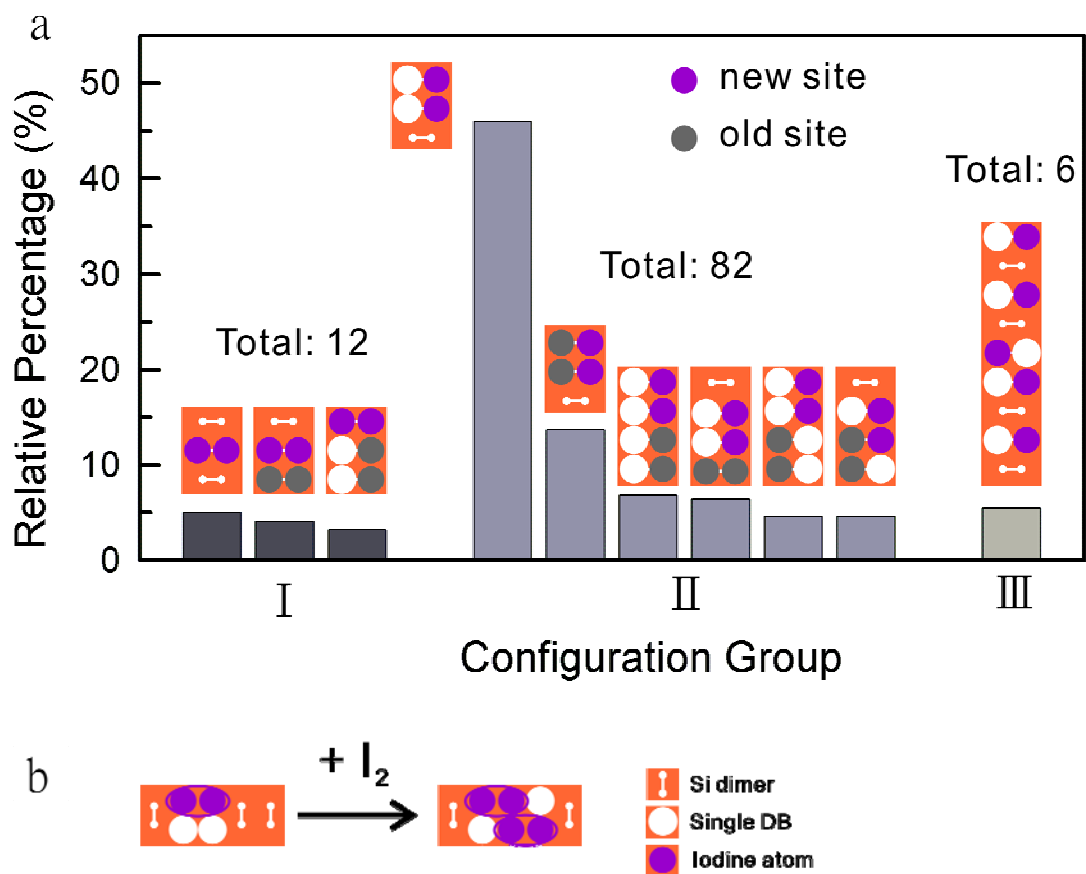


Fig. 4.4 (a) Showing the population of each new adsorption site at $\theta(I)=0.14$ ML comparing to the surface at $\theta(I)=0.1$ ML. (b) Schematic diagram illustrating shows the evolution of crossed type II configuration..

4.3.3 Maximum distance of two reactive sites allowed for I₂ dissociative adsorption

There are 0.08 ML isolated SDBs on the final I/Si(100) surface as discussed above, but some SDBs are very close and simply on the adjacent dimers, as marked by squares. Are these SDBs really blunt to I₂ adsorption? In order to understand the maximum distance of two SDBs for I₂ dissociative adsorption, series of SDBs pairs with different distance are fabricated on H/Si(100) surface. There are two reasons for using H-terminated surface. First, with different surrounding atom, one can identify iodine atom adsorption dynamics clearly. Second, the atomic radius of H atom is half smaller than I atom, this decreases steric hindrance and gives bare DBs for studying dissociative mechanism.



Fig. 4.5 display some DBs with different configurations before and after large I₂ exposure (0.12 L and 1.32 L). The adsorption probability and relatively reactions are also schematic illustrated at bottom. By the way, the bond lengths of I₂ and Si dimer are 2.67 and 2.43 Å, and the size of (2 × 1) structure is 7.68 × 3.84 Å² (2a × a). Fig. 4.5(a) shows the non-reaction of I₂ to SDB. As the result discussed previous, I₂ adsorption is a dissociative process that two nearby SDBs is required. Fig. 4.5(b) to Fig. 4.5(e) show several DB pairs with different distance extended perpendicular to dimer row direction. For I₂ adsorption to DB pairs on one dimer, type I site, an adsorption probability of 1.00 is observed. The result is expectable because type I configuration is most stable from energetics. Next configuration is two SDBs

are at neighboring dimers in different dimer row. The distance is larger than the I_2 bond length. Adsorption of I_2 on this configuration is rarely with probability 0.15 and only one I atom chemical bonded on the SDB. The rest 0.85 SDBs remain on the surface. Enlarging the distance to $2a$, no adsorption event takes place.

Fig. 4.6 demonstrate the adsorption of I_2 on SDBs pairs distributed along the dimer row direction. First configuration is two SDBs at the same side of adjacent dimer with distance of $1a$, type II site. Several adsorption events take place but rearrange adsorption position to bonding on one dimer, the probability is 0.6. The rest 0.4 are the adsorption directly on two SDBs. Fig. 4.6(b) shows I_2 adsorption on three continuous SDBs, while the same rearranged dynamics take place again. As the distance gets larger in Fig. 4.6(c) and Fig. 4.6(e), the distance of two SDBs is already too far for I_2 dissociative adsorption. Comparing with Fig. 4.5(c), the maximum distance for I_2 adsorption on Si(100) surface at room temperature is around 5 Å. The configurations in Fig. 4.5(c)-Fig. 4.5(e) and Fig. 4.6(c)-Fig. 4.6(d) are easily found at high coverage surface. These SDBs are basically produced via abstractive adsorption and crossed type II sites. Here demonstrates the reason why an iodine saturation surface can't be approached at room temperature.

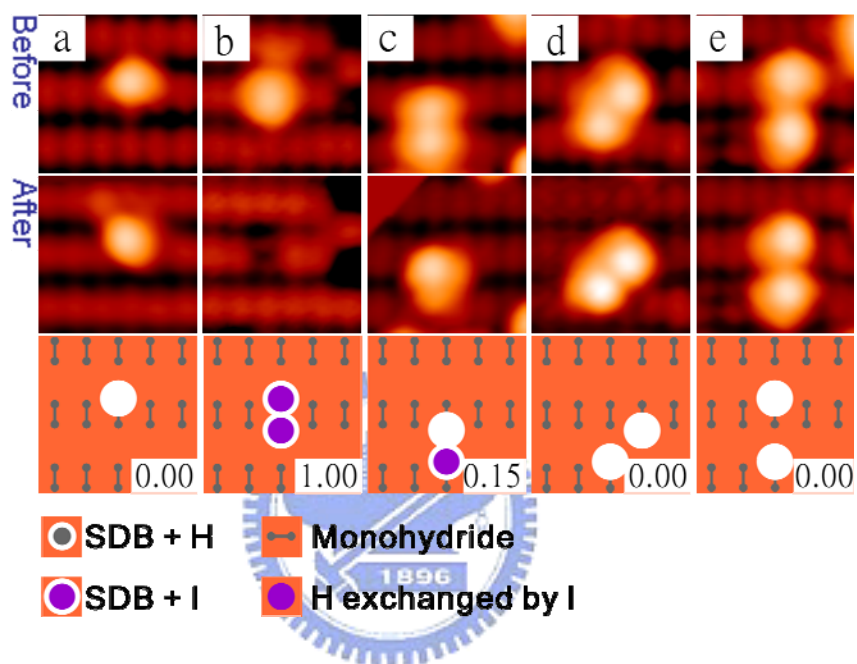


Fig. 4.5 Showing before and after 1.32 L I_2 expose on (a) single DB and (b)-(e) series of SDB pairs with different distance extended perpendicular to the dimer row direction prepared on H/Si(100) surface, relatively interaction and adsorption probabilities of each event are shown at the bottom. The STM sample bias are -1.8 V.

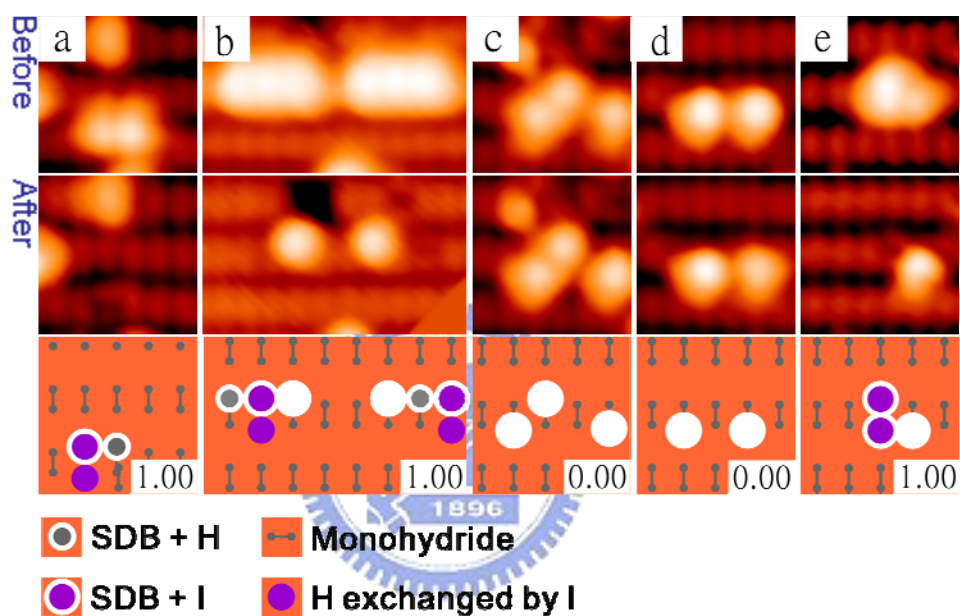


Fig. 4.6 Showing before and after 1.32 L I₂ expose on series of SDB pairs with different distance extended along the dimer row direction prepared on H/Si(100) surface, relatively interaction and adsorption probabilities of each event are shown at the bottom. The STM sample bias are -1.8 V.

4.4 Conclusion

Room temperature adsorption of I_2 on Si(100)-(2 × 1) surface has been studied by the STM. Dissociative adsorption is the dominant process. Adsorption of I_2 on the same side of neighboring dimer is favored than on one dimer with the ratio of 7:1 at low coverage. Isolated SDBs are present due to abstractive adsorption and crossed type II configurations, these isolated SDBs direct result in a maximum iodine coverage of 0.92 ML. A series studying of I_2 adsorption on isolated SDB pairs is demonstrated on H/Si(100) surface. The maximum distance of two SDBs for I_2 dissociative adsorption is $\sim 5 \text{ \AA}$.



Chapter 5 Topographically Constrained Adsorption and Reaction Mechanisms of I₂ and Cl₂ on the Si(100) Surface

5.1 Introduction

Molecule-surface reaction mechanisms are of importance and interest to chemical processes involving solids and catalysts [34,47,48]. Specifically, the reaction of halogen gases with the Si(100) surface as a prototypical case has attracted much attention [40,41,7,43,6,5]. A key question is: Do the two atoms in a halogen molecule prefer a pair adsorption process, in which the two atoms bind to two neighboring dangling bonds on the surface, as the geometry would suggest [7,49]? Or, is an abstractive process more likely, in which one halogen atom binds to a surface dangling bond, leaving behind a hot halogen atom [50]? A related question for the latter case is: What happens to the hot halogen atom? Thus far, work in this field has been mostly based on a survey of reaction results over a large area; the analysis can be complicated by competing mechanisms and multi-step processes.

To gain direct, geometry-specific information, we have performed a new experiment in which the active sites on a Si surface are pre-organized into simple configurations, including isolated dangling bonds and dangling bonds organized in pairs, clusters, and arrays. Scanning tunneling microscopy (STM) observation of the reaction of I₂ and Cl₂ with these dangling bond configurations shows interesting differences. While I₂ adsorption is primarily a pair process, the adsorption of Cl₂ is dominated by an abstractive process. Also observed are cascading surface reactions involving the hot Cl atom following the abstractive reaction, leading to many possible final states. These details become evident in our experiments because the initial dangle bond configurations place strong restrictions on the possible reaction pathways.

5.2 Experiment

In our experiment, clean Si(100)-(2 × 1) surfaces were prepared by direct Joule heating to ~1400 K. Subsequently, the chamber was backfilled with hydrogen gas to 2×10^{-7} torr; a tungsten filament at 1800 K positioned in front of the sample was used to create atomic hydrogen (H). The Si surfaces after a saturation exposure to H were mostly terminated by monohydride, where each Si dimer dangling bond of the clean starting Si surface was terminated by a H atom. Also present on the surfaces was a small admixture of dihydrides, where the original Si-Si dimer bond was broken to allow two H atoms to terminate each Si surface atom [51]. Various dangling bond configurations were formed afterwards by mild thermal desorption or programmed STM tip-induced desorption of the H [52, 53, 54]. Vapors of I₂ and Cl₂ were introduced into the chamber through a precision leak valve for the adsorption measurements.



5.3 Results and Discussion

The STM picture in Fig. 5.1(a) shows Si dimer rows terminated by hydrogen as well as eight bright features resulting from a mild thermal treatment. In the zoom-in image as Fig. 5.1(b), three of the bright features are less intense than the others and are each biased on one side of the respective dimer row. Each of these corresponds to an isolated Si dangling bond. The other five brighter features are symmetric about the respective dimer rows; they correspond to doubly desorbed dimers, or two neighboring dangling bonds in each case.

Figure Fig. 5.1(c) shows the same area after a saturation exposure of I_2 at room temperature. The five very bright features are each replaced by a pair of dim spots, which correspond to two I-terminated Si atoms in a dimer. The adsorption is therefore pair-wise. The results also demonstrate that the isolated dangling bonds are unaffected by the exposure. A survey over a large number of isolated dangling bond sites yields a mere ~2% probability for them to be terminated by I, while dimer dangling bond pairs have a 100% adsorption probability. Figure Fig. 5.1(d) is a schematic illustration of the events. The arrow on the right in Fig. 5.1(b) points to an I-terminated dimer. For comparison, the arrow on the left points to a dihydride species; the two spots are farther apart than that for the I-terminated dimers [55].

With programmed STM-tip desorption, a surface was prepared with an array of dangling bond clusters, each involving two and three neighboring pairs of dimers, or four and six dangling bonds in each cluster. Several such clusters are shown in Fig. 5.2(a). After I_2 exposure, nearly all clusters become saturated by I termination, as seen in Fig. 5.2(b). The results, summarized by a schematic diagram in Fig. 5.2(c), are fully consistent with and further corroborate the pair adsorption mechanism as the dominant process.

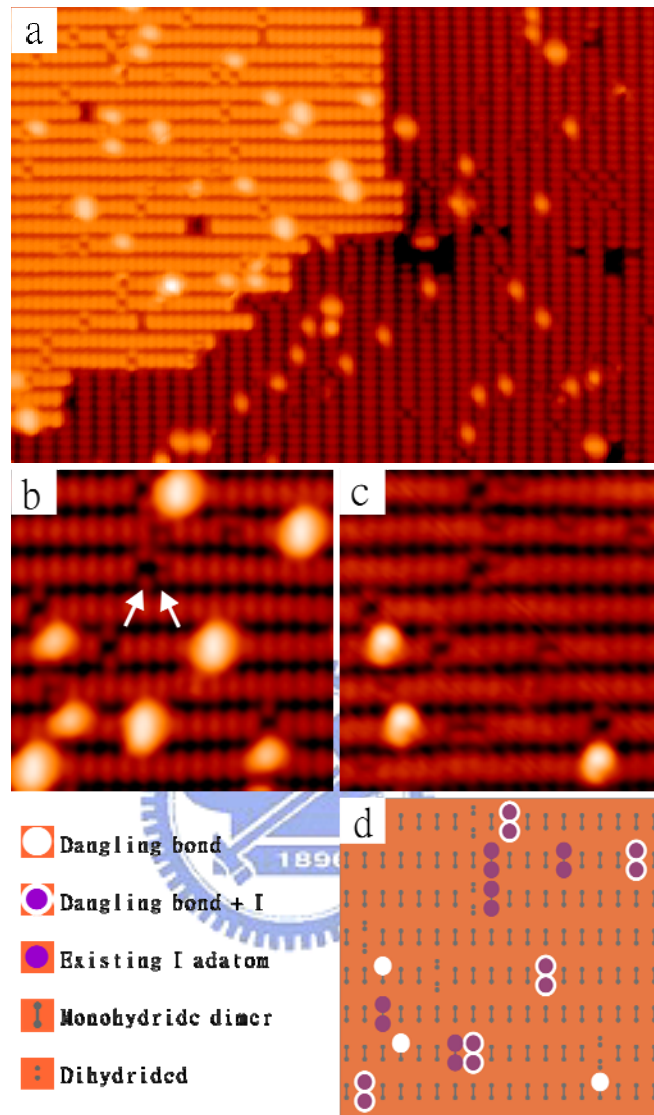


Fig. 5.1 (a) A filled state STM picture of a Si(100) surface mostly terminated by H. (b) Larger image showing five very bright features correspond to dimer dangling bond pairs, while the three somewhat less bright features correspond to single dangling bonds. The arrows point to a dihydride dimer (left) and an I-terminated dimer (right). (c) A picture showing the same area after I₂ exposure. (d) A schematic diagram illustrating the processes. The STM sample bias are (a)-(b) -2, and (c) -1.85 V.

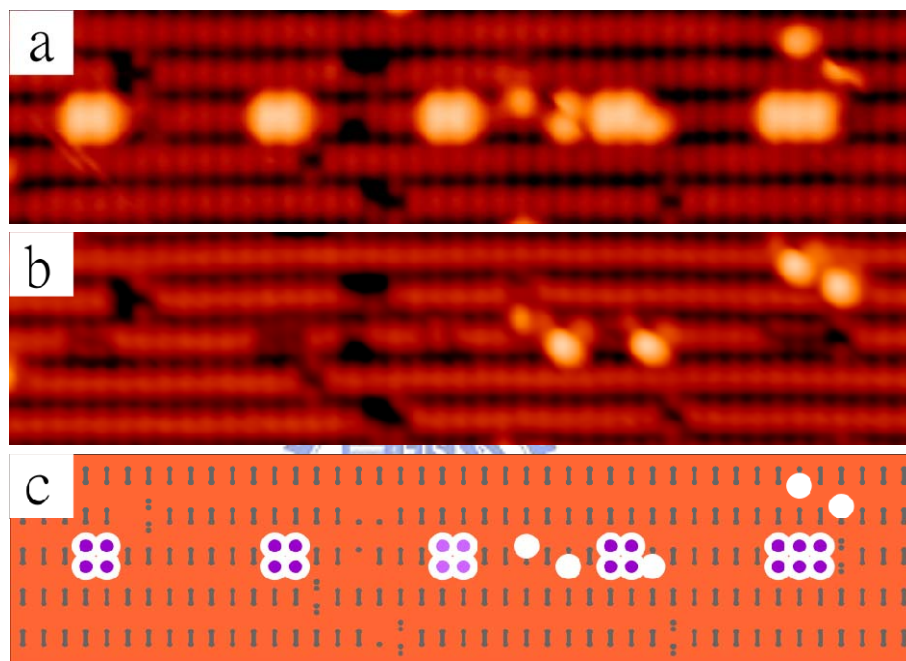


Fig. 5.2 (a) A STM picture of a Si(100) surface mostly terminated by H. Each of bright features corresponds to neighboring dimers with the H desorbed, or a cluster of dangling bonds. (b) The same area after I₂ exposure. (c) A schematic diagram for the area imaged; the symbols are the same as those used in Fig. 5.1. A little uncertainty is recorded in the center of the clusters. The STM sample bias are (a)-(b) -2, and (c) -1.85 V.

For easy distinction, the STM pictures pertaining to Cl₂ adsorption shall be shaded in green, as compared to red for I₂ adsorption. The picture in Fig. 5.3(a) corresponds to a single dangling bond on the starting surface. The six pictures in Fig. 5.3(b)-Fig. 5.3(e) and Fig. 5.3(g)-Fig. 5.3(h) are the results after exposure of a single dangling bond to Cl₂, yielding 1, 2, 2, 2, 3 and 5 Cl adatoms, respectively; the position of the dangling bond before adsorption is indicated by an arrow in each case. The two cases with 2 Cl adatoms have different final geometries. Since Cl₂ adsorption occurs readily on a single dangling bond, it must be an abstractive reaction. The hot Cl atom left over from the reaction must be responsible for the additional Cl adatoms in nearby areas. An analysis of a large number of cases involving just two Cl adatoms in the final state yields the statistics shown in Fig. 5.3(f) for each nearby site to be occupied by the second Cl atom. It is interesting to note that the site neighboring the original dangling bond on the same dimer unit is avoided, and the average distance from the original dangling bond is fairly short.

The very different adsorption processes for Cl₂ and I₂ suggest different reaction energetics and kinetics. The relevant bond energies are: 2.4 eV for Cl₂, 3.8 eV for Si-Cl, 3.2 eV for Si-H, and 4.3 eV for H-Cl [35]. A Cl₂ molecule impinging upon an isolated Si dangling bond can dissociate, based on energy considerations (2.4 eV << 3.8 eV), resulting in a Cl atom bonded to the Si. The remaining hot Cl atom can desorb into vacuum. Or, it may find a nearby H atom on the surface, bind with it, and desorb as a HCl molecule; this is again an energetically favorable process (4.3 eV >> 3.2 eV).

Thus, the results after the abstractive reaction of Cl₂ at an isolated dangling bond can be either Cl-termination alone or Cl-termination plus a nearby newly created Si dangling bond. The latter can react with another incoming Cl₂ molecule, and the process can cascade for a few iterations, resulting in multiple Cl adatoms in the nearby area, as observed experimentally. The probabilities are 55% for simple Cl-termination, 28% for an additional Cl adatom, and 17% for two or more additional Cl adatoms.

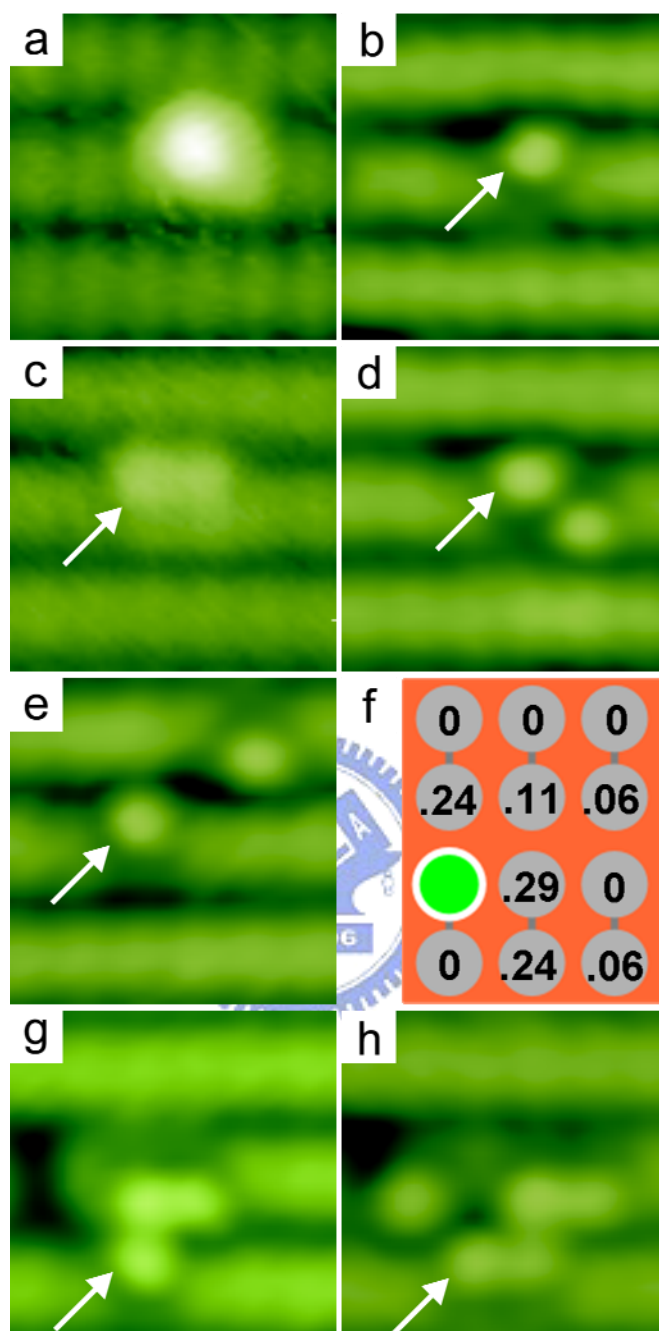


Fig. 5.3 (a) A single dangling bond. (b)-(e) and (g)-(h) Results of exposure to Cl_2 of a single dangling bond, showing 1, 2, 2, 2, 3 and 5 Cl adatoms, respectively. The arrow points to the original dangling bond position in each case. (f) Position distribution for the second Cl atom in a 2-Cl atom adsorption event relative to the initial single dangling bond position, indicated by a filled green circle. The STM sample bias are -1.7 to -1.85 V.

For I₂ adsorption, the relevant bond energies are: 1.5 eV for I₂, 2.3 eV for Si-I, 3.2 eV for Si-H, and 3.1 eV for H-I [35]. While it is energetically permissible for I₂ to dissociate and bond to a single Si dangling bond, the energy difference is much less than that for the corresponding Cl₂ case. This may suggest a reduced reaction probability, as observed experimentally, but the activation barrier can also be different. Furthermore, a hot I atom cannot bind to a nearby H and desorb as a HI molecule based on energy considerations (3.1 eV < 3.2 eV). Thus, no cascading reactions are expected. We have not observed any case where additional I atoms are adsorbed near either a single dangling bond or a cluster of dangling bonds.

The energetics for an I₂ molecule to undergo pair adsorption is strongly favorable ($2 \times 2.3 \text{ eV} \gg 1.5 \text{ eV}$), and this is the dominant process observed. The same should work for Cl₂. Yet in most cases studied, adsorption on a dimer dangling bond pair results in more complicated geometries, often involving more than two adsorbed Cl atoms. A collection of examples for Cl₂ adsorption involving various dangling bond configurations is presented in followed images.

Fig. 5.4(a) shows an initial surface with three dangle bond pairs. A picture of the same area after Cl₂ exposure, Fig. 5.4(b), reveals two or four Cl adatoms for each initial dangling bond pair. Other pictures, not included here, present evidence for three, five, or more Cl adatoms. A comparison of Fig. 5.4(c) and Fig. 5.4(d), before and after Cl₂ adsorption, shows that an isolated dangling bond and a cluster of four dangling bonds lead to a complicated final configuration with eight total adsorbed Cl atoms. Fig. 5.4(e) and Fig. 5.4(f) show similar experiment and result on some clusters of dangle bonds. The before and after pictures in Fig. 5.5(a) and Fig. 5.5(b) show that a linear array of dimer dangling bonds become a more diffuse array of Cl adatoms. The same theme is further illustrated in Fig. 5.6(a) and Fig. 5.6(b), which involve an initial stripe of dangling bonds. In all of the cases examined, no dangling bonds are left after the adsorption, but in some instances, there is evidence for H migration onto nearby dangling bonds during these more involved processes. The final number of Cl adatoms is generally greater than the original number of dangling bonds, except for a few simple cases where the numbers are

equal. These results are consistent with the abstractive reaction being the dominant adsorption process.

Abstractive adsorption on surfaces is an established concept with clearly demonstrated evidence [50,37]. However, the detailed atomic processes are generally not well known. One issue of interest is the relative importance of other competing processes, such as dissociative adsorption. Another issue is the fate of the remaining hot atom (or fragment) after an abstractive reaction. Our work shows that following an abstractive adsorption of Cl_2 , the hot Cl atom can either leave the surface or travel on the surface for a distance before initiating another surface reaction, possibly leading to additional secondary reactions. These detailed atomic processes are made clear by in situ studies involving various initial active site configurations. This approach points to opportunities for systematic investigations of the atomistics of gas-surface reactions.



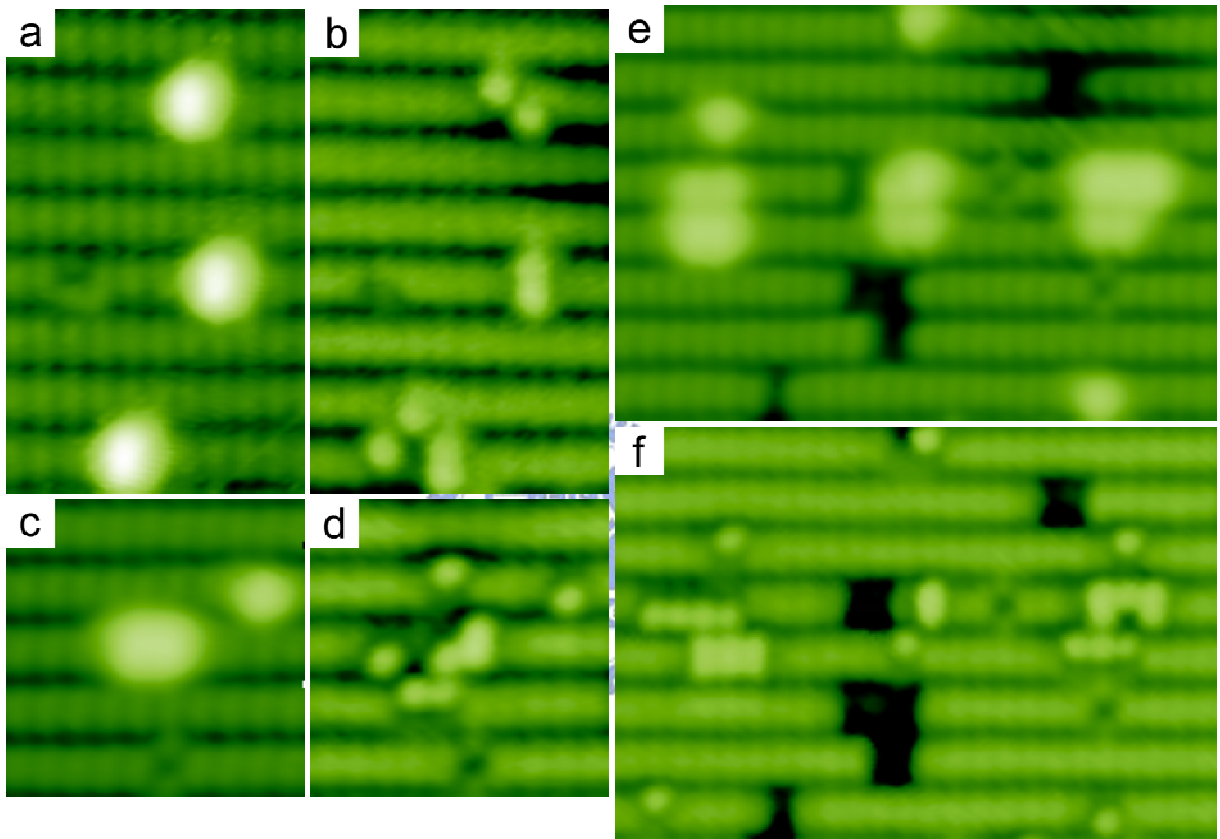


Fig. 5.4 (a) Three dangling bond pairs. (b) The same area after Cl_2 exposure. (c) A single dangling bond and a cluster of four neighboring dangling bonds. (d) The same area after Cl_2 exposure. (e) Several dangling bond clusters. (f) The same area after Cl_2 exposure. The STM sample bias are -1.7 to -2.0 V.

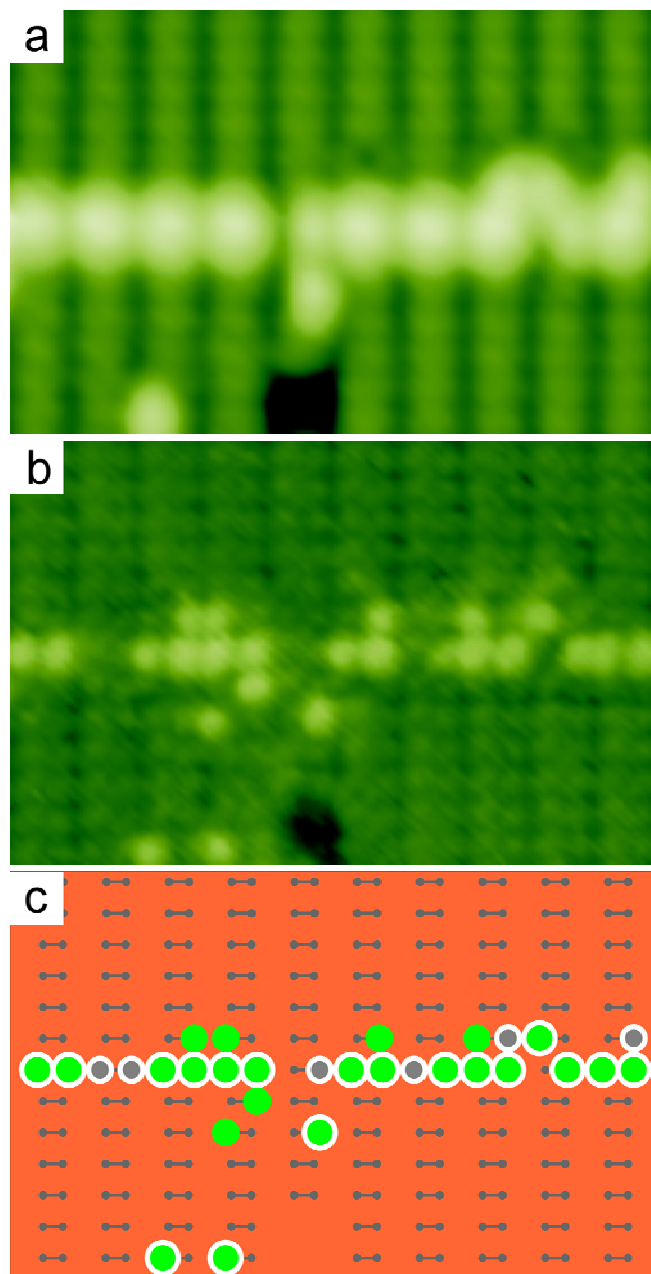


Fig. 5.5 (a) A linear array of dimer dangling bond pairs. (b) The same area after Cl₂ exposure. (c) A schematic diagram for the area imaged; the symbols are the same as those used in Fig. 5.1. The STM sample bias are (a) -1.8 and (b) 1.8 V.

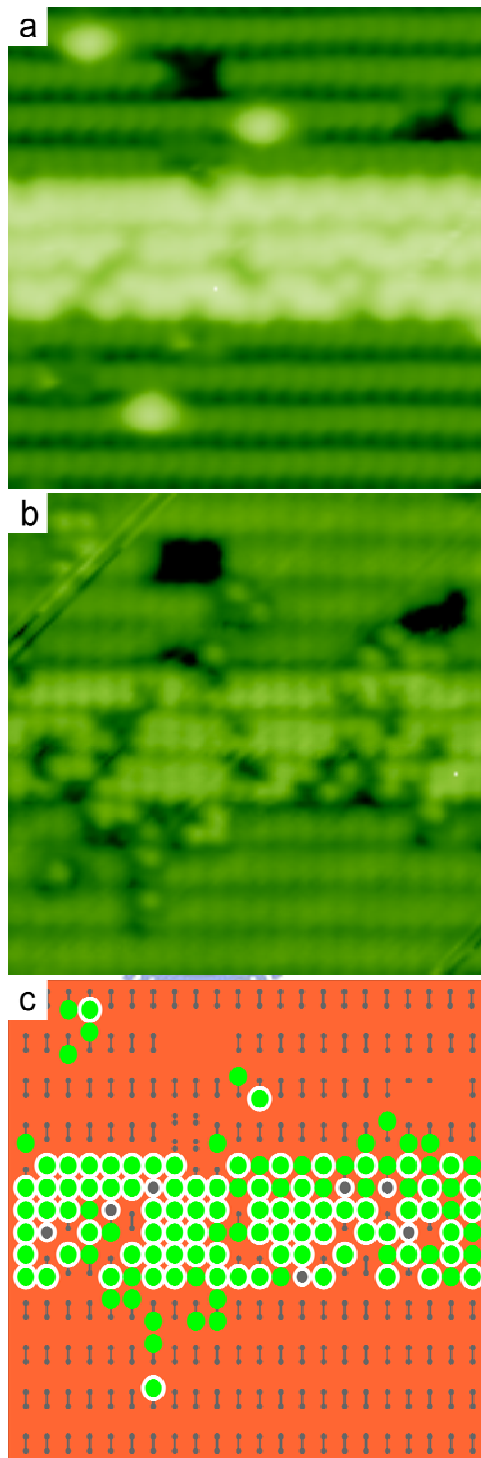


Fig. 5.6 (a) A stripe of dangling bonds. (b) The same area after Cl₂ exposure. (c) A schematic diagram for the area imaged; the symbols are the same as those used in Fig. 5.1.

5.4 Conclusion

H-passivated Si(100)-(2x1) surfaces were prepared with selected surface bonds reactivated by desorption of the H, resulting in dangling bonds in isolation or organized in pairs, clusters, or arrays. Reaction of these dangling bond configurations with Cl₂ and I₂ was examined with scanning tunneling microscopy. While I₂ adsorption is predominantly a pair process involving the bonding of the two I atoms to two neighboring dangling bonds, the adsorption of Cl₂ is dominated by the bonding of just one Cl atom, with the other Cl atom either leaving the surface or migrating to a nearby area to cause further reactions.



Chapter 6 Conclusion

In this thesis, the dynamics of diatomic molecular on Si(100)-(2 × 1) surface was discussed using scanning tunneling microscope (STM). The surface reactions included adsorption, diffusion, desorption, and phase transition. With the ability of real-space image and atomic resolution, we could in situ study these detailed atomic processes. The recombinative desorption were performed by H₂ from monohydride and dihydride species. The surface structure rearrangement was also observed during hydrogen reduction. Adsorption mechanism of Cl₂ and I₂ were demonstrated on clean Si(100)-(2 × 1) surface and hydrogen terminated surface. Due to different exothermicity after chemical bonding on the surface, Cl₂ and I₂ have different adsorption mechanism. I₂ adsorption is primarily a pair process, the adsorption of Cl₂ is dominated by an abstractive process.

We have presented a detailed atomistic view of the desorption of H₂ from H/Si(100) surface. The results illustrate two basic principles relevant to recombinative desorption: the constituent atoms must be organized first on the surface into predesorption states that are compatible with the free molecular geometry, and the resulting surface structure must be energetically favorable.

Our conclusions are summarized in the following:

1. Desorption from dihydrides proceeds by recombination of two H atoms coming separately from two adjacent dihydrides, leaving behind after the reaction a monohydride dimer on the surface.
2. Desorption from the (3 × 1) surface via dihydrides species is geometrically forbidden, but becomes possible with a switch of a dihydride with a neighboring monohydride dimer to form two adjacent dihydrides.
3. Desorption from monohydrides occurs at a higher temperature, and proceeds by

recombination of the two H atoms on a given monohydride dimer.

4. Up to ~4% more vacancies could be found after annealing at 570 K. These etching processes could account for some reduction of surface hydrogen during the (3×1) to (2×1) phase transformation.
5. Dihydride-pair recombination mechanism is the dominant process during phase transition. So, both the initial (3×1) and (1×1) domains linearly decay with a common half-life time of ~9.8 h.

Room temperature adsorption of I_2 on Si(100)- (2×1) surface had been studied. The result showed the dissociative adsorption is the dominant process. With dissociative mechanism as a dominant process for adsorption, I_2 could not terminate Si(100) surface.

Our conclusions are summarized in the following:

1. Adsorption of I_2 on the same side of neighboring dimer is favored than on one dimer with the ratio of 7:1 at low coverage.
2. Isolated SDBs are present due to abstractive adsorption and crossed type II configurations.
3. Due to I_2 adsorption is primarily a pair process, the presence of isolated SDBs direct result in a maximum iodine coverage of 0.92 ML.
4. A series studying of I_2 adsorption on isolated SDB pairs is demonstrated on H/Si(100) surface. The maximum distance of two SDBs for I_2 dissociative adsorption is ~5 Å.

The mechanism of diatomic molecules onto the surface is divided into two categories: dissociative adsorption and abstractive adsorption. To studying these surface reaction, we chose Cl_2 and I_2 for the reason of high and low exothermicity after chemical bonding on the Si surfac. H-passivated Si(100)-(2 × 1) surfaces were prepared with selected surface bonds reactivated by desorption of the H, resulting in dangling bonds in isolation or organized in pairs, clusters, or arrays. Reaction of these dangling bond configurations with Cl_2 and I_2 was examined with scanning tunneling microscopy.

Our conclusions are summarized in the following:

1. I_2 adsorption is predominantly a pair process involving the bonding of the two I atoms to two neighboring dangling bonds,
2. Adsorption of Cl_2 is dominated by the bonding of just one Cl atom, with the other Cl atom either leaving the surface or migrating to a nearby area to cause further reactions.



Appendix A Growth Behaviour of Ge Nano-islands on The Nanosized Si{111} Facets Bordering on Two {100} Planes

A.1 Introduction

The strain-driven self-organized growth of the threedimensional quantum-dot (QD) nanostructure in semiconductor heteroepitaxy has attracted considerable attention [56]. The quantized energy levels in the QDs can be manipulated through controlling their sizes and shapes, producing numerous promising nanoelectronics and optoelectronic devices [57]. In the growth processes and control, Ge-rich nano-island formation on the low-index silicon surfaces represents an ideal system for more thoroughly understanding the nature and the mechanism of the size distribution, evolution, and shape transformation of the QDs. Nanoscale-sized surfaces in the form of mesas or ridges on patterned substrates offer opportunities not only for novel growth-control engineering, but also for gaining a fundamental understanding of the phenomena of size-dependent crystal growth during the formation of QDs.

Nanosized surfaces are confined by boundaries such as growth-resistant thin films, nearly-vertical side walls milled by reactive ion etching (RIE), and well-defined low-index crystalline facets. Shiraki et al studied the size effect by depositing Ge on oxidized Si(100) windows with diameters ranging from 90 to 650 nm [58]. Their experimental results demonstrated that Ge size and numbers of Ge nanoislands increase with the window diameter. Similar experiments were performed on the patterned Si(100) square and circular mesas with size ranging from 90 to 580 nm and the sizes

and numbers of the Ge nano-islands were found to increase monotonically with the mesa size [58,59]. Additionally, the nano-islands were found to nucleate preferentially at the mesa edges and corners obtained using RIE [60,61]; Yang et al attributed their observation to the lower chemical potential in these regions resulting from the spatially nonuniform relaxation of the strained wetting layer [60]. Moreover, Jin et al showed similar preferential nucleation at the mesa edges and also that no nano-islands grow on the (113) mesa side walls [62].

As mentioned above, studies of the Ge nano-island growth on the windows or mesas have largely focused on the (100) plane of silicon. Few works have discussed the growth of nano-islands on the nanosized {111} plane. Using tetramethyl ammonium hydroxide (TMAH) solution to fabricate V-groove patterns in the Si(100) substrate with large {111} side walls, Suda et al observed that deposited Ge adatoms migrate from the surrounding (100) surface to the bottom of the V-groove or pits and form nano-islands at growth temperatures exceeding 750 K [63]. Olzierski et al used TMAH to build nanometer-scale V-grooves with {111} walls on oxidized Si(100) substrate [64]. Their results show that the Ge islands do not grow on the flat {111} facets, but rather nucleate at the bottom of the V-grooves.

This study reports the growth of nano-islands on nanoscale {111} surfaces created via KOH anisotropy etching. The nanoscale surface areas are surrounded by well-defined (100) or {111} planes. The nano-island formation on the small surface areas was found to be strongly dependent on the area geometry. The effect of area geometry was attributed to the adatom flux in or out of the small surface areas into the surrounding plane.

A.2 Experiment

Fig. A.1 illustrates the sample process flow used in the experiment. First, the four-inch n-type Si(100) wafers were RCA cleaned and thermally oxidized to form approximately 100 nm thick SiO₂ films. Using conventional optical photolithography and buffered oxide etch (BOE) solution etching, various rectangular-shaped Si windows with their edges oriented along the [110] direction were then opened. The {111} facets were obtained by etching in stirred 20% KOH + isopropyl alcohol (IPA) (5:1) solution at room temperature for various periods to achieve the desired width [65]. This strong-base solution preferentially etches the {100} and {110} planes, relative to {111}, in single-crystal silicon, thus creating an anisotropic etch. The etching rate along the (100) plane is $\sim 15 \text{ nm min}^{-1}$. Following KOH etching, the SiO₂ masks were removed by BOE etching.

Before patterned Si wafers were loaded into the growth chamber, the substrates were chemically cleaned and dipped into a diluted HF solution to produce a hydrogen-terminated surface. Ge growth was performed via ultra-high vacuum chemical vapour deposition (UHV-CVD) at a growth temperature of 650°C with a GeH₄ flow rate of 5 sccm. Under the present study conditions, the growth rate is about 2.3 nm min^{-1} on the (100) surface. The samples investigated in this study had a growth time of 100 s, and thus, an average Ge thickness of 3.5 nm. Following growth, the surface topography of the samples and three-dimensional (3D) islands were examined using a commercial atomic force microscope (AFM) operated in tapping mode in air.

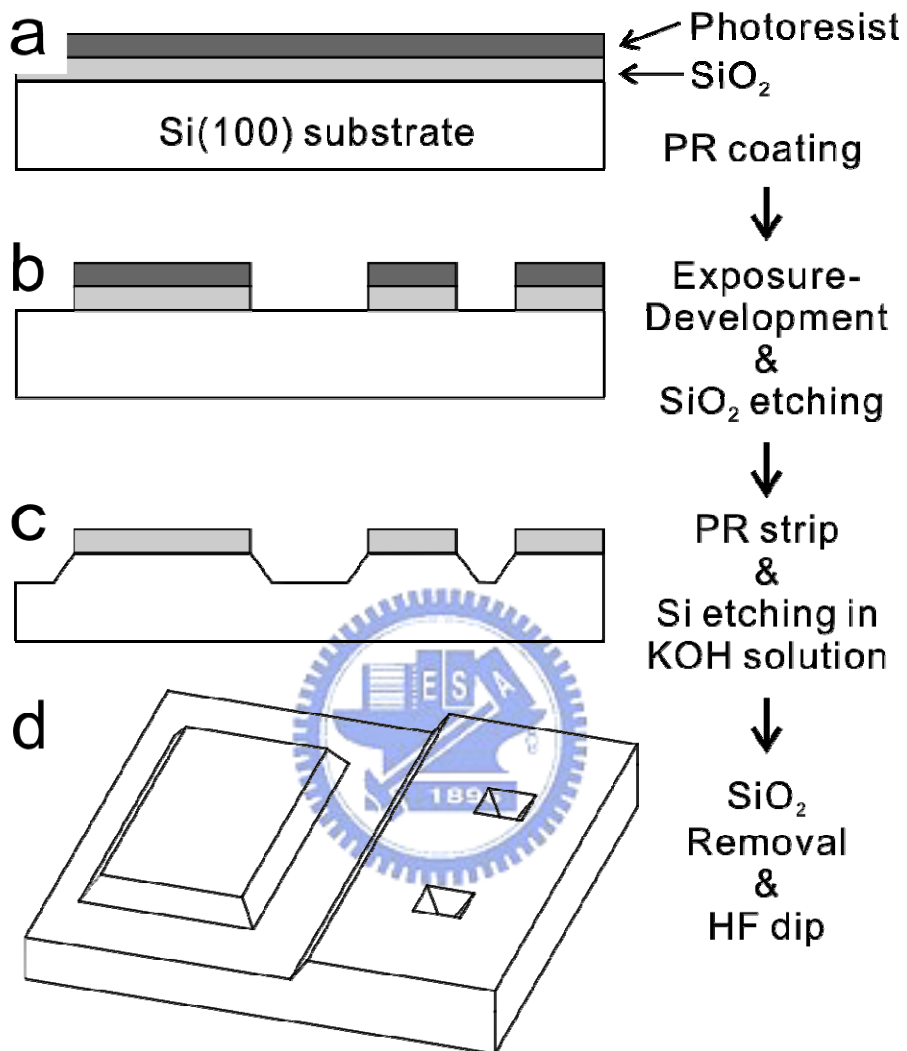


Fig. A.1 Process flow chart for the fabrication of 2D arrays of rectangular mesas and negative pyramids.

A.3 Results and Discussion

A.3.1 The formation of well-confined {111} surface

As described in section 2, the flat nanosized Si{111} facets confined by the Si(100) zones were obtained through anisotropic wet chemical etch. The etching time regulates the etching depth and thereby the width of the {111} facets (W_{111}). Fig. A.2 shows the typical AFM line profiles for various etching depths from 9 to 150 nm. Based on the basic geometrical analysis of the diamond structure, the angles between the (114), (113), and (111) planes and the (100) plane are 19.5° , 25.3° , and 54.7° , respectively. The evolution of the topographic profiles and overall angles in Fig. A.2 indicates that the (113) and (114) planes are not evident under the wet etching and that the {111} facets become well-defined as the etching depth exceeds ~ 30 nm. The bottom boundary of the {111} facets is concave and Fig. A.2 demonstrates that the {111} and (100) facets meet with a sharp angle. In contrast, the top boundary is convex, and the cusp between the {111} and (100) facets is blunt, possibly because of the undercut etch and the balance of the strain relaxation and chemical bonding energy [60].

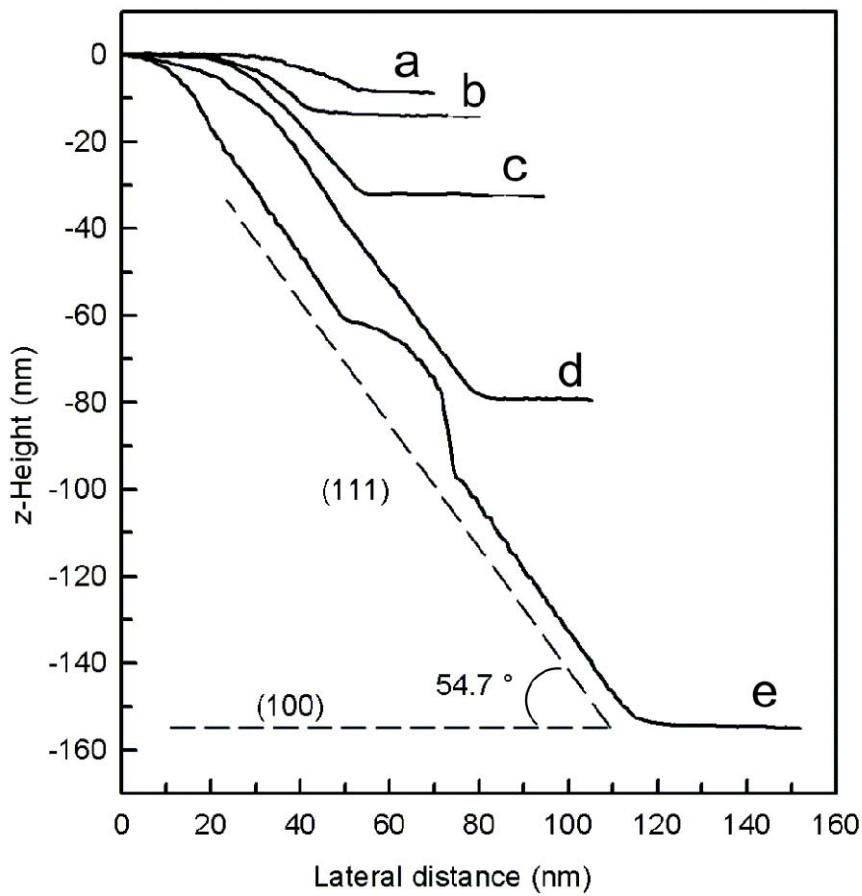


Fig. A.2 AFM z-height profiles over the mesa side walls following etching in KOH + IPA solution. The etching depth is about (a) 9, (b) 15, (c) 32, (d) 80, and (e) 150 nm. The two dashed lines provide guides to the (100) and {111} planes. The profiles reveal that the {111} facets become well defined as the etching depth exceeds 30 nm. The bump near the centre of (e) was created by scanning over a grown nano-island.

A.3.2 Ge nano-islands on the (100) planes

Fig. A.3 displays the derivative AFM images taken after Ge UHV-CVD growth on the patterned Si(100) samples with various KOH etch time. A mesa is clearly visible near the centre of each image; the photolithographic mask used in patterning the mesas has an area of $3 \times 6 \mu\text{m}^2$. With increasing etch depth, the side walls of the Si(100) mesas expand at the expense of the mesa area. Depending on the relative etching rates of the solution [66], as Fig. A.3 illustrates, the side walls of the etched mesas comprise various crystallographic planes other than the $\{111\}$ facets discussed in this study.

A 3D island forms a stable nucleus owing to the roughening transition from the stained wetting layer; this is a Stranski–Krastanov growth process. The critical thickness before island formation for Ge growth on Si(100) is known to be around 3 ML for the large (100) areas. Once the critical thickness is exceeded, islands grow in a random manner. Most nano-islands are dome clusters with an average radius of 30 nm, average height of 15.2 nm, and island number density (N_{100}) of $5 \times 10^9 \text{ cm}^{-2}$. Compared with a previous study [67], the island number density obtained in this approach is higher and the average size of nano-islands is smaller due to the smaller diffusion length of the Ge adatoms during the higher rate and low-temperature deposition in this work [68]. The island density on the (100) facets appears to be constant throughout their areas in Fig. A.3.

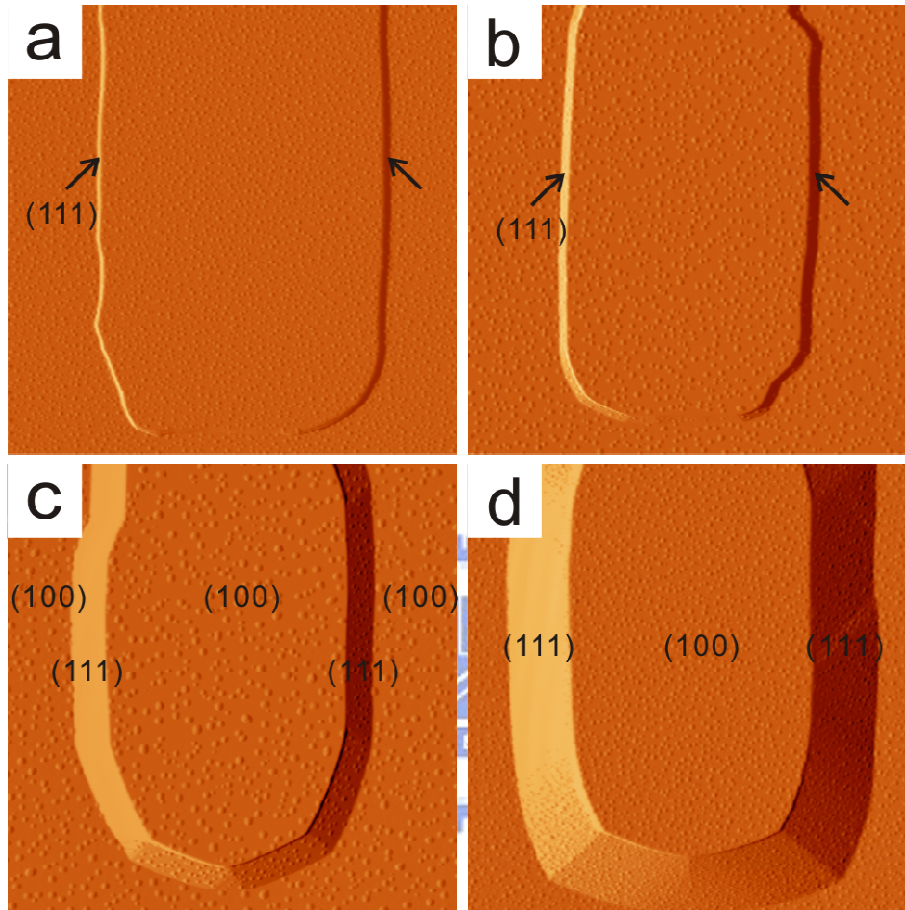


Fig. A.3 Derivative AFM images displaying Si mesas after Ge growth. The arrows indicate the $\{111\}$ planes. The width of the $\{111\}$ facets is about (a) 100, (b) 180, (c) 530, and (d) 1190 nm. Most nano-islands are dome clusters with an average radius of 30 nm and average height of 15.2 nm on the (100) plane. The image sizes are $5.5 \times 5.5 \mu\text{m}^2$.

A.3.2 Ge nano-islands on the {111} planes

In Fig. A.3, the {111} facets fence the left and right sides of the (100) mesas appearing as the bright and dark bands in the image because of the derivative imaging processing. Three dimensional images Fig. A.4 and derivative images Fig. Fig. A.5 displays typical zoom-in images over these {111} side walls. The {111} facets have width (W_{111}) of around 100, 180, 530, and 1190 nm for Fig. A.4(a)-Fig. A.4(d) and Fig. A.5(a)-Fig. A.5(d), respectively. These islands ripen during growth, broadening the volume distribution. Presumably these islands consist of the SiGe alloy [69,70]. Similar to the (100) surface areas, nano-islands appear on the {111} facets once Ge coverage exceeds $\sim 3\text{--}5$ ML [70,71,72]. The average Ge thickness of about 15 ML is much larger than those of the wetting layers; therefore, the slight difference in the wetting layer thickness does not affect the nucleation behaviour observed herein.

On the large {111} facets such as in Fig. A.5 (c) and Fig. A.5(d), the nano-islands have a smaller average size and a higher number density (N_{111}) compared to those (N_{100}) on their neighbouring (100) facets. The equivalent thickness of the Ge growth obtained by integrating island volume per unit area is roughly the same for both the large {111} and (100) areas. Neglecting the difference in the critical thickness of their wetting layers, the Ge concentration of the wetting layers and islands, the effect of the finite radius of the AFM tip on the island sizemeasurement, and the scanning geometry difference on the two surfaces, this study estimated the deposition rates of Ge on the two facets to be roughly equal, while a similar study showed that the growth rate in {111} is about half of that in (100) [69]. Within the limitations of the AFM resolution, the nano-islands do not show facets as those observed in the molecular beam epitaxy at low rate [73]. This study estimates that N_{111} is $\sim 4N_{100}$. The crystallographic orientations of the two facets in the growth chamber might affect their growth rates slightly, but not their growth

morphology under similar growth conditions. The island number density N is roughly proportional to $D^{-1/3}$ at the same deposition rate, where D denotes the diffusion coefficient [74]. The higher island density indicates a smaller diffusion coefficient, that is, $D_{111} \sim D_{100}/60$ on the wetted layers of the two facets.



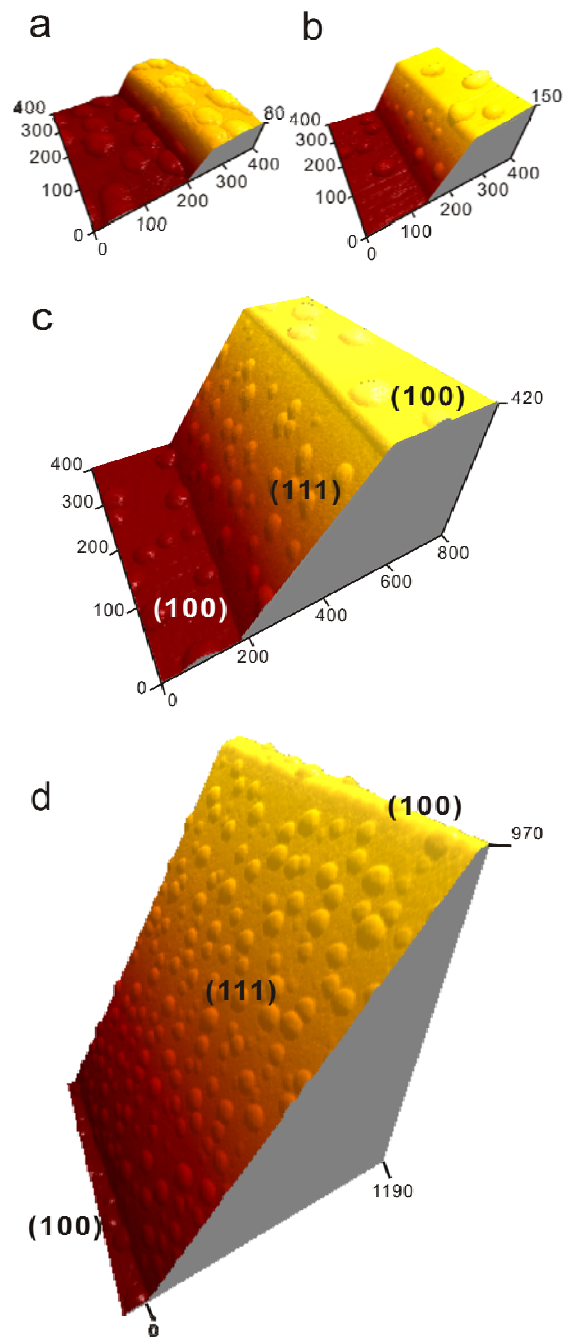


Fig. A.4 Zoom-in three-dimensional images over the $\{111\}$ facet for the same samples, namely (a) Fig. A.3(a), (b) Fig. A.3(b), (c) Fig. A.3(c), and (d) Fig. A.3(d).

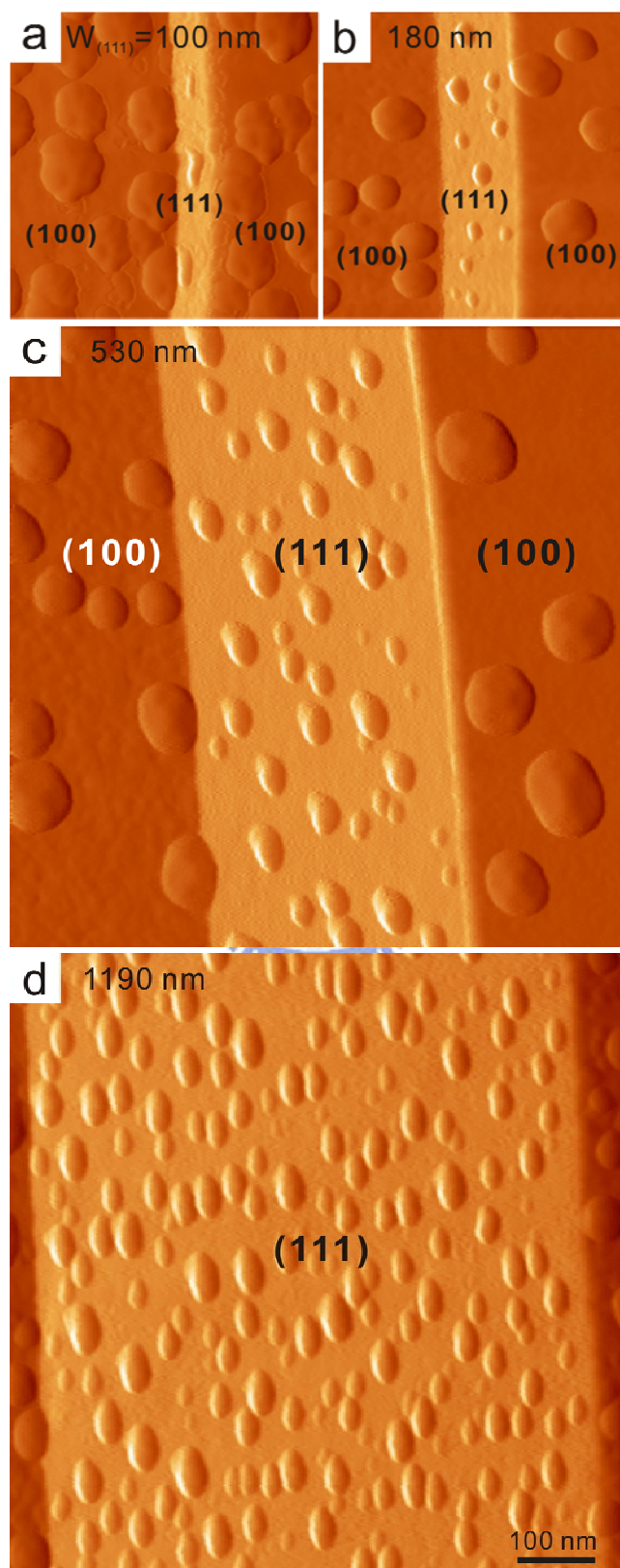


Fig. A.5 Zoom-in derivative images over the $\{111\}$ facet for the same samples, namely (a) Fig. A.3(a), (b) Fig. A.3(b), (c) Fig. A.3(c), and (d) Fig. A.3(d).

Compared to the central area in Fig. A.5(c) and Fig. A.5(d), N_{111} near the border of the (100) facets is noticeably smaller. In fact, nearly nuclei-free bands (known as the denuded zone) are clearly observable on both edges of the $\{111\}$ facets in Fig. A.5(c); their width (W_{dz}) is of the order of a few tens of nanometres. When W_{111} is compatible with W_{dz} , both the island density N_{111} and the average sizes of the nano-islands on the $\{111\}$ facets decrease significantly, as shown in Fig. A.5(a) and Fig. A.5(b). In contrast, N_{100} displays little variation between the situations where it is near to and distant from the edges. As shown in Fig. A.6, similar island depletion zones on the $\{111\}$ planes are also evident in the negative pyramid structure created on a square silicon oxide window on the same substrate as that in Fig. A.3(c).

The reduction in the island density and size on the $\{111\}$ facets near their border with the (100) facets implies the loss of Ge adatoms on the $\{111\}$ facets either to a good sink of adatoms at the boundary of the two facets or to the neighbouring (100) facet. Fig. A.3 and their zoom-in images show that the (100) facet near the convex boundary contains nano-islands; however, few nucleated islands are visible above the convex boundary. Restated, preferential nucleation of nano-islands on the (100) facet near the $\{111\}$ boundaries is not as evident as near the (100), (110) and a curved surface [75,60]. The convex edges between the $\{111\}$ and (100) facets are not good sinks for Ge adatoms. Nevertheless, near the concave boundary (or the L-shape groove), however, preferential nucleation is slightly enhanced on the (100) plane, as shown in Fig. A.5(c). The base areas of these nano-islands are on the (100) plane, indicating that they nucleate on the (100) plane and grow to contact with the V-groove. In comparison, Ge nano-islands preferentially grow on top of the V-grooves between two $\{111\}$ family planes (Fig. A.6) [69,63,64].

As noted by Yang et al, the (100) facet near the concave edge has a low chemical potential owing to the spatially nonuniform relaxation of the strained wetting layer, and

can act as a local nucleation centre. The preferred nucleation can account in part for the depletion of Ge adatoms around the nearby $\{111\}$ facets, assuming that the V-groove does not impose significant diffusion barrier. Additionally, the existence of the adatom sink on the V-groove and in the pits can lead to island depletion on the (100) surface [63]. However, a separate driving force is required for depleting Ge adatoms on the $\{111\}$ facet near its convex edge, a location that lacks a good sink nearby. With no other driving forces, mass transport is driven by chemical-potential gradients associated with the wetting layer thickness [76], that is, $F = -\frac{\Delta\mu}{\Delta x}$. In addition, the diffusivity on the $\{111\}$ facet is smaller than that on (100), as discussed earlier. It can be concluded that a net flux of Ge adatoms from the $\{111\}$ regions toward the (100) facets indicates that the effective chemical potential μ_{100} is smaller than μ_{111} .



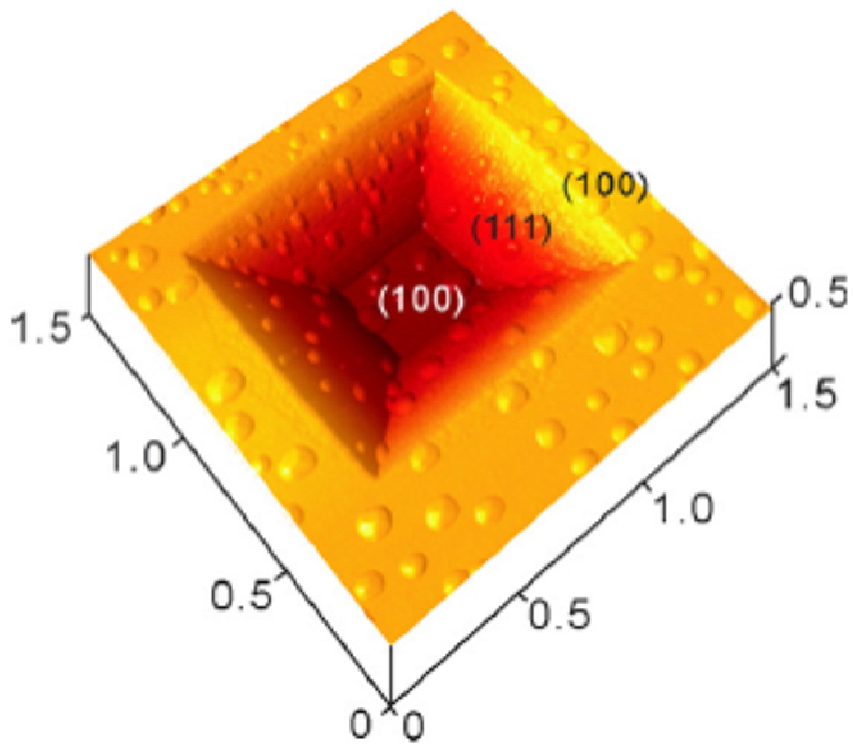
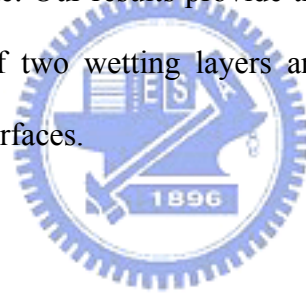


Fig. A.6 Three-dimensional AFM images showing a negative pyramid following Ge growth. The depletion zone is discernible on the edge of $\{111\}$ facets near the (100) planes, but no such zone emerges on the border between the $\{111\}$ facets. The scales are in units of micrometre.

A3.4 Conclusion

Nanosized surfaces with well-defined sidewall facets provide opportunities for both new methods of growth-control engineering, and also fundamental understanding of the size-dependent crystal growth phenomena during nano-island formation. Various nanosized Si{111} facets bordered by (100) planes were fabricated and Ge nano-islands were simultaneously grown on the two facets. Nano-island formation was suppressed on the {111} facets as the width of the {111} facets reduced below ~500 nm at growth temperature 650°C. By excluding Ge adatom sinks near the convex border of the two facets, we conclude that the effective chemical potential for Ge adatoms on the {111} facets is smaller than that on the (100) facet, resulting in an adatom flux from the {111} facets to the (100) plane. Our results provide the first direct comparison of the adatom chemical potential of two wetting layers and its influence on the growth behaviour on the nanosized surfaces.



References

-
- [1] T. C. Shen, Surf. Sci. 390, 35 (1997).
- [2] C. Thirstrup, Surf. Sci. 411, 203 (1998)
- [3] T. C. Shen, J. A. Steckel, and K. D. Jordan, Surf. Sci. 446, 211 (2000).
- [4] C. C. Cheng and J. T. Yates, Jr., Phys. Rev. B 43, 4041 (1991).
- [5] H. Okada, K. Inagaki, H. Goto, K. Endo, K. Hirose, and Y. Mori, Surf. Sci. 515, 287 (2002).
- [6] Z. F. Liu and S. P. Chan, Chem. Phys. Lett. 318, 15 (2000).
- [7] I. Lyubinetzky, Z. Dohnálek, W. J. Choyke, and J. T. Yates Jr., Phys. Rev. B 58, 7950 (1998).
- [8] J. A. Kubby, and J. J. Boland, Surface Science Reports, 26, 61 (1996)
- [9] X. Tong and R. A. Wolkow, Surf. Sci. 600, L199 (2006).
- [10] T. Hallam, T. C. G. Reusch, L. Oberbeck, N. J. Curson, and M. Y. Simmons, J. Appl. Phys. 68, 2187 (1990)
- [11] A. Gross, M. Bockstedte, and M. Scheffler, Phys. Rev. Lett. 79, 701 (1997); E. Pehlke and M. Scheffler, *ibid.* 74, 952 (1995).
- [12] Dynamics of Gas-Surface Interactions, edited by C. T. Rettner and M. N. R. Ashfold (The Royal Society of Chemistry, Cambridge, 1991).
- [13] S. Ciraci and I. P. Batra, Surf. Sci. 178, 80 (1986).
- [14] S. F. Shane, K.W. Kolasinski, and R. N. Zare, J. Chem. Phys. 97, 1520 (1992)
- [15] J. J. Boland, Adv. Phys. 42, 129 (1993), and references therein.
- [16] See, for example, H. N. Waltenburg and J. T. Yates, Jr., Chem. Rev. 95, 1589 (1995), and references therein.
- [17] M. Dürr, Z. Hu, A. Biedermann, U. Höfer, and T. F. Heinz, Phys. Rev. Lett. 88, 046104 (2002).
- [18] J. J. Boland, Phys. Rev. B 44, 1383 (1991).
- [19] J. J. Boland, Phys. Rev. Lett. 65, 3325 (1990).
- [20] D. T. Jiang, G.W. Anderson, K. Griffiths, T. K. Sham, and P. R. Norton, Phys. Rev. B 48, R4952 (1993).
- [21] X. R. Qin and P. R. Norton, Phys. Rev. B 53, 11100 (1996).
- [22] J.Y. Maeng, S. Kim, S. K. Jo, W. P. Fitts, and J. M. White, Appl. Phys. Lett. 79, 36 (2001).

-
- [23] J. E. Northrup, Phys. Rev. B 44, R1419 (1991).
- [24] Y. J. Chabal and K. Raghavachari, Phys. Rev. Lett. 54, 1055 (1985).
- [25] P. Nachtigall, K. D. Jordan, and C. Sosa, J. Chem. Phys. 101, 8073 (1994).
- [26] M. C. Flowers, N. B. H. Jonathan, Y. Liu, and A. Morris, J. Chem. Phys. 99, 7038 (1993).
- [27] A. Vittadini and A. Selloni, Chem. Phys. Lett. 235, 334 (1995).
- [28] M. R. Radeke and E. A. Carter, Phys. Rev. B 54, 11803 (1996).
- [29] S. K. Jo, B. Gong, G. Hess, J. M. White, and J. G. Ekerdt, Surf. Sci. Lett. 394, 162 (1997).
- [30] A. R. Laracuenta and L. J. Whitman, Surf. Sci. 545, 70 (2003).
- [31] S. M. Gates, R. R. Kunz, and C. M. Greenlief, Surf. Sci. 207, 364 (1989).
- [32] J. J. Boland, Phys. Rev. Lett. 67, 1539 (1991).
- [33] D.-S. Lin and R.-P. Chen, Phys. Rev. B 60, R8461 (1999); Surf. Sci. 454, 196 (2000).
- [34] Scientific Background on the Nobel Prize in Chemistry 2007, Chemical Processes on Solid Surfaces:
http://nobelprize.org/nobel_prizes/chemistry/laureates/2007/chemadv07.pdf
- [35] H. C. Flaum, D. J. D. Sullivan, and A. C. Kummel, J. Phys. Chem. 98, 1719 (1994).
- [36] H. Brune, J. Winterlin, J. Trost, G. Ertl, J. Wiechers, and R. J. Behm, J. Chem. Phys., 99 2128 (1993).
- [37] Y. L. Li, D. P. Pullman, J. J. Yang, A. A. Tsekouras, D. B. Gosalvez, K. B. Laughlin, Z. Zhang, M. T. Schulberg, D. J. Gladstone, M. McGonigal, and S. T. Ceyer, Phys. Rev. Lett. 74, 2603 (1995).
- [38] J. A. Jensen, C. Yan, and A. C. Kummel, Phys. Rev. Lett. 76, 1388 (1996).
- [39] R. S. Nord and J. W. Evans, J. Chem. Phys. 82, 2795 (1985).
- [40] J. J. Boland, Science 262, 1703 (1993).
- [41] D. Rioux, F. Stepniak, R. J. Pechman, and J. H. Weaver, Phys. Rev. B 51, 10981 (1995).
- [42] C. F. Herrmann and J. J. Boland, Surf. Sci. 460, 223 (2000).
- [43] C. F. Herrmann and J.J. Boland, J. Phys. Chem. B 103, 4207 (1999).
- [44] M. Gothelid, G. L. Lay, and U. O. Karlsson, Surf. Sci. 556, 203 (2004).
- [45] D. Chen and J. J. Boland, Phys. Rev. Lett. 92, 096103 (2004).

-
- [46] G. J. Xu, A. W. Signor, A. Agrawal, K. S. Nakayama, B. R. Trenhaile, and J. H. Weaver, *Surf. Sci.* 577, 77 (2005).
- [47] Gabor A. Somorjai, *Introduction to Surface Chemistry and Catalysis* (John Wiley & Sons, New York, 1994).
- [48] G. R. Darling and S. Holloway, *Rep. Prog. Phys.* 58, 1595 (1995).
- [49] H. Doshita, K. Ohtani, and A. Namiki, *J. Vac. Sci. Technol. A* 16, 265 (1998).
- [50] Y. Liu, D. P. Masson, and A. C. Kummel, *Science* 276, 1681 (1997).
- [51] E. J. Buehler and J. J. Boland, *Surf. Sci.* 425 L363 (1999).
- [52] T. C. Shen, C. Wang, G. C. Abeln, J. R. Tucker, J. W. Lyding, P. Avouris, and R. E. Walkup, *Science* 268, 1590 (1995).
- [53] X. Tong and R. A. Wolkow, *Surf. Sci.* 600, L199 (2006).
- [54] M. McEllistrem, M. Allgeier, and J. J. Boland, *Science* 279, 545 (1998).
- [55] M. Dürr, A. Biedermann, Z. Hu, U. Höfer, and T. F. Heinz, *Science* 296, 1838 (2002).
- [56] A. Bruce et al 2005 *Quantum Dots: Fundamentals, Applications, and Frontiers* (NATO Science Series vol 190) (Dordrecht: Springer), and reference therein
- [57] P. Michler, 2004 *Single Quantum Dots: Fundamentals, Applications and New Concepts* (Berlin: Springer), and reference therein.
- [58] E. S. Kim, N. Usami, and Y. Shiraki, *Semicond. Sci. Technol.* 14, 257 (1999).
- [59] T. Kitajima, B. Liu, and S. R. Leone, *Appl. Phys. Lett.* 80, 497 (2002).
- [60] B. Yang, F. Liu, and M. G. Lagally, *Phys. Rev. Lett.* 92, 25502 (2004).
- [61] H. M. Lee, T. H. Yang, G. Luo, and E. Y. Chang, *Japan. J. Appl. Phys.* 43, L247 (2004).
- [62] G. Jin, J. L. Lium, S. G. Thomas, Y. H. Luo, K. L. Wang, and B. Y. Nguyen, *Appl. Phys. A* 70, 551 (2000).
- [63] Y. Suda, S. Kaechi, D. Kitayama, and T. Yoshizawa, *Thin Solid Films* 464/465, 190 (2004).
- [64] A. Olzierski, A. G. Nassiopoulou, I. Raptis, and T. Stoica, *Nanotechnology* 15, 1695 (2004).
- [65] Y. Y. Zhang, J. Zhang, G. Luo, X. Zhou, G. Y. Xie, T. Zhu, and Z. F. Liu, *Nanotechnology* 16, 422 (2005).
- [66] I. Zübel, and I. Barycka, *Sensors Actuators A* 70, 250 (1998).
- [67] L. Vescan, K. Grimm, M. Goryll, and B. Hollander, *Mater. Sci. Eng. B* 69/70,

324 (200) and references therein.

- [68] H. J. Kim, Z. M. Zhao, J. Liu, V. Ozolins, J. Y. Chang, and Y. H. Xie, *J. Appl. Phys.* 95, 6065 (2004).
- [69] A. Hartmann, L. Vescan, C. Dieker, and H. Lüth, *J. Appl. Phys.* 77, 1959 (1994).
- [70] F. Ratto et al, *Appl. Phys. Lett.* 84, 4526 (2004).
- [71] P. D. Szkutnik, A. Sgarlata, N. Motta, and A. Balzarotti, *Mater. Sci. Eng. C* 23, 1053 (2003).
- [72] F. Ratto, A. Locatelli, S. Fontana, S. Ashtaputre, S. K. Kulkarni, S. Heun, and F. Rosei, *Phys. Rev. Lett.* 96, 96103 (2006).
- [73] N. Motta, F. Rosei, A. Sgarlata, G. Capellini, S. Mobilio, and F. Boscherini, *Mater. Sci. Eng. B* 88, 264 (2002).
- [74] Y. W. Mo, J. Kleiner, M. B. Webb, and M. G. Lagally, *Phys. Rev. Lett.* 66, 1998 (1991).
- [75] T. I. Kamins, and R. S. Williams, *Appl. Phys. Lett.* 71, 1201 (1997).
- [76] K. N. Tu, J. W. Mayer, and L. C. Feldman, 1992 *Electronic Thin Film Science for Electrical Engineers and Materials Scientists* (New York: Macmillan)

